

A statistical analysis of landfast sea ice breakout events at  
the northern floe edge of Admiralty Inlet, Nunavut

by

Calder Patterson

A thesis submitted to the Faculty of Graduate and Postdoctoral  
Affairs in partial fulfillment of the requirements for the degree of

Master of Science

in

Geography

Carleton University  
Ottawa, Ontario

© 2021, Calder Patterson

## **Abstract**

In the spring, Inuit travel across landfast ice to the northern floe edge in Admiralty Inlet to hunt. During this time, the floe edge can be unstable, and floes can break free (I.e., breakout) from landfast ice, stranding hunters on mobile ice floes. To assess this risk, a climatology of breakout events from 2000-2020 was developed, which revealed that first events in the spring now occur 46 days earlier and 6-7 more of these events now occur each year than two decades ago. Point-biserial correlations between past breakout events and meteorological variables from ECMWF's reanalysis dataset (ERA5) were calculated to explore potential associations. These yielded weak ( $|r| = 0.06-0.12$ ) yet significant relationships to winds, rainfall, and snowfall. A logistic regression model to predict breakout timing outperformed climatology but had low skill. *In situ* observations of breakout events and environmental conditions near the floe edge are recommended to improve prediction.

## **Acknowledgements**

This thesis would not have been possible without the thorough and considerate guidance of my supervisors, Dr. Adrienne Tivy and Dr. Derek Mueller. Their experience as researchers and contributions as editors were invaluable.

This project was funded by the Crown-Indigenous Relations and Northern Affairs Canada. Further support was provided by SmartICE and the Canadian Ice Service. Additional financial support was provided by the Ontario Graduate Scholarship and scholarships from Carleton University.

Field work in Admiralty Inlet prior to the commencement of my master's degree was an incredible experience, made all the better by the company of Ada Loewen and Dr. Greg Crocker. We were guided on the landfast sea ice of Admiralty Inlet by Ikpiarjuk locals Nigel Kigutikajuk, Gideon Allurut, and the late Levi Kalluk. We also received incredible insight from the Arctic Bay Guardians (Nauttiqsuqtiit).

I would like to thank Dr. Greg Crocker, Dr. Joshua Turner, Dr. Trevor Bell, and Ada Loewen, who provided feedback and insights that helped refine my research.

I am also extremely grateful to my parents, Dr. Tim Patterson, and Dr. Elizabeth Anderson for their advice, support and most importantly for feeding me when I didn't have time or energy to feed myself.

# Table of Contents

<b>Abstract.....</b>	<b>ii</b>
<b>Acknowledgements .....</b>	<b>iii</b>
<b>Table of Contents .....</b>	<b>iv</b>
<b>List of Tables .....</b>	<b>vi</b>
<b>List of Figures.....</b>	<b>vii</b>
<b>Chapter 1: Introduction .....</b>	<b>1</b>
1.1    Research context.....	2
1.2    Research questions .....	6
1.3    Approach .....	7
1.4    Thesis structure.....	7
<b>Chapter 2: Literature review .....</b>	<b>9</b>
2.1    Landfast sea ice in the Canadian Arctic Archipelago.....	9
2.1.1    Formation and deterioration of landfast sea ice .....	9
2.1.2    Remote sensing of landfast sea ice.....	13
2.1.2.1    Optical remote sensing .....	13
2.1.2.2    Synthetic aperture radar.....	14
2.1.3    Modelling landfast sea ice breakup.....	17
2.1.4    Landfast sea ice in Admiralty Inlet .....	19
2.2    Logistic regression.....	21
2.2.1    Logistic regression model fit.....	24
2.2.2    Logistic regression assumptions and expectations.....	27
2.3    Measures of forecast skill.....	30
2.3.1    Generating a binary forecast .....	32

<b>Chapter 3: Data and Methods .....</b>	<b>35</b>
3.1 Data .....	35
3.2 Methods .....	40
3.2.1 Landfast sea ice phenology during breakup in Admiralty Inlet .....	42
3.2.2 Data pre-processing for relational statistics .....	46
3.2.3 Significance of environmental variables .....	49
3.2.4 Logistic regression .....	52
<b>Chapter 4: Results.....</b>	<b>59</b>
4.1 Landfast sea ice phenology.....	59
4.2 Significance of environmental variables .....	67
4.3 Logistic regression.....	69
<b>Chapter 5: Discussion .....</b>	<b>81</b>
5.1 Landfast sea ice phenology in Admiralty Inlet.....	81
5.2 Significant environmental variables .....	85
5.3 Logistic regression.....	89
5.4 Approaches to ice breakout modelling and future directions .....	93
<b>Chapter 6: Conclusion.....</b>	<b>99</b>
<b>References .....</b>	<b>103</b>
<b>Appendices.....</b>	<b>114</b>
Appendix A - ERA5 reanalysis variables.....	114
Appendix B - Breakout events.....	117
Appendix C - Significant environmental variables .....	120
Appendix D - Auxiliary logistic regression models .....	124

## List of Tables

Table 2.1 Other commonly used satellites equipped with SAR imaging instruments.....	16
Table 2.2 Yes/No forecast contingency table for n binary events. ....	31
Table 3.1 Summary of the datasets used in this thesis.....	36
Table 4.1 Reduced predictor pool of 37 environmental variables. ....	68
Table 4.2 Logistic regression parameters for the seven predictors in the benchmark long-leads logistic regression model. ....	71
Table 4.3 Logistic regression parameters for the four predictors in the benchmark short-leads logistic regression model. ....	72
Table 4.4 Modelled and expected observation frequencies from the long-leads benchmark model within each decile of probability for breakout events.....	75
Table 4.5 Modelled and expected observation frequencies from the short-leads benchmark model within each decile of probability for breakout events. ....	76
Table 4.6 Summary of performance measures for the climatology probability density function and logistic regression results.....	78
Table 4.7 Measures of performance and fit for auxiliary models developed from unused predictors.....	79
Table 4.8 Yes/No forecast contingency table for the ensemble model.....	80
Table 5.1 Probability partition scheme for the benchmark logistic regression model.....	98

## List of Figures

Figure 1.1 Location of Admiralty Inlet and nearby places of interest in the surrounding region. ....	2
Figure 2.1 Generalized thermal gradient within sea ice and overlying snow cover at the onset of melt in the spring.....	11
Figure 2.2 Admiralty Inlet and surrounding geographic features of note.....	20
Figure 2.3 Diagram visualizing the receiver operating characteristic. ....	34
Figure 3.1 ERA5 0.25° grid cells that completely overlie Admiralty Inlet that were used in this study, and the location that WebTide data was computed for. ....	39
Figure 3.2 Methods flowchart.....	41
Figure 3.3 Breakout event in Admiralty Inlet, captured by RADARSAT-2 images in July of 2013. ....	43
Figure 3.4. Division of the spring season into three sub-seasons. ....	47
Figure 4.1 MODIS imagery of the 2013 spring season landfast ice deterioration in Admiralty Inlet.....	60
Figure 4.2 Number of breakout events identified in satellite imagery each year. ....	62
Figure 4.3 Timing of breakout events identified in satellite imagery.....	63
Figure 4.4 Histogram of breakout events observed on each day of all spring seasons on record. ....	64
Figure 4.5 Size of breakout events, categorized by location along the northern floe edge in Admiralty Inlet.....	65

Figure 4.6 The day-of the year on which breakout events occurred, grouped by location along the northern floe edge in Admiralty Inlet.....	66
Figure 4.7 Plot of the linear relationships between the value of each predictor and the logit of the model outcome. ....	70
Figure 5.1 Tide elevation (m) and breakout events (black vertical lines) observed in satellite imagery from June through July for 2000 to 2003.....	83

## Chapter 1: Introduction

Average air temperatures are increasing at a greater rate in the Arctic than at lower latitudes and climate models project this rapid regional warming will continue (Dai et al., 2019; Ye & Messori, 2021). This Arctic Amplification phenomenon has been attributed to (among other causes) an ice-albedo feedback mechanism where warming leads to a reduction in sea ice cover and decreasing albedo, which drives further reduction in sea ice cover by allowing greater uptake of heat in the ocean through absorption of solar radiation (IPCC, 2019; Serreze & Barry, 2011). For over four decades, Arctic sea ice cover has decreased significantly (Comiso et al., 2017; Perovich et al., 2020). In addition to a reduction in sea ice extent, reductions in ice thickness have also been observed (Howell et al., 2016; Perovich et al., 2020). This is also true in the narrow, shallow channels of the Canadian Arctic Archipelago, where landfast sea ice (immobile sea ice that is attached to land) thickness has decreased, and the length of the ice-free season in the summer has increased (Galley et al., 2012; Howell et al., 2016).

Traditional Inuit ways of life and local commercial enterprises have been significantly impacted by this reduction in sea ice extent and duration since it increases the risk associated with ice-based activities (Cooley et al., 2020; Enfotec Technical Services, 2003; Ford et al., 2019; Galley et al., 2012; Nickels et al., 2005). For example, the community of Ikpiarjuk (Arctic Bay; Figure 1.1) in Nunavut relies on landfast sea ice in Admiralty Inlet for travel north to the floe edge where the landfast ice meets the open ocean. The spring hunting and tourism season is the most active time for travel there when pods of narwhal migrate along the floe edge as the ice breaks up. Inuit hunt whales

along the opening leads, yet it is during this period when the risk of sea ice breakup is greatest (Cooley et al., 2020; Ford et al., 2006; Nickels et al., 2005). Over the last few decades in Ikpiarjuk there have been incidents where people have become stranded on sea ice floes that have broken free of landfast ice, some requiring search-and-rescue intervention, and incurring significant loss of equipment and property (Enfotec Technical Services, 2003; Ford et al., 2006; Learns, 2016). These landfast sea ice breakout events and the period in which they occur are the focus of this thesis.

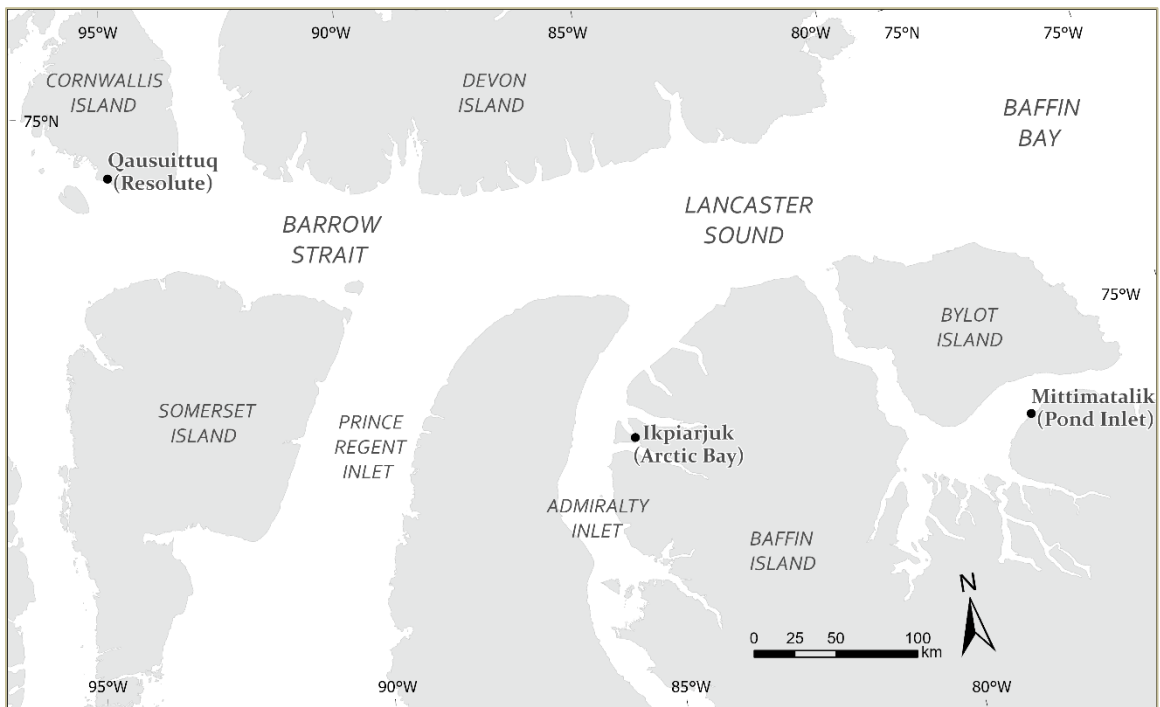


**Figure 1.1** Location of Admiralty Inlet and nearby places of interest in the surrounding region.

## 1.1 Research context

Approximately 540,000 km<sup>2</sup> of the narrow channels and straits in the Canadian Arctic Archipelago are covered by landfast ice each winter, representing approximately one

third of the landfast ice in the entire Arctic (Perovich et al., 2018). Its vast coverage and cultural significance make it an important priority for cryosphere and global climate research and for the communities that rely on its seasonal presence (Cooley et al., 2020; Nickels et al., 2005). In contrast to mobile pack ice, landfast sea ice is an immobile, continuous sheet of ice that is contiguous with the shore and attached to it by grounded ice (Barry et al., 1979; Mahoney et al., 2007, 2014). Depending on the salinity of the water, formation of landfast sea ice in ice-free water begins when average air temperatures are between 0°C and -1.8°C, when it begins to grow seaward from shore (Barry et al., 1979; Mahoney et al., 2014). The seaward edge of landfast ice can be stabilized by pack ice that has accumulated along its edge by winds or currents (Barry et al., 1979; Mahoney et al., 2007, 2014; Petrich et al., 2012).

Deterioration of landfast sea ice occurs because of thermal (ice melting) and/or mechanical (forced by winds, currents, and tides) processes (Petrich et al., 2012). In many parts of the Arctic, landfast sea ice breakup (mobilization of deteriorating landfast sea ice) has been occurring progressively earlier in the spring season (Dai et al., 2019; Galley et al., 2012; Mahoney et al., 2014; Selyuzhenok et al., 2015; Serreze & Barry, 2011). The reasons for this earlier break-up are varied. When surface air temperatures are above the melting point of the ice, it will begin to decay in place. This ice may remain fastened to the shore until it melts completely (thermal breakup), or storms or surge events may unground or fracture the decaying landfast ice (mechanical breakup) resulting in an ice floe that may simply drift away (Jones et al., 2016; Mahoney et al., 2007, 2014; Petrich et al., 2012). Wadhams (2000) described discrete events that occur during breakup, which are characterized by the opening of a flaw lead, or crack, between the free

ice floe and the landfast ice. Sea ice floes varying in size from a hundred square metres to hundreds of square kilometres can breakout from landfast sea ice and drift out into the open ocean. These discrete events are defined as landfast sea ice “breakout events”. Several breakout events can occur in quick succession if the floe edge is unstable, but the floe edge may also remain stable for a long period of time between breakout events (Wadhams, 2000).

In Ikpiarjuk, access to many hunting areas is dependent on the conditions of the landfast sea ice in Admiralty Inlet. The ability to anticipate and respond to dangers, like breakout events, is essential for safe travel (Enfotec Technical Services, 2003; Ford et al., 2006; Nickels et al., 2005). Inuit Qaujimagatuqangit (IQ) describes the congress of Inuit knowledge, culture, values, worldview, language, social organization, life skill, perceptions, and expectations, which Inuit have always used to adapt to their environment, including variable sea ice conditions (Wilson et al., 2021). As a result of rapidly changing climate conditions, many ice users report that their IQ used to make predictions have become less dependable (Wilson et al., 2021). As a result, hunting is more hazardous, and the need for operational landfast sea ice forecasts is more urgent (Ford et al., 2006).

Studies of landfast sea ice have provided insights into how landfast sea ice deteriorates in the late spring and early summer (Crocker & Wadhams, 1989; Else et al., 2014; Petrich et al., 2012), however only one study has resulted in the development of an operational forecast model. Petrich et al. (2012) developed a model to forecast the onset of thermal breakup in northern Alaska up to two weeks in advance. While the model isolates thermal decay mechanisms, it does not address the dynamic forces that contribute to mechanical

landfast ice breakup (Petrich et al., 2012). Conversely, Crocker & Wadhams (1989) modelled landfast sea ice breakup in McMurdo Sound, Antarctica, to investigate the mechanical breakup processes. Their primary findings are that wind-induced tensile failure and incident sea swells are the only significant mechanism for fracture (Crocker & Wadhams, 1989). Loewen (2020) modelled large “plug” type breakout events in Admiralty Inlet using finite element modelling and found that pre-conditioning is required to reduce the ice strength enough to allow relatively low wind and current forces to initiate a breakout event. The Loewen (2020) study has helped to enhance our understanding of breakout events in Admiralty Inlet but does not provide an ability to forecast risk and is focused on a smaller subset of breakout events.

The research conducted for this thesis is a component of the *Landfast Sea Ice Breakup Prediction in a Changing Climate* project funded by Crown-Indigenous Relations and Northern Affairs Canada (CIRNAC) through the Climate Change Preparedness in the North Program. The project partners with Carleton University are the Canadian Ice Service and *SmartICE*. The Canadian Ice Service provides information about the condition of ice and icebergs in Canada’s navigable waters to ensure the safety of Canadians, their property, and their environment. *SmartICE* ([smartice.org](http://smartice.org)) is a northern social enterprise that provides communities with technology that helps them adapt to unpredictable sea ice conditions resulting from climate change. *SmartICE* has been invited by the Tuvaliriji (*SmartICE*’s Community Management Committee in Arctic Bay) to operate in Ikpiarjuk and have been asked for assistance developing knowledge and tools that can be implemented to enhance the safety of sea ice. This thesis supports *SmartICE* and Tuvaliriji’s objectives and seeks to increase our understanding of the

patterns, timing, and mechanisms of landfast sea ice breakup in Admiralty Inlet through the analysis of archived remote sensing and environmental data. The findings of this thesis, along with the results from the overarching research project will be presented to the community of Ikpiarjuk in workshops facilitated by *SmartICE* staff.

## **1.2 Research questions**

This thesis examines past breakout events, assesses historical changes, and attempts to develop predictive ability. The goal of this thesis is to increase our understanding of the timing and mechanisms of landfast sea ice breakout at the northern floe edge of Admiralty Inlet through the analysis of archived remote sensing and environmental data. These analyses are used to develop and test statistical models that predict landfast sea ice breakout events in Admiralty Inlet. The following research questions were addressed to meet the goal of this thesis:

1. How have landfast sea ice breakout events at the northern floe edge of Admiralty Inlet changed over the last two decades?
2. Which readily available environmental variables have a significant relationship to landfast sea ice breakout events at the northern floe edge of Admiralty Inlet?
3. Can a logistic regression model skillfully predict the risk of sea ice breakout events at the northern floe edge of Admiralty Inlet?

### **1.3 Approach**

To address the research questions outlined above, historical satellite images were analyzed to determine the timing of landfast sea ice breakout events in Admiralty Inlet and identify changes over the last two decades. Environmental data were correlated against the historical observations of breakout events to determine which ones had significant relationships with breakout events. The significant predictors were used to develop a logistic regression model, which was tested using several validation schemes and performance measures.

These analyses will provide an understanding of how ice conditions are changing as the Arctic climate warms and improve our knowledge of the processes involved in breakout events by revealing which underlying environmental variables are best correlated with them. The model produced here has the potential to be implemented operationally as part of an automated ice safety awareness toolkit to provide users with daily predictions (i.e., probabilities of breakout events occurring). Although this thesis focuses on the landfast ice in Admiralty Inlet near Ikpiarjuk, it is anticipated that the knowledge pertaining to sea ice breakup and methods developed to predict breakout events are applicable to and could be implemented in many locations across Inuit Nunangat (Inuit homelands in Canada).

### **1.4 Thesis structure**

This document follows a standard thesis format. Chapter 1 has introduced the topic, provided context, and enumerated the research objectives. Chapter 2 contains a review of

the literature relevant to landfast sea ice deterioration, logistic regression and measures of model performance and skill. The methods used to collect historical observations, identify significant predictors of breakout, and develop logistic regression models are presented in Chapter 3, and the results of this work are presented in Chapter 4. The implications of these results for our understanding of landfast sea ice in Admiralty Inlet and potential for implementation of the developed model are discussed in Chapter 5 and the final conclusions are summarized in Chapter 6. A complete list of references is provided at the end of the document, and ancillary tables and figures are included in the appendices.

## **Chapter 2: Literature review**

### **2.1 Landfast sea ice in the Canadian Arctic Archipelago**

Sea ice is known as ‘landfast’ where it is either attached to the shore, or to shoals, or to thick, non-drifting glacial ice, such as ice shelves, marine-terminating glaciers, and grounded icebergs (Galley et al., 2012). Landfast sea ice is typically seasonal, forming in the fall and winter, and melting in the spring and summer (Galley et al., 2012). In the Canadian Arctic Archipelago (CAA), landfast ice forms in confined channels and fjords and in straits between islands. This ice is of particular importance in Inuit communities, where the landfast ice has social, cultural, and economic significance by providing a platform for travel, hunting, and fishing (Ford et al., 2006; Galley et al., 2012). In the CAA, the seasonal duration of landfast ice, between the onset of freeze up and breakup, is decreasing significantly. Between 1983 and 2009, onset occurred 0.64 to 1.07 weeks later per decade, and breakup occurred 0.57 to 0.89 weeks earlier per decade (Galley et al., 2012). This decrease in ice duration is a component of the ice albedo feedback effect, where the increase of open water causes increased absorption of solar energy, which contributes to the changing climate in the CAA (Galley et al., 2012; IPCC, 2019).

#### **2.1.1 Formation and deterioration of landfast sea ice**

Landfast sea ice typically begins to form along the shore in early winter as the shallow water column cools rapidly. The sea ice grows outward from the shore and freezes to the bottom, down to depths of approximately 2 m as it thickens (Wadhams, 2000). The

maximum thickness of the ice is largely controlled by snow cover, which can insulate the ice from the cold air, slowing down the freezing process (Howell et al., 2016). Landfast ice development is most extensive in areas where the near-shore slope is gentle because shallow water cools more rapidly (Barry et al., 1979; Wadhams, 2000). Ice which is adhered to the shore is called the ice foot and is unaffected by tides, due to the formation of a tidal crack. Ice that forms seaward of the tidal crack can rise and fall independently of the ice foot (Wadhams, 2000).

At the seaward margin of the landfast ice, onshore pressure from mobile pack ice can create highly ridged or deformed ice, which can be indicative of the boundary between landfast and mobile sea ice. If the mobile ice floes adhere to the landfast ice, it may become immobile, effectively increasing the extent of the landfast ice (Wadhams, 2000). If the mobile pack ice moves away from the landfast ice (i.e., they diverge) a lead of open water is created. The boundary between the fast ice and mobile ice pack is called a flaw lead, which can undergo refreezing mid-winter, when the speed of the mobile pack ice slows, forming an area of thin landfast ice (Wadhams, 2000).

The decay of landfast sea ice occurs relatively quickly in comparison to its formation, driven by atmospheric and oceanographic processes. There are two main modes that cause breakup, thermal and mechanical, which can occur independently or concomitantly (Galley et al., 2012; Petrich et al., 2012). Thermal breakup is primarily driven by increased atmospheric temperatures and downwelling radiation and can also be enhanced by addition of heat from river runoff (Galley et al., 2012). Before the snow cover melts, the ice is insulated from changes in atmospheric temperatures. There is also a thermal

gradient that cools upwards from approximately freezing temperatures at the ice-ocean interface towards the snow-ice interface (Figure 2.1).

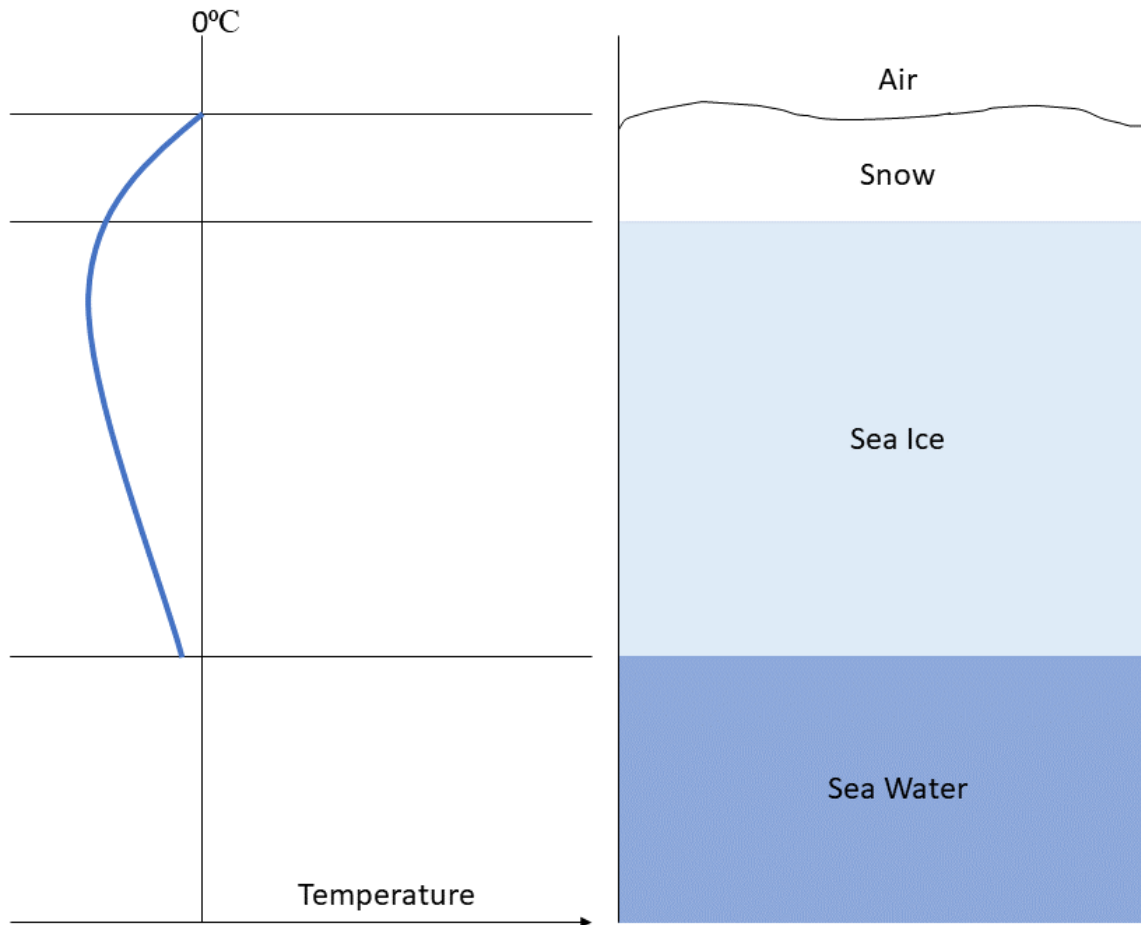


**Figure 2.1 Generalized thermal gradient within sea ice and overlying snow cover at the onset of melt in the spring. The snow and ice cover cool inwards as melt at the interfaces with the air (0°C) and sea water (-1.8°C) progresses (Untersteiner, 1986).**

After the snow melts, the ice warms and becomes isothermal, allowing significant melting to occur. As thermal breakup progresses, the stages of deterioration are characterized by changes in albedo (Perovich & Polashenski, 2012). Albedo is highest when the snow cover remains cold, prior to any significant melt. During snow melt,

ponds begin to form in pits in the snow cover, decreasing albedo. Next, a small increase of albedo accompanies pond drainage, when the pits connect with the sea water below the ice. As the pits continue to expand, they re-flood and albedo continues to decrease as the melt ponds evolve. Eventually, the ice breaks up entirely, leaving open water, which has the lowest albedo (Perovich & Polashenski, 2012). Throughout this progression, the reduction in albedo increases the absorption of solar energy, further enhancing melt (Perovich & Polashenski, 2012).

Landfast sea ice deterioration is enhanced by dynamic forces from winds, currents, and waves (Jones et al., 2016). These forces act to physically break ice, forming leads and creating mobile floes that can be advected away (Wadhams, 2000). Sea ice has a low tensile strength, the ice's ability to resist fracture, which decreases considerably as ice temperature increases, so strong winds and currents that impinge upon the large surface area of landfast ice may have a significant impact on the formation of leads (Itkin et al., 2017; Shokr & Sinha, 2015; Wadhams, 2000). Storm-generated waves at the seaward edge of the landfast ice may be energetic enough to break the ice (Kohout et al., 2014). The extent of pack ice plays an important role in impeding breakup by attenuating waves that otherwise may fracture the ice (Crocker & Wadhams, 1989; Kohout et al., 2014).

Deterioration of landfast ice is often characterized by the formation of leads between immobile ice and a mobile floe (Wadhams, 2000). The process of mobile floes drifting into open water, away from landfast ice, is defined as a "breakout event" in this thesis; community members in Ikpiarjuk refer to this process as "breakoff".

## **2.1.2 Remote sensing of landfast sea ice**

Most of Earth's sea ice is found in remote areas at high latitudes, so the most practical way of monitoring sea ice extent and seasonal variability is by using satellite imagery (Pedersen et al., 2017; Shokr & Sinha, 2015; Wadhams, 2000). Optical imagery is readily available at various spatial and temporal resolutions; however, these images are limited by polar darkness and cloud cover. Cloud cover is very prevalent at the ice edge, which is obscured by clouds much of the time. A solution is to use passive and/or active microwave sensors, which can penetrate cloud cover, and do not rely on sunlight (Pedersen et al., 2017; Wadhams, 2000).

### **2.1.2.1 Optical remote sensing**

Optical remote sensing measures the reflection of solar radiation in the visible and near infrared (NIR) bands. Measurements from optical sensors are from reflectance at the top of the atmosphere, surface reflectance is obtained by accounting for atmospheric effects like absorption, scattering, and emission of radiation. The albedo of seawater typically falls between 0.04 and 0.08, depending on the incidence angle of the incoming solar radiation. This is much lower than the albedo from sea ice or snow, which falls between 0.4 and 0.8, making sea ice appear brighter than sea water (NSIDC, 2021a).

There are several optical imaging satellites that can be used to observe sea ice, one of the more widely used is the Moderate Resolution Imaging Spectroradiometer (MODIS), an instrument aboard the Terra and Aqua satellites, launched by NASA in 1999 and 2002,

respectively. These two satellites view the entirety of the Earth in 1 to 2 days and acquire 36 spectral bands, ranging from 0.4  $\mu\text{m}$  to 14.4  $\mu\text{m}$ , and have a resolution of 250 m, 500 m, and 1000 m (NASA, n.d.). Bands 4, 6, 7, 13, 16, 20, 26, 31, and 32 are used in the MODIS snow and sea ice mapping algorithm (Hall et al., 2001). The two satellites work in tandem to maximize cloud-free surface viewing, and because the satellites have polar orbits, they view high latitude regions multiple times per day (NSIDC, 2021a).

### **2.1.2.2 Synthetic aperture radar**

Synthetic aperture radar (SAR) is an active remote sensing technology used for Earth observation. Its use is privileged in sea ice studies as a tool to monitor, measure and map sea ice and is often used as the primary source of information for sea ice charting (Pedersen et al., 2017; Shokr & Sinha, 2015). SAR satellites send out a fan-shaped microwave beam and converts the backscattered energy into a geometrically corrected image of the Earth's surface (GC-CSA, 2021). Backscattered energy is often converted to a greyscale image for viewing, with black representing no return from the surface and white corresponding to the maximal amount of backscatter in the image (Pedersen et al., 2017). Sea ice generally appears bright relative to sea water in SAR images because it has a strong backscatter response due to its greater resistance to penetration at microwave frequencies. Rough ice and ice with a higher concentration of gas bubbles and voids looks especially bright because of strong surface (and shallow sub-surface) scattering from the raised ridges that reflect microwaves back towards the sensor (Onstott & Shuchman, 2004; Pedersen et al., 2017; Wadhams, 2000). In contrast, water is an order of

magnitude less resistant to microwave penetration than ice, so it appears dark grey to black, unless there was significant surface roughness produced by wind-driven waves, which may make it appear brighter (Pedersen et al., 2017). SAR satellites operating within the C-band of frequencies (4-8 GHz) can differentiate between ice cover types better than other radar frequencies, like X-band (8-12GHz), which are more sensitive to surface conditions, and L-band (1-2 GHz), which have a deeper penetration (Onstott & Shuchman, 2004).

Canada's first SAR satellite RADARSAT-1 was launched in 1995. RADARSAT-1 included a wide swath option, providing images 450 km wide at 100 m resolution (GC-CSA, 2021). RADARSAT-2 (owned by MacDonald, Dettwiler and Associates' (MDA)) was launched in 2007 and had enhanced capabilities relative to RADARSAT-1 (GC-CSA, 2021). RADARSAT-2 resolutions ranged from 1 to 100 metres and scene widths that range from 144 to 250,000 km<sup>2</sup> (GC-CSA, 2021). In June of 2019, the RADARSAT Constellation Mission (RCM) was launched (GC-CSA, 2019). RCM provides imaging of the Arctic up to four times each day (GC-CSA, 2019). RCM historical imagery was not available for this research, so only RADARSAT-1 and -2 imagery was used in this thesis. All the RADARSAT missions operate within the C-band of frequencies. There are several other SAR instruments aboard various satellites, however, these satellites have not produced large sets of historical imagery like the RADARSAT series, and so they were not considered in this research. Some other satellites equipped with SAR instruments are listed in Table 2.1.

**Table 2.1** Other commonly used satellites equipped with SAR imaging instruments. Abbreviations: European Space Agency (ESA); German Aerospace Centre (DLR).

Satellite	Instrument	Years of operation	Band	Agency
Sentinel-1 (a and b) <a href="https://sentinel.esa.int/web/sentinel/missions/sentinel-1">https://sentinel.esa.int/web/sentinel/missions/sentinel-1</a>	C-SAR	2014 – pres.	C	ESA
TerraSAR-X <a href="https://eoportal.org/web/eoportal/satellite-missions/t/terrasar-x#sensors">https://eoportal.org/web/eoportal/satellite-missions/t/terrasar-x#sensors</a>	TSX-SAR	2007 – pres.	X	DLR
ENVISAT <a href="https://earth.esa.int/eogateway/missions/envisat">https://earth.esa.int/eogateway/missions/envisat</a>	ASAR	2002 – 2012	C	ESA
ERS 1 and 2 <a href="https://earth.esa.int/eogateway/missions/ers">https://earth.esa.int/eogateway/missions/ers</a>	SAR	1991 – 2000; 1995 – 2011	C	ESA

Passive microwave remote sensing makes use of the natural microwaves emitted by the Earth’s surface. Clouds emit relatively little microwave radiation compared to sea ice, so this method can also be used to detect sea ice during polar darkness and cloud cover (NSIDC, 2020). The main drawback of this method is the limited energy emitted by the surface, requiring coarser resolutions, making features like leads difficult to observe (NSIDC, 2020). Passive microwave sensors constitute the longest data set of sea ice observations, going back as far as 1972, captured by the Electrically Scanning Microwave Radiometer (ESMR), aboard the Nimbus-5 satellite (NSIDC, 2020). Other instruments include the 1978 Scanning Multichannel Microwave Radiometer (SMMR), the 1987 Special Sensor Microwave/Imager (SSM/I), the 2002 Advanced Microwave

Scanning Radiometer-Earth Observing System (AMSR-E), and AMSR-2 in 2012 (NSIDC, 2020).

### **2.1.3 Modelling landfast sea ice breakup**

Landfast ice is represented in coupled modelling systems (Lemieux et al., 2016) but not with the physics or resolution to simulate the deterioration of a floe edge. Breakup of coastal landfast sea ice in northern Alaska has been modelled by Petrich et al. (2012). Their main findings are that the sea ice remains landfast until expanding melt ponds weaken the ice enough that very little force from winds and currents can disintegrate the ice, and the best predictor for the progression of thermal decay of the near-shore sea ice cover is downwelling solar radiation (Petrich et al., 2012). The model had good model accuracy, able to predict when breakup would occur within two days (Petrich et al., 2012). Unfortunately, the findings of Petrich et al. (2012) are not directly transferable to the study of landfast breakout events in Admiralty Inlet because the landfast ice is coastal, not confined in an inlet. Additionally, it does not consider mechanical breakup, which has been reported as a significant contributor to breakout events by community members (Bell et al., 2019; Ford et al., 2006).

Between 1999 and 2003, a heuristic modelling approach in Admiralty Inlet (as well as Eclipse Sound, Navy Board Inlet and initially Cumberland Sound) was undertaken as a pilot project by Enfotec Technical Services. They developed a prototype system for monitoring the stability of landfast sea ice near the Nunavut communities of Ikpiarjuk (Arctic Bay), Mittimatalik (Pond Inlet), and Pangniqtuuq (Pangnirtung), to deliver an

advisory/warning service to northern communities, and to help reduce the frequency of people becoming stranded on floating ice (Enfotec Technical Services, 2003). In addition to investigating breakup patterns through community consultation and analysis of historical satellite data, fieldwork was conducted that included collecting ice thickness data and deploying satellite drift beacons on the landfast ice. Prototype products delivered to the community were periodic maps that indicated the current ice edge, locations of recent ice loss, areas of high and moderate potential for ice fracture, water, moving ice, and landfast ice, based primarily on satellite image interpretation. In 2001 in Admiralty Inlet, the products delivered to the community at Ikpiarjuk incorrectly predicted the location of initial ice breakout and the timing was correctly predicted (Enfotec Technical Services, 2003). Although the products were well received, the project did not progress beyond the pilot phase.

Loewen (2020) is the first work that computationally models the breakout of landfast sea ice in Admiralty Inlet. The work focuses on “plug” failures, which are large breakout events that span the entire width of the inlet. Numerical experiments using finite element modelling demonstrated the effects of environmental stresses, ice material properties, and leads on sea ice deformation prior to breakup. Environmental stresses acting on the ice were weak, and so, like the findings of Petrich et al. (2012), they proposed that preconditioning by way of deterioration of ice strength and development of cross-inlet and shore leads allowed relatively low wind and current forces to initiate a breakout event (Loewen, 2020).

#### **2.1.4 Landfast sea ice in Admiralty Inlet**

Admiralty Inlet (Figure 2.2) is located at the northern end of Baffin Island, Nunavut. The inlet runs north to south and is intersected by several adjoining inlets along the eastern shore. It is approximately 300 km long, and 60 km wide where the inlet meets Lancaster Sound, and at its centre the inlet is up to 800 metres deep (Jakobsson et al., 2012).

Landfast ice is present in the inlet for up to 10 months of the year, freezing up in October and breaking up in July (Galley et al., 2012). However, the inlet experienced a later onset of landfast ice of 1.4 weeks per decade between 1983 and 2009 (Galley et al., 2012). The northern floe edge of the landfast ice is of great importance to the nearby community of Ikpiarjuk (Arctic Bay) because it is where community members hunt seal and narwhal (Ford et al., 2006).

In the early 2000s, breakup in the inlet began as early as the third week of June to the second week of July. Fracturing in the inlet was completed by the end of July, and open water conditions were reached by early August (Enfotec Technical Services, 2003). This breakup timing was still prevalent in the early 2010s (Galley et al., 2012). Breakup hazards are greatest for hunters travelling on the ice, particularly near Cape Charles Yorke, where early ice chipping (i.e., gradual deterioration of the floe edge) at the opening to Lancaster Sound was greatest (Enfotec Technical Services, 2003; Ford et al., 2006). Sudden fracturing southward into Elwin Inlet can cut off travel to and from Cape Crauford, an important location for tourism.

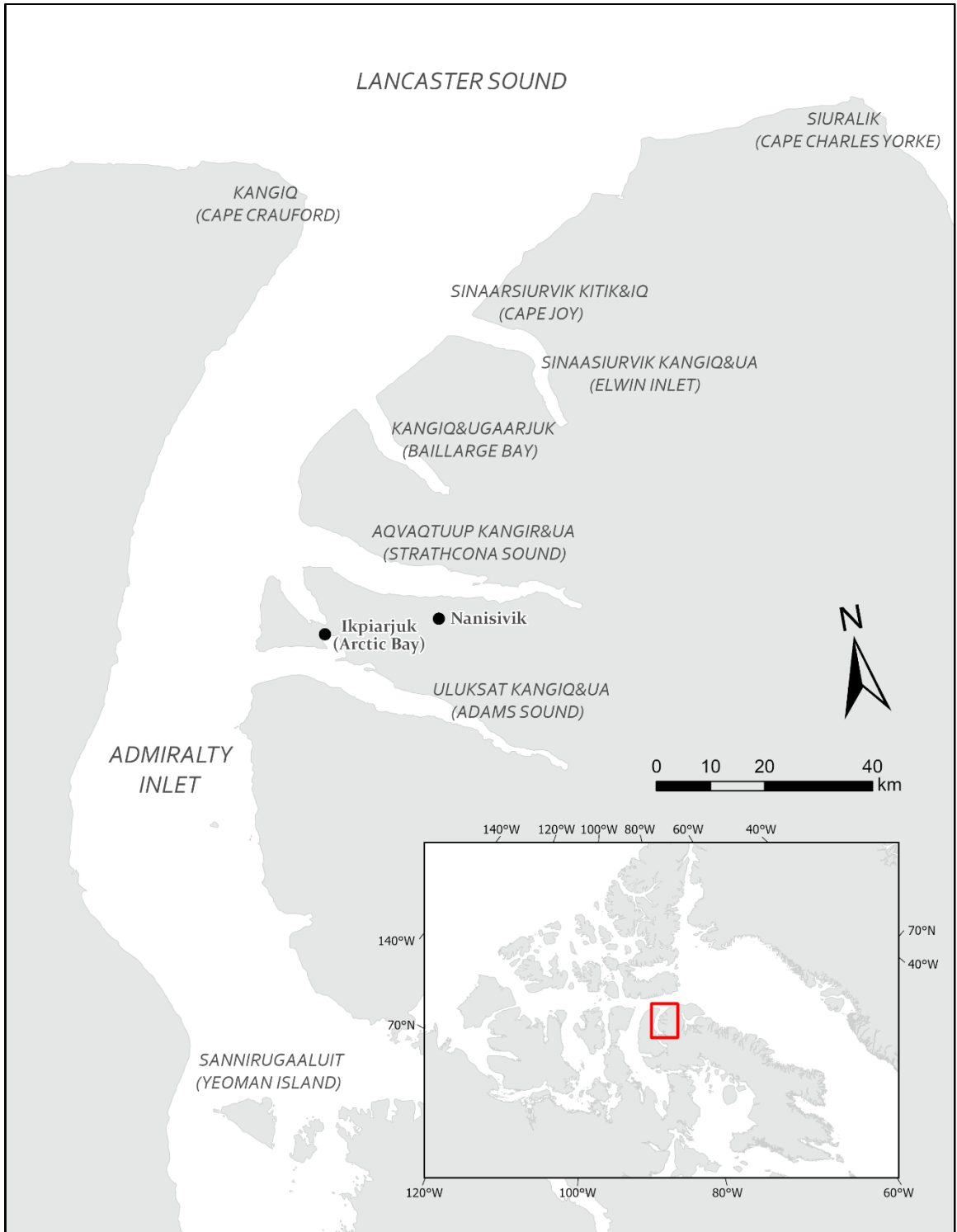


**Figure 2.2 Admiralty Inlet and surrounding geographic features of note. The key map (bottom right) indicates the location of Admiralty Inlet at the north end of Baffin Island (red rectangle).**

The pattern of fracture of fast ice in Admiralty Inlet is controlled by stress fractures that form east-west across the inlet, and breakup progresses from north to south in stages, controlled by these stress fractures (Enfotec Technical Services, 2003). The landfast ice in the adjoining inlets melt out entirely several weeks earlier due to a combination of warm freshwater runoff and shore melting from solar radiation (Enfotec Technical Services, 2003). Eastward currents entering Admiralty Inlet from Lancaster Sound flow south along the western edge of the inlet and cross west to east before turning northward and flowing northeast past Cape Joy into Lancaster Sound (Enfotec Technical Services, 2003). These currents cause floes from the fractured landfast ice to drift into eastern Lancaster Sound (Enfotec Technical Services, 2003). The Enfotec study found that high-risk periods coincided with the highest tides (spring tides) that occur twice in each lunar cycle (Enfotec Technical Services, 2003); and community members have attributed breakout events to sudden and unexpected changes in wind conditions (Ford et al., 2006). There are two dominant wind directions in Arctic Bay, north and south, and the strongest winds are from the south (Ford et al., 2006; Loewen, 2020). Southerly winds are associated with more turbulent conditions and northerly winds are associated with clear weather (Ford et al., 2006).

## **2.2 Logistic regression**

There are many empirical modelling techniques that could be used to forecast breakout events. For example, artificial neural networks (ANN) and vine copulas (Yu et al., 2019; Zhao et al., 2012) have been used to model river ice breakup. Other methods that could be employed to predict breakout include classification and regression trees (CART) and

Bayesian regression models. Each of these modelling methods has its merits and could be implemented in a forecast for breakout events. However, logistic regression is a more appropriate modelling method for two reasons. First, logistic regression is specifically used for binary or ordinal outcomes (Hosmer et al., 2013). Additionally, it is mathematically simple, based on a cumulative distribution function that can be interpreted similarly to linear regression, and ease of interpretation is important in exploratory studies (Hosmer et al., 2013). This modelling technique is reviewed below.

Logistic regression is a powerful modelling tool which uses a set of independent variables to predict a categorical response variable (Hosmer et al., 2013; Ottenbacher et al., 2004; Stoltzfus, 2011). In binary logistic regression, the response variable is binary, coded as 1 or 0 (e.g., events vs. non-event, left vs. right, etc.). The prediction from a logistic regression model ranges from 0 and 1 and represents the probability of the response being 1 (Hosmer et al., 2013).

In typical linear regression problems, the response variable is assumed to be continuous and exhibits a linear relationship with the independent predictor that may range from  $-\infty$  to  $+\infty$ . These assumptions are invalid for a binary response variable, which is coded as 0 and 1. To address this issue, a cumulative distribution function called the logistic distribution (Equation 2.1) is used, which represents the conditional probability that the response variable is equal to 1 given  $x$ , the independent variable (Hosmer et al., 2013).

$$\pi(x) = \frac{e^{\beta_0 + \beta_1 x}}{1 + e^{\beta_0 + \beta_1 x}} \quad \text{Equation 2.1}$$

To allow similar interpretation of the intercept,  $\beta_0$ , and coefficient,  $\beta_1$ , in linear regression models, the logistic distribution is transformed using the logit transformation, (also known as the log-odds transformation). The logit (Equation 2.2) is assumed to be linear with the independent variables in the model, is continuous and its range is not bounded between 0 and 1 (Hosmer et al., 2013).

$$\mathbf{g}(x) = \ln \left[ \frac{\pi(x)}{1-\pi(x)} \right] = \beta_0 + \beta_1 x \quad \text{Equation 2.2}$$

For a multiple logistic regression model, which has  $p$  parameters denoted by the vector  $x' = (x_1, x_2, \dots, x_p)$ :

$$\mathbf{g}(x') = \ln \left[ \frac{\pi(x')}{1-\pi(x')} \right] = \beta_0 + \beta_1 x_1 + \beta_2 x_2 + \dots + \beta_p x_p \quad \text{Equation 2.3}$$

The intercept ( $\beta_0$ ) and coefficients ( $\beta_p$ ) are estimated using statistical software, which uses a function called the likelihood function (Equation 2.4) that expresses the probability of the observed data as a function of the predictors (Hosmer et al., 2013). For a pair  $(x_i, y_i)$ , if  $y_i = 1$ , then the contribution to the likelihood function is  $\pi(x_i)$ . If  $y_i = 0$ , then the contribution to the likelihood function is  $1 - \pi(x_i)$ .

$$l(\beta) = \prod_{i=1}^n \pi(x_i)^{y_i} [1 - \pi(x_i)]^{1-y_i} \quad \text{Equation 2.4}$$

A set of maximum likelihood estimators for each of the predictors maximize the likelihood function to best match the observed data (Hosmer et al., 2013; Stoltzfus, 2011). This is accomplished by an iterative weighted least squares procedure that identifies the optimal linear combination of predictors with the greatest likelihood of predicting the observed response variable (Hosmer et al., 2013; Stoltzfus, 2011). This is

easier to do using the log of the likelihood function, referred to as the log-likelihood (Equation 2.5).

$$L(\boldsymbol{\beta}) = \ln[l(\boldsymbol{\beta})] = \sum_{i=1}^n \{y_i \ln[\pi(x_i)] + (1 - y_i) \ln[1 - \pi(x_i)]\} \quad \text{Equation 2.5}$$

The confidence intervals (CIs) for the coefficients of each predictor are calculated as  $\beta_1 \pm z_{1-\frac{\alpha}{2}} \widehat{SE}(\beta_1)$ , and as  $\beta_0 \pm z_{1-\frac{\alpha}{2}} \widehat{SE}(\beta_0)$  for the intercept, where  $z_{1-\frac{\alpha}{2}} = 1.96$  for the 95% CI. In addition to estimating the coefficients of the model parameters, modelling software also calculates the standard errors ( $\widehat{SE}$ ), p-values and z-scores. The p-value represents the probability that the null hypothesis is correct, which is that any contributions of a parameter in the model is due to random chance and therefore is not significant. The z-scores, or Wald statistics, are the coefficients divided by the standard error. As z-scores increase, uncertainty surrounding the estimation of the coefficients decreases because the standard errors are getting much smaller relative to the coefficients. The z-score is susceptible to Type II error, which occurs when the null hypothesis is accepted incorrectly.

### 2.2.1 Logistic regression model fit

To assess the fit of each predictor in the constructed model, the observed events are compared to the predicted probabilities. In logistic regression, this is based on the log-likelihood function, which is used to calculate the deviance ( $D$ ; Equation 2.6). If the

probabilities of the observed events are high, and low for the non-events, then the model has a low deviance, and therefore a good fit for the data.

$$D = -2 \cdot L(\beta) \quad \text{Equation 2.6}$$

To assess the significance of a predictor, we compare the value of  $D$  with and without the predictor to obtain the statistic  $G$  (Equation 2.7), from the likelihood ratio test (Hosmer et al., 2013). To do this, a second “null” model is also constructed, which does not contain the predictor in question (Hosmer et al., 2013).  $G$  follows the  $\chi^2$  distribution; if the predictor contributes to the model significantly, then the p-value of  $\chi^2$  will be small.

$$G = -2 \ln \left[ \frac{(\text{likelihood without the predictor})}{(\text{likelihood with the predictor})} \right] \quad \text{Equation 2.7}$$

Predictor selection can be accomplished iteratively using automated or manual processes in a backward or forward stepwise fashion. Once the model contains only predictors that are not collinear and that significantly contribute to the model, it is considered parsimonious and can be assessed for its goodness of fit. Many summary statistics of the goodness of fit are readily computed using statistical software. Pseudo- $R^2$  statistics compare the log-likelihood of the fitted model ( $\ln(L_C)$ ) to the log-likelihood of a null model ( $\ln(L_{null})$ ), which just has an intercept and no covariates (Hosmer et al., 2013). Likelihoods fall between 0 and 1, so the log of a likelihood is less than or equal to zero. If a model has a very low likelihood, then the log-likelihood will have a much larger magnitude than the log of a more likely model. If the log likelihoods are similar (i.e., the fitted model is not significantly different from the null model), then the statistic will be

close to 0, which means the model has very little predictive power. If the log-likelihoods are very different, then the statistic will be close to 1. A commonly used pseudo-R<sup>2</sup> statistic is McFadden’s pseudo-R<sup>2</sup> (Equation 2.8), which ranges from 0 to 1. Generally, pseudo-R<sup>2</sup> statistics are difficult to interpret as indicators of model fit for a standalone model, however it is valuable for comparing models. The model with the greater likelihood would have the greater McFadden’s pseudo-R<sup>2</sup> (Hosmer et al., 2013).

$$pR_{McFadden}^2 = 1 - \frac{\ln(L_C)}{\ln(L_{null})} \quad \text{Equation 2.8}$$

An alternative statistic is generated using the Hosmer-Lemeshow test, which is used to examine the distribution of the model probabilities by grouping both observed events and predicted events into ten “deciles” (Hosmer et al., 2013; Stoltzfus, 2011). The division of each probability decile is assigned at probability thresholds such that there are an equal number of observed events in each decile. For each decile, the number of observed events is compared to the number of events predicted by the model. For example, the second decile might contain all observed events with modelled probabilities greater than the first decile and less than the third decile. If we observed three events in the 2<sup>nd</sup> decile, then we hope the model will predict a similar number in that decile. The number of events predicted in each decile is estimated by summing the one minus the estimated probabilities of each event in that decile (Hosmer et al., 2013). If the model is a poor fit of the data, then the observed events and predicted events in each decile will be very different (Hosmer et al., 2013). The Hosmer-Lemeshow goodness of fit statistic is calculated from the Pearson chi-squared statistic from the table of deciles, with the

alternative hypothesis that the distributions are drawn from different populations.

Therefore, if the p-value less than  $\alpha = 0.05$  then there is evidence of a poor model fit, otherwise, the null hypothesis is accepted, which is that the model is deemed a good fit and that the predicted events are representative of the observed events (Hosmer et al., 2013).

### **2.2.2 Logistic regression assumptions and expectations**

Several assumptions and expectations of logistic regression analysis need to be assessed to ensure that it is being implemented appropriately. The assumptions that need to be satisfied for the correct implementation of binary logistic regression modelling are the following:

- 1) The response variable must be binary or dichotomous (Hosmer et al., 2013; Ottenbacher et al., 2004; Stoltzfus, 2011).
- 2) There should be little to no multicollinearity in the predictors because highly correlated predictors will result in large standard errors. An explicit test of multicollinearity should be undertaken and reported (Ottenbacher et al., 2004; Stoltzfus, 2011).
- 3) The error of the predictors should be independent. In other words, there is no repetition of observations (Stoltzfus, 2011).
- 4) There should be no strongly influential data points. Any data points with standardized residuals greater than 3 standard deviations should be removed (Stoltzfus, 2011).

- 5) There must be a linear relationship between the continuous predictors and the logit of the response variable (Hosmer et al., 2013; Ottenbacher et al., 2004; Stoltzfus, 2011)). If the predictors do not meet this assumption, they can be transformed to a different scale or dummy coded and re-tested for linearity, but any predictors that do not meet this assumption should not be included in the model (Hosmer et al., 2013; Stoltzfus, 2011).

There are additional criteria described by Ottenbacher et al. (2004) for the correct examination of logistic regression models. These are considered to be best practices, not statistical requirements for correct implementation of logistic regression. Nevertheless, these criteria were adhered to as best as possible in this thesis:

- 1) There should be an explanation of how the predictors were selected. This may include the results of previous research or significant association in a bivariate analysis with the response variable (Ottenbacher et al., 2004; Stoltzfus, 2011).
- 2) Sufficient observed events in the response variable per independent predictor; too many predictors will overfit the observations, resulting in high standard error on the regression coefficients (Ottenbacher et al., 2004; Stoltzfus, 2011). Logistic regression models require more events than predictors to iteratively cycle through different solutions to find the best model fit for the data through the process of maximum likelihood iteration (Stoltzfus, 2011). A rule of thumb is a minimum of ten events for each independent predictor, but more observations tend to improve model validity (Ottenbacher et al., 2004; Stoltzfus, 2011).

- 3) Test for interactions between predictors; interaction terms can be derived for predictor pairs (Hosmer et al., 2013; Ottenbacher et al., 2004; Stoltzfus, 2011). Interaction terms can needlessly complicate the logistic regression model without providing much benefit, so their inclusion should be considered carefully and there should be some justification of why these terms were or were not included (Stoltzfus, 2011).
- 4) How the predictors are coded should be described. This applies to any transformations of the predictors (e.g., interaction terms, higher order transformations, normalization), and dummy coding of nominal predictors. Describing the coding is essential for interpreting the results (Ottenbacher et al., 2004).
- 5) The procedure for entering the predictors into the model should be stated. Possible procedures are forward inclusion, backward inclusion, and best subset (Ottenbacher et al., 2004).
- 6) Statistical tests of significance should be applied to each predictor, and the complete model (Hosmer et al., 2013; Ottenbacher et al., 2004).
- 7) Goodness of fit measures or discrimination statistics (e.g., ROC curves, Hosmer-Lemeshow statistics, etc., see section 2.2.1 and 2.3) should be reported, describing how well the entire model matches the observed values (Ottenbacher et al., 2004).
- 8) Models should be validated. A validation procedure using a subset of the original sample should be used to develop the model and coefficients, and the results should be tested against the remaining. This can include split-sampling, cross-

validation, bootstrapping or other resampling methods, etc. (Ottenbacher et al., 2004; Stoltzfus, 2011).

### **2.3 Measures of forecast skill**

Forecasts of meteorological events are almost never absolute and are expressed as a probability or likelihood of occurrence, with some expression of the uncertainty (Hogan & Mason, 2011). Classic examples include forecasts for precipitation. If an event is particularly extreme or hazardous (floods, tornadoes, frost, fog, heat, cold, etc.) and the probability of its occurrence is above a given threshold, then a warning could be issued (Hogan & Mason, 2011). The probabilities of these events can be converted to a binary decision of whether an event will occur or not. These yes/no forecasts have four possible predictive outcomes, which can be represented in a 2x2 contingency table, shown in Table 2.2. The cells of this matrix (i.e., hits (a), false alarms (b), misses (c) and correct rejections (d)) can be formulated to create measures of the performance of the forecast. The sum of these cells is the sample size (n).

**Table 2.2 Yes/No forecast contingency table for n binary events (after Hogan and Mason, 2012).**

Event forecast	Event observed		Total
	Yes	No	
Yes	a (Hits)	b (False alarms)	a + b
No	c (Misses)	d (Correct rejections)	c + d
Total	a + c	b + d	a + b + c + d = n

Verification measures are functions of the forecast, observations, or their relationship.

Verification measures are derived from the counts in Table 2.2 (i.e., a, b, c, d). The counts can be converted to relative frequencies by dividing by the sample size (n).

Performance measures are composed of subsets of distinct verification measures, that assess measures' individual or collective correspondences (Murphy, 1996). Some performance measures assess skill, which is the ability of the model to correctly forecast events and/or non-events, more often than would be expected by chance.

Hit Rate (H) is the proportion of forecasted events that were correctly forecast (Hogan & Mason, 2011). A perfect Hit Rate is 1, which indicates that all the observed events were correctly forecast. A Hit Rate of 0 indicates that there were no successful event forecasts.

$$H = a / (a + c) \qquad \text{Equation 2.9}$$

False Alarm Rate (F) is the proportion of non-events that were incorrectly forecast as events (Hogan & Mason, 2011). A perfect False Alarm Rate is 0, which indicates that no non-events were incorrectly forecast as events. A False Alarm Rate of 1 indicates that all non-events were incorrectly forecast as events.

$$F = b/(b + d) \quad \text{Equation 2.10}$$

The Peirce Skill Score (PSS) is the difference between the Hit Rate and the False Alarm Rate (Hogan & Mason, 2011). The Peirce Skill Score ranges from -1 to 1, with scores less than 0 indicating no model skill and greater skills being indicated by scores closer to 1.

$$PSS = H - F \quad \text{Equation 2.11}$$

The Symmetric Extremal Dependence Index (SEDI) is a non-degenerate skill metric used for both rare and overwhelmingly common events. Non-degenerate means that the score will not trend towards a meaningless base value if the observed rate of occurrence of an event is extremely small or large (Hogan & Mason, 2011).

$$SEDI = \frac{\ln F - \ln H + \ln(1-H) - \ln(1-F)}{\ln F + \ln H + \ln(1-H) + \ln(1-F)} \quad \text{Equation 2.12}$$

### 2.3.1 Generating a binary forecast

It is important to be able to convert continuous probabilities from a logistic regression model to a binary prediction regarding the response variable (Hogan & Mason, 2011). To convert a continuous probability to a binary outcome, an optimal decision threshold,  $w$ , needs to be identified; the decision threshold is a probability value above which an event is forecast and below which a non-event is forecast. This threshold maximizes the difference between Hit Rate (H, signal) and False Alarm Rate (F, noise). The decision threshold can be identified using the receiver operating characteristic (ROC), which is produced by iteratively calculating verification measures at small intervals of different

decision thresholds (Hogan & Mason, 2011). These measures at different intervals produce the ROC curve. The optimal decision threshold lies on the point of the curve that is closest to the upper left corner (i.e., a Hit Rate of 1), which can be located from the iterated set of decision thresholds where the Peirce Skill Score (PSS) is greatest (Hogan & Mason, 2011). This is illustrated in Figure 2.3, where the greatest difference between H and F is at a PSS ~0.4.

The closer the ROC curve is to a Hit Rate of 1, the greater the skill in detecting event signal. The closer the ROC curve is to a False Alarm Rate of 1, the worst the skill in detecting event signal (Hogan & Mason, 2011; Hosmer et al., 2013). Rules of thumb for the ROC curve are derived from the area under it. The plot can be treated as a unit square, so the area under the curve is calculated as a fraction from 0 to 1, which is the receiver operating characteristic (Hosmer et al., 2013; Stoltzfus, 2011). If the ROC is 0.5 or less, then the curve lies on or below the no skill line (Figure 2.3), which suggests no skill in distinguishing signal from noise (might as well flip a coin). If the ROC is 0.5 to 0.7, then the skill in distinguishing signal from noise is poor (not much better than a coin flip). An ROC greater than 0.7 is acceptable, greater than 0.8 is excellent, and greater than 0.9 is outstanding. An ROC of 0.7 is the minimum requirement for model performance (Hosmer et al., 2013; Stoltzfus, 2011).

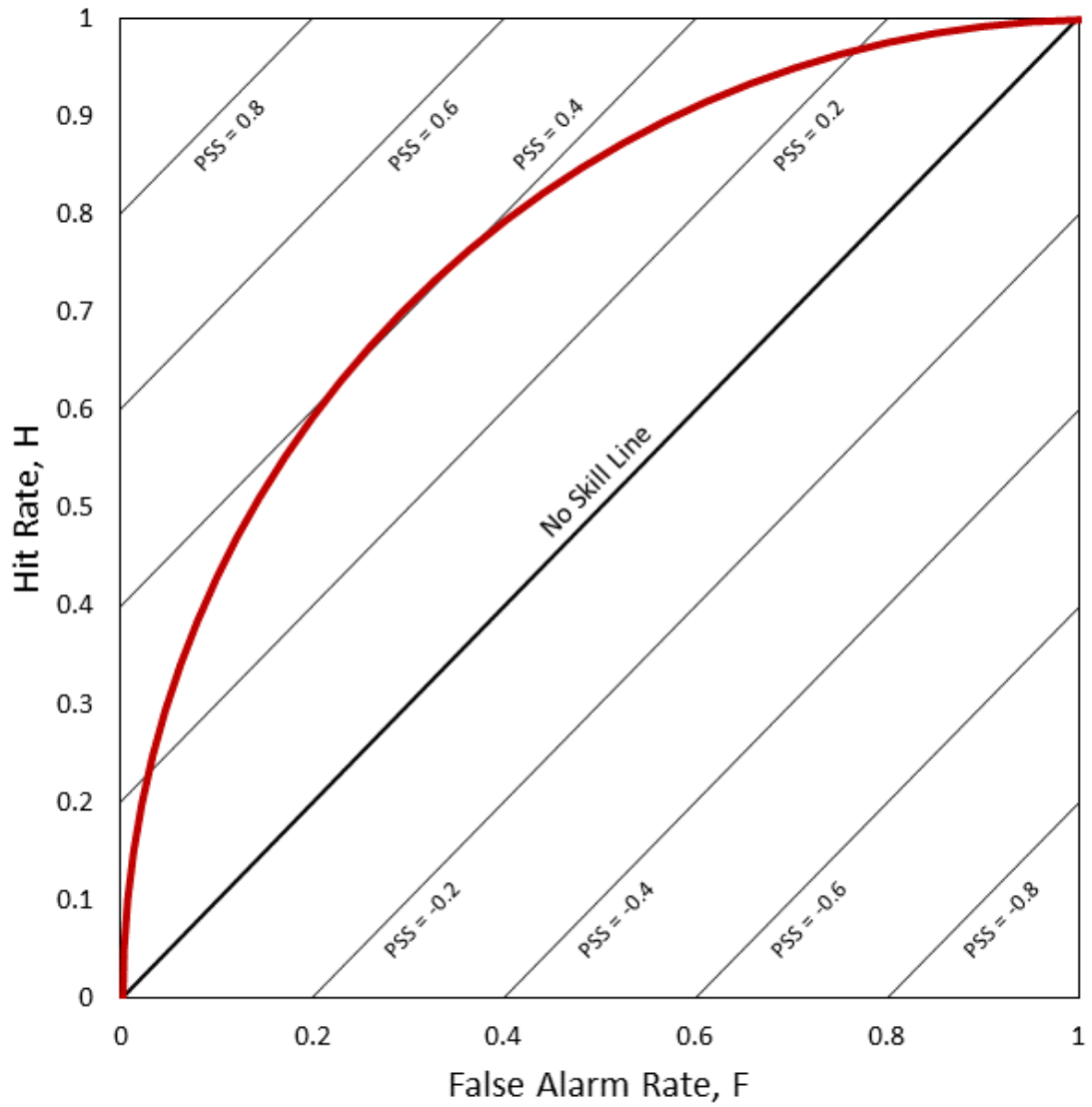


**Figure 2.3** Diagram visualizing the receiver operating characteristic. The contours represent the Peirce Skill Score (PSS), the red line shows the ROC curve. After Hogan and Mason (2012).

## **Chapter 3: Data and Methods**

To develop a greater understanding of changes in sea ice phenology in Admiralty Inlet over the last two decades, archived satellite imagery was acquired and studied (Objective 1). These images were used to develop a set of daily binary observations (0 or 1) of whether a breakout event occurred or not. This binary breakout event variable was compared to environmental data to determine which variables have a significant relationship with breakout events (Objective 2). Logistic regression was used to model the binary breakout event variable and to determine whether this modelling approach could skillfully forecast the risk of breakout events (Objective 3).

### **3.1 Data**

To meet the objectives of this thesis, several datasets were acquired (Table 3.1). A combination of synthetic aperture radar (SAR) and optical satellite imagery was used to study the sea ice breakup phenology over the last two decades and generate a binary breakout event variable. Environmental data were assessed to determine which variables had significant relationships with the binary breakout event variable, and those significant environmental variables were used as predictors in a logistic regression model to predict sea ice breakout events.

**Table 3.1 Summary of the datasets used in this thesis. Each data set includes data type, source, range and frequency of observations, and the project objective that it pertains to.**

	Data Type	Source	Data Range Acquired	Data Frequency
Satellite Imagery	RADARSAT-1		1997 to 2013	
		Canadian Ice Service – Environment and Climate Change Canada		Daily to Weekly
	RADARSAT-2		2008 to 2019	
	(MODIS) – Terra and Aqua	NASA Worldview ( <a href="https://worldview.earthdata.nasa.gov/">https://worldview.earthdata.nasa.gov/</a> )	2000 to 2020	Daily
Environmental Data	ERA5	European Centre for Medium-Range Weather Forecasts ( <a href="https://www.ecmwf.int/en/forecasts/datasets/reanalysis-datasets/era5">https://www.ecmwf.int/en/forecasts/datasets/reanalysis-datasets/era5</a> )	1979 to 2020	Hourly
	WebTide Tidal Prediction Model	Bedford Institute of Oceanography – Government of Canada ( <a href="https://www.bio.gc.ca/science/recherche-recherche/ocean/webtide/index-en.php">https://www.bio.gc.ca/science/recherche-recherche/ocean/webtide/index-en.php</a> )	2005 to 2019	Hourly

RADARSAT-1 and -2 ScanSAR mode (wide and narrow) images that intersect Admiralty Inlet between April 1<sup>st</sup> and July 31<sup>st</sup> each year from 1997 through 2019 were acquired from the Canadian Ice Service (CIS). The RADARSAT-1 and RADARSAT-2 images both have nominal resolutions of 100 metres (GC-CSA, 2021). The SAR images were clipped to a footprint that covered a larger area around the northern end of Baffin Island (Figure 1.1). The region of interest is large with respect to Admiralty Inlet to allow some observations of the sea ice conditions surrounding the inlet to be made. The images

were reprojected on the fly in ArcMap Desktop (version 10.6; Esri) to a Lambert Conformal Conic (LCC) projection, which is in use by the CIS for mapping in Canadian waters [central meridian: 100°W; latitude of the projection origin: 40°N; standard parallels at 49°N and 77°N] (CIS-ECCC, 2006).

Moderate Resolution Imaging Spectroradiometer (MODIS) Corrected Reflectance True Colour Terra and Aqua optical images, from April 1<sup>st</sup> to July 31<sup>st</sup> 2000 to 2020, were viewed and analyzed on the NASA Worldview website (<https://worldview.earthdata.nasa.gov>), part of the Earth Observing System Data and Information System. The images are daily mosaics and have a resolution of the 250 metres. The NASA Worldview has a well-developed interface for inspecting archived images, and they are displayed with a coastline in a Polar Stereographic projection and is commonly used for small scale mapping of satellite imagery and mosaics in polar research (NSIDC, 2021b).

Environmental data from the ERA5 reanalysis dataset was acquired from the European Centre for Medium-Range Weather Forecasting (ECMWF) using Copernicus Climate Change Service (C3S) information from the Climate Data Store (CDS) infrastructure. There are many other reanalysis datasets that could have been used, including ERA-I, JRA-55, CFSv2, MERRA-2, and ASRv2, but ERA5 was selected because it is easily accessible and widely used (Graham et al., 2019). The results contain modified C3S information 2021. Neither the European Commission nor ECMWF is responsible for any use that may be made of the Copernicus information or data it contains. The dataset is generated by running a global weather model in hindcast mode constrained to available observations. The ERA5 dataset (Appendix A ) provides hourly estimates of

meteorological variables on a 0.25-degree global grid from 1979 to the present (Hersbach et al., 2018). Additionally, a 10-day high resolution forecast product is available with the same environmental variables as the reanalysis products. The R package *ecmwf* (Koen, 2020) was used to access the Copernicus CDS, where the ERA5 reanalysis dataset is archived. All 105 numerical single-level variables (Appendix Table A.1) with continuous spatial coverage at 0.25° grid resolution were downloaded for all months from 2000 to 2020 at an hourly time step; grid cells containing only the ocean in Admiralty Inlet and along the floe edge area in Lancaster Sound were acquired (Figure 3.1).

Tidal data was acquired from the Bedford Institute of Oceanography's WebTide tidal prediction system for the Canadian Arctic Archipelago. The data set is produced using tidal constituents from available tide gauge stations that were interpolated using a finite element analysis, generating 17356 nodes across the region (Collins et al., 2011). The WebTide application (GC-BIO, 2015) was used to query this database and extract hourly tidal elevation and current (expressed as westward (*u*) and northward (*v*) components) model predictions from April through July for the years 2000 through 2019 at the north end of Admiralty Inlet (Figure 3.1), midway between Cape Crauford and Cape Joy (Collins et al., 2011). This location was selected to capture the tidal properties affecting the northern floe edge that might contribute to breakout events.

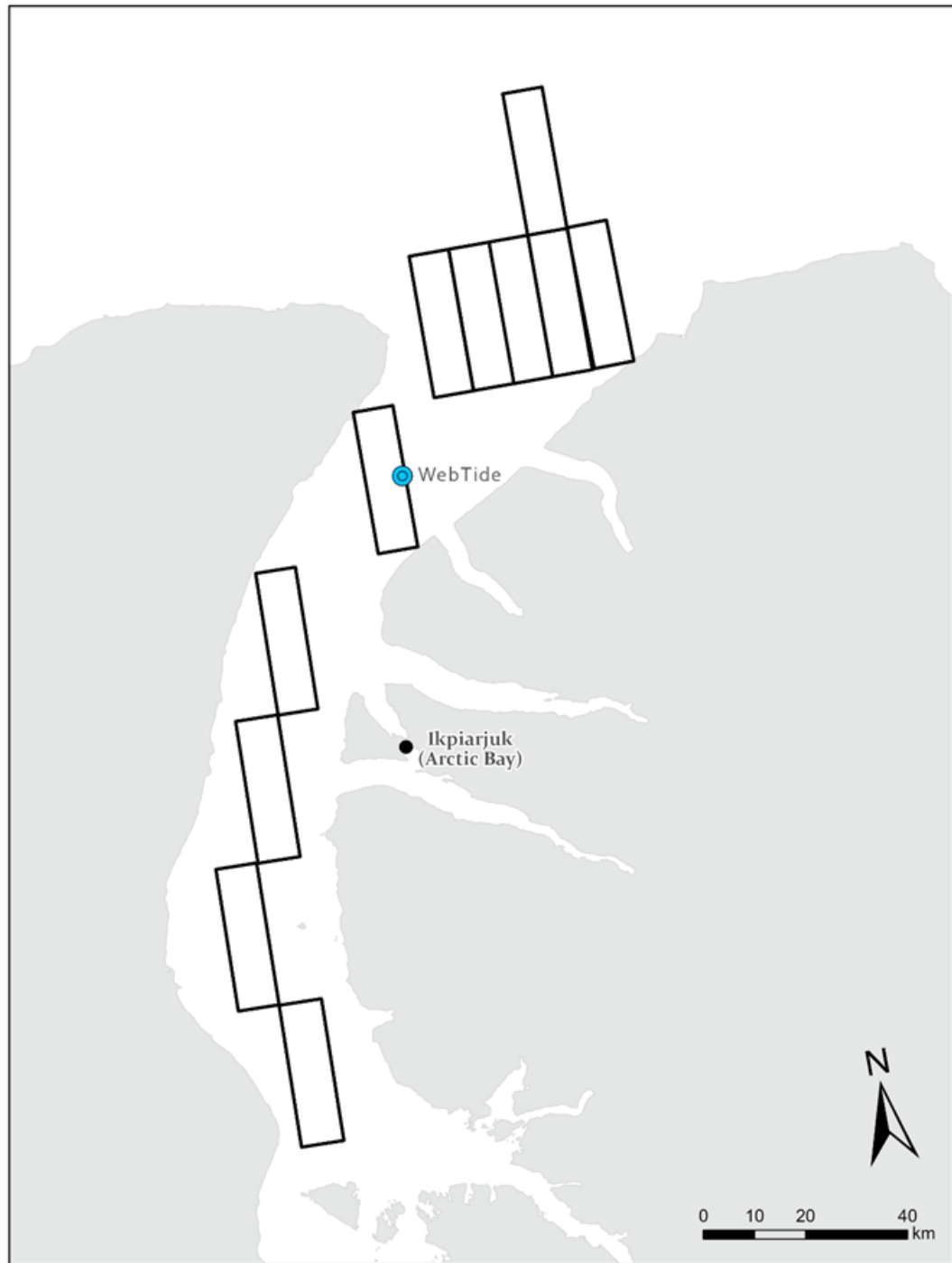


**Figure 3.1 ERA5 0.25° grid cells that completely overlie Admiralty Inlet that were used in this study. The location that WebTide data was computed for is indicated by the blue dot at 73.50°N, 84.89°W.**

## **3.2 Methods**

The phenology of breakup in Admiralty Inlet was described using satellite imagery (Figure 3.2, step 1); a dataset of daily observations of historical breakout events, where event days were coded as 1 and non-event days were coded as 0, was produced (section 3.2.1). These observations were compiled into a binary breakout event variable, which was compared to the environmental data to identify statistically significant relationships and to select environmental variables to include in a predictive model (Figure 3.2, step 2-3; section 3.2.3). The selected environmental variables were tested in a logistic regression model and the skill of the model was assessed to determine if it effectively forecasts the binary breakout event variable (Figure 3.2, step 4-6; section 3.2.4).

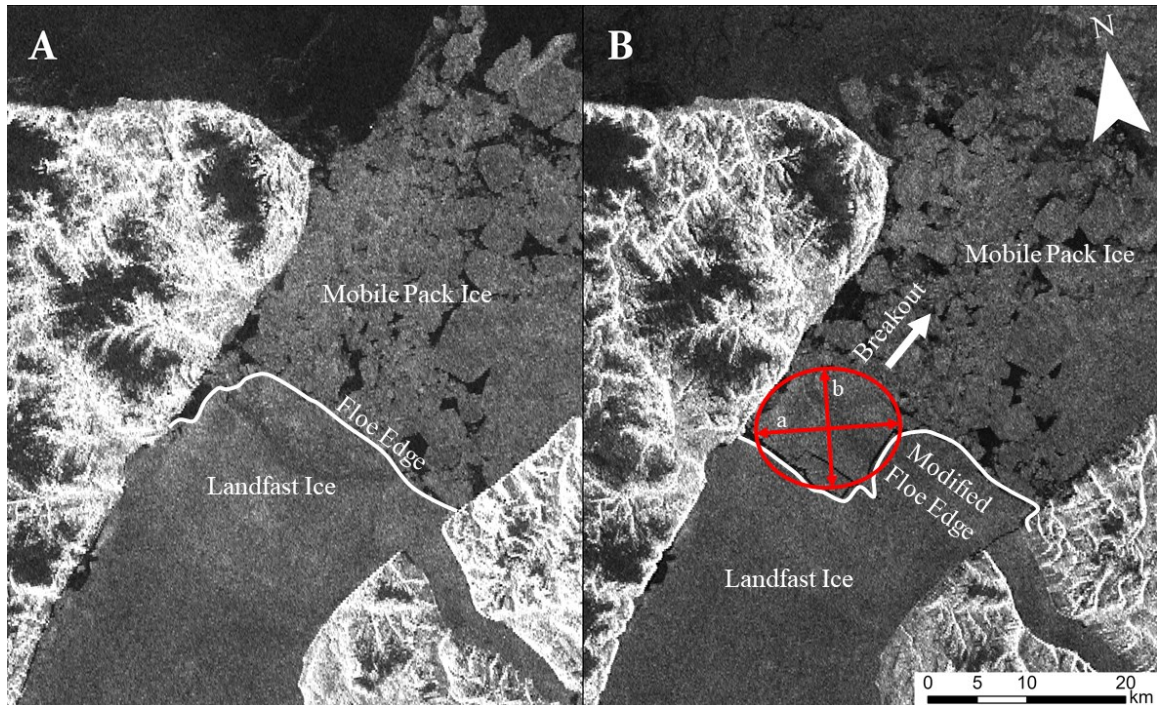


Figure 3.2 Methods flowchart. The workflow of processes (orange rectangles), from data sources (blue rectangles) to intermediate products (green ovals) and final products (red ovals), that were implemented to address the objectives of this thesis (Section 1.2). <sup>1</sup>An image analysis of SAR and optical satellite data produced a binary breakout event variable, which was used to develop a climatology model based on relative frequency of breakout. <sup>2</sup>Point biserial correlation identified significant relationships between environmental variables (from ERA5 and WebTide) and the binary breakout event variable. <sup>3</sup>A Pearson collinearity matrix was used to remove multicollinear environmental variables from candidate predictor variables. <sup>4</sup>Logistic regression models were constructed by selecting predictors from the candidate predictor pool. <sup>5</sup>Unused predictors were implemented in auxiliary models. <sup>6</sup>The primary logistic regression model and the auxiliary models were implemented in an ensemble model.

### **3.2.1 Landfast sea ice phenology during breakup in Admiralty Inlet**

To describe the sea ice phenology during spring breakup, SAR images from RADARSAT-1 and -2 and optical images from MODIS (Table 3.1) were used to build familiarity with the progression of sea ice breakup between April 1<sup>st</sup> and July 31<sup>st</sup> in each year on record. Visual inspection of the imagery was conducted to make qualitative observations regarding the state of the landfast sea ice in Admiralty Inlet and to describe patterns in sea ice deterioration. The images were also analyzed to determine the timing, size, and relative location of landfast sea ice breakout events. A sea ice breakout event was deemed to occur if a large floe of mobile sea ice broke free from the immobile landfast sea ice floe, and drifted into the open ocean (Wadhams, 2000).

The SAR images were opened in ArcMap and viewed at a scale of approximately 1:600,000. The area of interest was the north end of the inlet to observe changes to the landfast sea ice floe edge between Cape Crauford and Cape Charles Yorke, where the inlet meets Lancaster Sound. The image was panned and rescaled to inspect the floe edge more closely if a change was observed. The same was done for the MODIS imagery in the NASA Worldview interface. Breakout events were identified by comparing an image with the image that precedes it chronologically (Figure 3.3). If no breakout event was observed in either image, the lack of a breakout event was recorded (coded as 0) on these days and in the intervening days between the two images.



**Figure 3.3 Breakout event in Admiralty Inlet, captured by RADARSAT-2 images in July of 2013. Pre-breakout imagery on July 7, 2013 (A) and post-breakout imagery on July 8, 2013 (B). Breakout along the western floe edge joins the mobile ice floes that occupy the northern end of Admiralty Inlet, a breakout event was recorded for July 3, 2013. The size of the breakout event was approximated as an ellipse (red oval), measured with a long axis (a) and a short axis (b). RADARSAT-2 Data and Products © MDA Geospatial Services Inc. (2021) – All Rights Reserved. RADARSAT is an official mark of the Canadian Space Agency.**

If the landfast floe edge receded southward in the second image, when compared to the first, a breakout event occurred between the two images. Events were only recorded if the images were acquired within two days of each other, to constrain the breakout event to a reasonable number of days. These breakout events were recorded (coded as 1) on the date of the second image. Coding the breakout event on the date of the second image was chosen to ensure that the impact of environmental conditions on the actual date of the

event would not be missed if the timing of the event was attributed to an earlier date than the actual date of the event. Sometimes changes in the floe edge were observed but could not be constrained to a specific date (e.g., if there was a greater than 1-day gap in the imagery) due to gaps in the available archived SAR images that coincide with cloud cover in MODIS imagery. In these cases, no observations were recorded, so the date's observation was left blank (i.e., coded as NA), and therefore did not contribute to subsequent analyses. This was not a significant issue because it only occurred on three occasions, and only for 2- to 3-day periods.

Ancillary observations of the breakout events were made to record the size of the breakout events and the location of the event along the floe edge. Two measurements were taken: the long axis diameter of the region that broke off ( $a$ , the longest length across the floe), and the short axis diameter of the broken-out area ( $b$ , the diameter perpendicular to the long axis diameter). Assuming these areas are roughly elliptical in shape, area ( $A$ ) was calculated as  $A = \pi \left(\frac{a}{2}\right) \left(\frac{b}{2}\right)$  (Figure 3.3).

The location of each breakout event was categorized as being in the east, west or centre of the northern floe edge in Admiralty Inlet. Floes that broke away which were in contact with the eastern shore or were mostly located in the eastern half of the northern floe edge were classified as eastern breakout events. The same classification was used on the western end of the floe edge. Floes that originated equally from the west and east of the floe edge but were not in contact with either shore were classified as centre breakout events. If the breakout event extended from the eastern to western shore, then the breakout event was called a “plug failure”, consistent with the work of Loewen (2020).

Trends in the annual number of breakout events and the timing of breakout events from 2000 to 2020 were calculated using linear regression. The rate of change in the number of breakout events observed each year was assessed to determine if these events are becoming more frequent. To assess changes in the timing of the first breakout events and the onset of breakup, linear trend lines were also fit to the relationships between the day of the year of the first breakout events each year, and the onset of breakup each year. One year, 2012, was omitted from all the analyses except the onset of breakup because no breakout events were observed in 2012 ahead of the complete mobilization of the land fast ice in Admiralty Inlet. Significance values and confidence intervals were calculated for each linear trend. Box plots of the size and timing of breakout events grouped by relative location along the floe edge were generated. A Bartlett test determined that the variances of these categories were not homogeneous, so the non-parametric Kruskal-Wallis test was used to assess if there were significant differences in breakout surface area between location categories (Kabacoff, 2011).

A climatology model was generated as a benchmark to compare with the logistic regression results (see Section 3.2.4). The total number of breakout events for each day of the year across the study period was calculated and divided by the number of years on record [21]. A histogram (Figure 4.4) of this data provides the relative frequency of breakout events on each calendar day throughout the spring season. This dataset was smoothed with a 7-day rolling mean to remove noise and the resultant curve was taken to represent the empirical probability of a breakout event occurring on a given day of the year. An ROC curve (see Section 2.3.1) was used to identify the optimal decision threshold in the relative frequency of breakout events to convert the smoothed probability

curve to a binary outcome. Performance measures were derived from these outcomes so the climatology model could be compared to logistic regression.

### **3.2.2 Data pre-processing for relational statistics**

Data pre-processing was required before the environmental data and the binary breakout event variable could be used in correlation analysis to identify significant relationships (see Section 3.2.3), or in logistic regression modelling (see Section 3.2.4).

#### ***Defining the breakout season***

The binary breakout event variable was truncated to only include observations from the first breakout event to the onset of breakup each year. Early in the April 1<sup>st</sup> to July 31<sup>st</sup> spring season as defined for this thesis, no breakout events occur, while late in this season, breakout events occur daily or the landfast ice has become completely mobile as the inlet transitions to open water conditions. Since the focus of objective 2 and 3 of this thesis is the analysis of environmental variables and modelling of landfast sea ice breakout events, the period from April 1<sup>st</sup> to July 31<sup>st</sup> was subdivided into three distinct sub-seasons (Figure 3.4):

- 1) Pre-breakout season: begins on April 1<sup>st</sup> and precedes the first breakout event at the northern floe edge.

- 2) Breakout season: begins with the first breakout event at the northern floe edge and ends when breakout events occur daily or the ice in the inlet is completely mobile.
- 3) Breakup season: begins when breakout events occur daily, or when landfast ice in Admiralty Inlet is completely mobile and ends on July 31st.

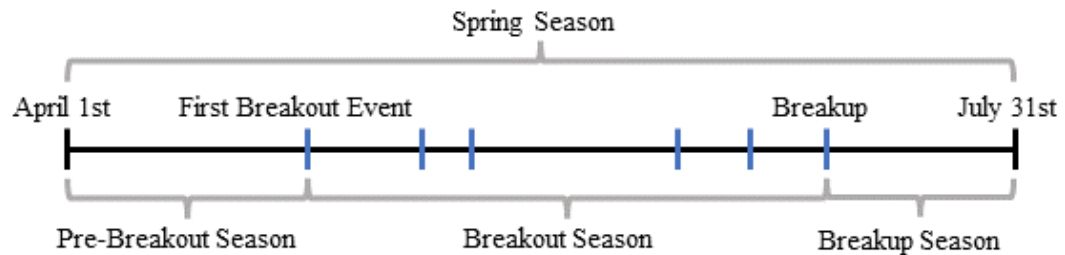


**Figure 3.4. Division of the spring season into three sub-seasons. Breakout events are indicated by vertical blue bars, the first breakout event and breakup are labelled. Note that in the breakup season there is continuous change in the structure of the landfast ice cover on a daily timescale.**

The breakout season is the focus of relational statistics and modelling in this thesis, not when conditions are unsuitable for breakout (i.e., the pre-breakout season) or when the ice strength is so poor that it is obviously unsuitable for travel (i.e., the breakup season). Including data from both the pre-breakout season and breakup season may bias the correlation of certain environmental variables with breakout events. For example, from April 1<sup>st</sup> to July 31<sup>st</sup>, variables such as accumulated degree days of melt would correlate well with breakout events simply because of a seasonal progression from many weeks of no breakout events at the beginning of the record to weeks of continuous breakouts or complete mobility of the landfast ice at the end of the record. This correlation overshadows other variables known to be important for breakout, like wind (Ford et al., 2006), and brings little insight to the process of breakout during the part of the season when breakout events occur sporadically, posing the greatest risk to ice users.

### ***Derived environmental variables***

The hourly re-analysis data acquired from the European Centre for Medium-Range Weather Forecasting (ECMWF) was averaged to a daily resolution to match the resolution of the binary breakout event variable. A derived variable, *accumulated degree days of melt* (ADDM) was also calculated from the ERA5 2 metre temperature. ADDM was calculated as the sum of daily average temperatures greater than 0°C, the melting temperature of the snow that covers the sea ice, beginning on April 1<sup>st</sup> each year.

Since breakout events can be driven by environmental conditions at the time of the event as well as influenced by conditions leading up to the event, two new categories of environmental variables were produced from the original 105 variables:

- 1) The 1- to 21-day antecedent mean values ('averages') for each of the ERA5 environmental variables were calculated [ $n_1 = 105 \times 21 = 2,205$ ], and
- 2) The 1- to 21-day antecedent values ('leads') for each of the ERA5 environmental variables were generated by lagging the data series from each variable. A lead value of 0 represents the conditions on the day-of the event/non-event [ $n_2 = 105 \times 22 = 2,310$ ].

This produced a final pool of 4,515 (2,205 + 2,310) environmental variables from the ERA5 re-analysis data alone.

Average and lead variables from 1 to 21 days were not considered for tide variables because the mechanical nature of tides and currents as a driver for breakout events makes them only important on the day-of the event, but the derivatives of the variables were

generated on the day of the observations. Since daily averages of tidal data are near zero, daily minimum and maximum values of elevation and u and v current components were extracted from the hourly WebTide variables (tide elevation and currents) to capture the amplitude of daily oscillations ( $n = 6$ ). This then resulted in a total of 4,521 environmental variables.

### **3.2.3 Significance of environmental variables**

The strength of the relationship between the binary breakout event variable and the continuous environmental variables for the breakout sub-season were determined using point-biserial correlation. The point-biserial correlation coefficient, which measures the strength of an association between a binomial and continuous variable, was calculated using the *ltm* library in R (Rizopoulos, 2018). To assess whether there were any spatial patterns, the point-biserial correlations between the binary breakout event variable and each of the original environmental variables were calculated for each grid cell from along and across transects of Admiralty Inlet (Figure 3.1). There were no observable differences in correlations among these grid cells, so for all further analyses all these grid cells were averaged together.

The point-biserial correlation coefficients ( $r$ ) were calculated between the binary breakout event variable and each spatially averaged environmental variable. A positive correlation indicates that days with breakout events are associated with increases in the magnitude of the environmental variable. The coefficients are negative in the opposite case, where days with breakout events are associated with decreases in the magnitude of

the environmental variable. The significance of the association was evaluated using a two-tailed test (Equation 3.1) that follows the Student t distribution (Sheskin, 2011).

$$t = \frac{r\sqrt{N^*-2}}{\sqrt{1-r^2}} \quad \text{Equation 3.1}$$

To account for serially-autocorrelated data (Afyouni et al., 2019), an effective sample size ( $N^*$ ; Equation 3.2) was calculated for each environmental variable from the lag-1 autocorrelation coefficients of the binary breakout event variable ( $r_1$ ) and the environmental variable ( $r_2$ ).  $N$  is the sample size.

$$N^* = N \frac{1-r_1r_2}{1+r_1r_2} \quad \text{Equation 3.2}$$

The p-value was obtained from the  $t$  statistic using the Student t distribution function in the *stats* library in R (R-core, 1969). The p-values were compared to  $\alpha = 0.10$  to assess their significance. Only correlations with p-values less than  $\alpha$  were considered for implementation in the empirical models because they have a low likelihood of committing a Type I error (Stoltzfus, 2011). Since this is a preliminary study, a relaxed  $\alpha$  was used to avoid excluding potentially significant factors from future analyses and to retain as many candidate predictors as possible for the logistic regression modelling. Additional investigation of each variable was conducted in the model-building stage where there were more stringent criteria for the suitability of environmental variables as predictors.

Including multiple similar variables in a model can cause mathematically unstable outcomes and decrease generalizability (Stoltzfus, 2011). To remove redundant candidate predictors, environmental variables with significant correlations with the binary breakout event variable were compiled in a Pearson correlation matrix. Colinear variables at a cut-off threshold of 0.7 were eliminated from contention, prioritizing retention of variables with the greater absolute point-biserial correlation coefficient. This reduced pool of non-colinear environmental variables was subsequently used as a set of independent predictors in a logistic regression model with greater confidence.

The remaining predictor variables were grouped into four categories based on their relationship to processes that are implicated in landfast ice deterioration. These categories are precipitation, radiation balance, non-radiative fluxes, and mechanical. First, several variables with difficult to interpret relationships with the binary breakout event variable were removed from the predictor pool. *Instantaneous large scale surface precipitation fraction* was removed because the relationship between the fraction of a grid cell and a breakout event is ambiguous. Fraction variables indicate a portion of the grid cell in which an event occurs, in this case large scale precipitation. *Mean vertically integrated moisture divergence*, was also removed. This variable is a component of evaporation and condensation models, but there are variables that directly deal with these, so the variables were removed. *Neutral wind at 10 m v-component* was removed because the unmodified equivalent (*10 metre V wind component*) is more easily described than neutral wind, which is related to the friction between the air and the surface, and the two are colinear. The *forecast logarithm of surface roughness for heat, maximum total precipitation rate since previous post-processing, total precipitation, mean eastward gravity wave surface*

*stress*, and *mean eastward turbulent surface stress* were all removed for similar reasons to the variables described above. *Precipitation type* is an ordinal variable, so it was removed so that it would not need to be dummy coded in the logistic regression model.

### **3.2.4 Logistic regression**

Before beginning the model building process, the pool of candidate predictors identified in Section 3.2.3 was carefully vetted to ensure that all the predictors had clear and meaningful relationships with breakout events. Any environmental variables whose correlation with the binary breakout event variable could not be explained physically were removed from the predictor pool. There were many predictors in the pool with long-leads of 8 to 21 days. This far ahead of a breakout event, the relationship identified by the correlation tests may well be due to a spurious relationship that may not be generalizable. Considering this, two candidate predictor pools were created. The first included all the predictors, and the second included only predictors with lead times of 7 days or less.

A logistic regression model was generated from each of the two candidate predictor pools using the generalized linear model function from the *stats* library in R (R-core, 1969), starting with a saturated model (including all predictors in the candidate predictor pool). To reduce the number of predictors in each model and achieve an acceptably parsimonious model (i.e., one predictor to a minimum of ten positive observations in the binary breakout event variable), the predictors were evaluated using the  $\chi^2$  statistic (Section 2.2.1). The ANOVA function from the *car* library in R (Fox, 2020) was used with a type II Wald test to determine the significance of each predictor (Hosmer et al.,

2013; Osborne, 2017). For each model, one predictor at a time, predictors with the largest  $\chi^2$  p-values were removed and then the model was re-trained with the remaining predictors until all the  $\chi^2$  p-values were less than  $\alpha = 0.1$ . The threshold for  $\alpha$  was set to 0.1, a more permissive threshold, to ensure that the fit of the model does not degrade due to a scarcity of model parameters and to enhance model skill (Hosmer et al., 2013). Once the  $\chi^2$  p-values of all the remaining predictors were below  $\alpha = 0.1$ , the rejected candidate predictors were added back into the model, one at a time, to determine if they were significant in a reduced predictor pool. If they were, they were re-added to the model, if not, they were removed once again. Long-lead and short-lead benchmark logistic regression models were trained and validated using the complete dataset to assess the best possible performance of the logistic regression approach. These models were also recreated using z-scores (Equation 3.3) of the predictor values ( $x$ ) so that the logistic regression coefficients would be comparable, and the relative influences of the environmental predictors could be interpreted.

$$Z = \frac{x-\mu}{\sigma}, \quad \text{Equation 3.3}$$

where  $\mu$  is the mean and  $\sigma$  is the standard deviation of the variable.

### *Assumptions of logistic regression*

Before the logistic regression models could be assessed, several key assumptions of binary logistic regression modelling needed to be addressed (Section 2.2.2). These

assumptions are that there is a binary response variable, little to no multicollinearity in the predictors, independent error within the predictors, there are no strongly influential data points, and each predictor has a linear relationship with the logit of the response variable (Hosmer et al., 2013; Ottenbacher et al., 2004; Stoltzfus, 2011). The first two criteria were addressed in Section 3.2.3. Since multicollinearity was addressed and there are no replicated observations which would result in pseudoreplication, however temporal autocorrelation is likely present in the environmental variables. Therefore, model error of the predictors may not be independent (Stoltzfus, 2011). The presence of strongly influential data points was determined by examining the standardized residuals and removing those data points greater than 3 standard deviations (Stoltzfus, 2011).

There were no values in the dataset with absolute standardized residuals greater than 3 standard deviations, so no data points needed to be removed. The relationship between each predictor and the logit of the response variable was assessed visually using scatter plots (Hosmer et al., 2013; Ottenbacher et al., 2004; Stoltzfus, 2011). The logit of each data point was calculated using Equation 2.3, whereby the logit for each outcome is calculated as  $\log\left(\frac{p(x)}{p(x)-1}\right)$ , where  $p$  is the probability of a breakout event occurring, as predicted by the model. This was plotted against the values of each of the predictors and a loess function was overlain on each plot to approximate trends in the relationship.

Predictors that were not approximately linear were log-transformed following an offset of  $1 \times 10^{-22}$  to remove zero values. Only variables that were both linear and significant post-transformation were retained in the models. Additional criteria outlined in Section 2.2.2 were followed as closely as possible.

### ***Model performance and validation***

Logistic regression calculates the probability of an event occurring; however, this cannot be directly compared to the binary breakout event variable to assess model skill. The receiver operating characteristic (ROC) was calculated by iterating through probabilities from 0.01 to 0.99 at increments of 0.01 (Section 2.3.1). At each iteration, the probability was used as the decision threshold above which an event is forecast, thereby converting the probability calculated by the model into a binary prediction of a breakout event occurring or not. The Hit Rate (H, ratio of correct predictions of breakout to the total number of breakout events forecast) and False Alarm Rate (F, ratio of incorrect predictions of non-events to the total number of non-events forecast) were calculated at each iteration, the ROC was calculated as the area under the curve plotted for H vs. F. The closer the ROC is to 1, the greater the skill in detecting the event signal while minimizing false positives. This optimized decision threshold corresponds to the greatest Peirce Skill Score (PSS) along the ROC curve.

Measures including the Hit Rate, False Alarm Rate and Symmetric Extremal Dependency Index (SEDI) were calculated based on the binary model output. SEDI is a non-degenerate skill metric used for both rare and overwhelmingly common events (Hogan & Mason, 2011). Non-degenerate means that the score will not trend towards a meaningless base value if the observed rate of occurrence of an event is extremely small or large (Hogan & Mason, 2011). This makes it an ideal measure to assess the skill of a model of breakout events because they are relatively rare. The goodness of fit of the models was assessed using McFadden's pseudo  $R^2$  statistics and the Hosmer-Lemeshow test (Section 2.2.1).

To evaluate the severity of overfitting in the original model, several cross-validation frameworks were implemented to assess the shrinkage of the performance measures for the benchmark model. A bootstrap scheme was implemented that subsampled 1000 different 70% training to 30% validation datasets and a logistic regression base model was trained and validated for each subsample. The average performance measures from each base model were used to represent a more realistic evaluation of model skill and determine the relative shrinkage, a measure of overestimation bias (a.k.a., “optimism”), expected for the benchmark model (Iba et al., 2021). To represent cases on a year-by-year basis, training and validation datasets were sampled using a leave-one-year-out (LOYO) cross-validation method, like Zhao et al. (2012). In this scheme, a model was trained on data from all but one year from 2000 to 2020. Each of these 21 models was then validated against the year that was left out of the training dataset. This cross-validation method made more data points available for model training and enhanced assessment of model performance by looking at model performance on independent years. Again, 2012 was omitted from the analysis because there were no breakout events and therefore no breakout season to validate a logistic regression model with.

The benchmark model was compared to a climatology model that consisted of the smoothed empirical probability derived from the breakout event histogram (Figure 4.4; and see Section 3.2.1). An ROC curve was constructed to identify the optimal decision threshold to convert probability to a binary decision of whether a breakout event will occur or not (see model building step above). Performance measures were calculated for the results of the climatology model to facilitate comparison to the logistic regression model.

### ***Auxiliary models***

To explore how predictors that were not included in the long-leads benchmark model could still contribute to the prediction of breakout, the remaining predictors were used to construct several auxiliary logistic regression models using the methods established above. The predictors that were implemented in an auxiliary model were removed from the predictor pool and the process was repeated if there was no evidence of poor fit (based on the Hosmer-Lemeshow statistic). SEDI was calculated for the auxiliary models and they were implemented as base models in an ensemble.

### ***Ensemble model***

An ensemble model that includes all the constructed auxiliary models was created by weighted summation of the predictions from a benchmark model and the auxiliary models in an ensemble (DelSole et al., 2017). This model was constructed using all the observations in the dataset, just like the benchmark logistic regression models. Inspired by DelSole et al. (2017), the weight of each model's prediction was determined by two parameters that were derived for each model (Equation 3.4). The first was how much each model's forecasted probability ( $p_m$ ), the output of each model expressed as a probability between 0 and 1, exceeded or was less than the probability decision threshold ( $w_m$ ), which indicates the relative strength of each probability prediction. The second was  $SEDI_m$ , which indicates relative confidence in distinguishing event signal from non-event noise in the model. The forecast ( $f$ ) was then calculated as:

$$f(L) = \sum_{m=1}^L (p_m - w_m) \times SEDI_m \quad \text{Equation 3.4}$$

$L$  is the number of auxiliary models that were constructed. The first parameter ( $p_m - w_m$ ) determines the sign of the prediction, negative predictions were in favour of a non-event forecast and positive predictions were in favour of an event forecast. The weight of the prediction was proportional to the product of both parameters. If the final summation of all the predictions was zero or negative, the forecast was a non-event, if it was positive, the forecast was an event.

## Chapter 4: Results

### 4.1 Landfast sea ice phenology

The deterioration of the Admiralty Inlet floe edge (Figure 4.1) begins with mobilization of sea ice in Lancaster Sound to the north. During the winter, sea ice fills Lancaster Sound, blocking the northern floe edge of Admiralty Inlet. Breakout events here do not occur until the Lancaster Sound ice has broken up. Only once the northern floe edge is exposed do breakout events occur. Typically, the sea ice in Lancaster Sound is fully mobile (no longer fastened to the shoreline) by April 1<sup>st</sup> (16/21 years in the data set), exposing the northern floe edge of Admiralty, allowing the episodic recession of the northern floe edge by breakout of ice floes. Recession continues as far south as Adam's Sound until ice at the southern end of the inlet deteriorates around Yeoman Island (Figure 2.2). At this point, the entirety of the remaining landfast ice becomes mobile (i.e., breakup) and sea ice south of Elwin Inlet drifts towards the south, and floes to the north drift into Lancaster Sound.

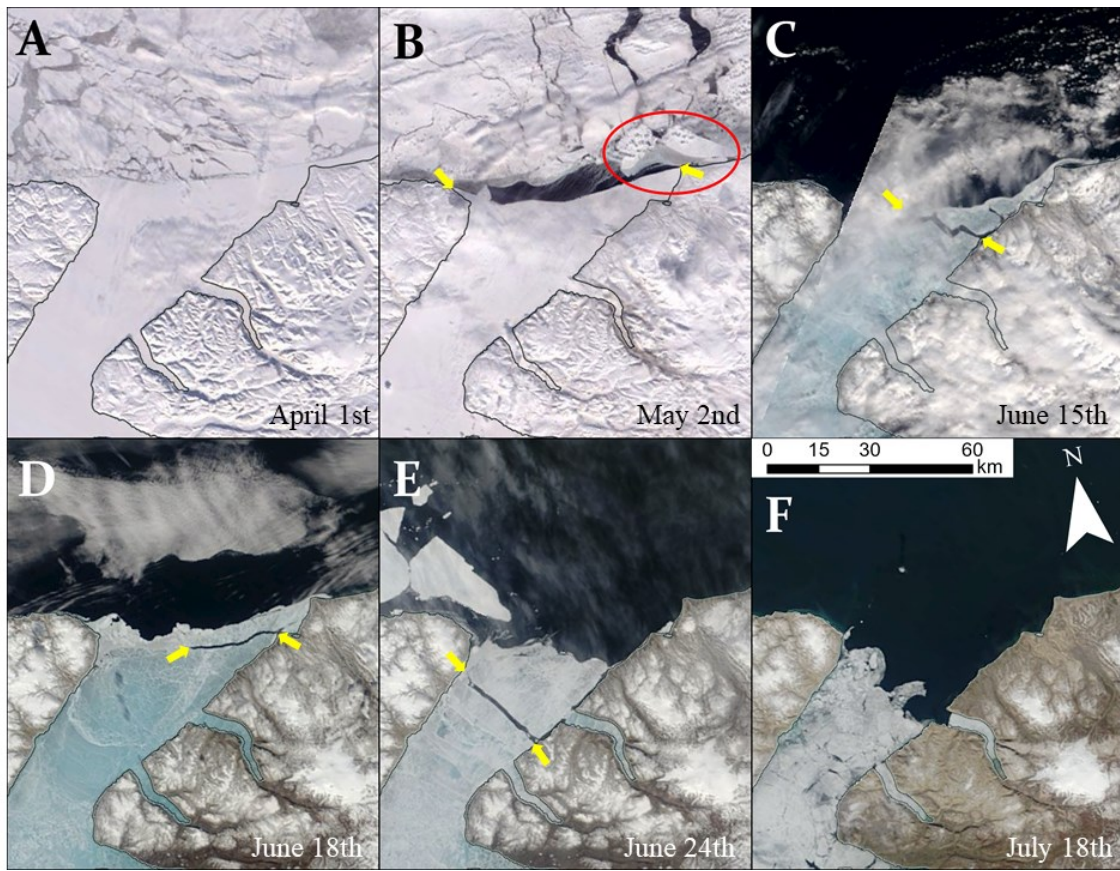


**Figure 4.1 MODIS imagery of the 2013 spring season landfast ice deterioration in Admiralty Inlet. The ends of the modified floe edge after breakout events are indicated by yellow arrows. (A) Ice in Lancaster Sound is completely mobile (fully mobilized in mid-March), but the northern floe edge is stable, so no breakout events had occurred yet (i.e., pre-breakout season). (B) The first breakout event of the year, marking the beginning of the breakout season. The northern floe edge is recessed compared to image A, and the ice floe that broke out can be seen to the east of the mouth of the inlet (circled in red). (C) and (D) Two breakout events contributing to the gradual recession of the northern floe edge. Flaw leads are observable as a darker strip of open water between the remaining landfast ice and the escaping mobile floe. (E) A “plug failure” that stranded hunters and tourists (Learns, 2016). (F) Ice in the inlet is fully mobile, complete breakup occurred on July 13<sup>th</sup> but was partially obscured by cloud in the MODIS imagery. We acknowledge the use of imagery from the NASA Worldview application (<https://worldview.earthdata.nasa.gov>), part of the NASA Earth Observing System Data and Information System (EOSDIS).**

An exception to the typical melt season progression is 2012, when Lancaster Sound broke up to the west and east of the mouth of Admiralty Inlet, but not directly north of the inlet. The ice in Lancaster Sound remained landfast up to the southern coast of Devon Island, which prevented breakout events from occurring. Rather than gradual recession of the floe edge from the north toward the south, the ice in the inlet remained stable until breakup of ice at the south of the inlet facilitated complete breakup of the landfast ice. Since breakout events at the northern floe edge never occurred, this year was omitted from further analyses.

From 2000 to 2020, 125 breakout events were observed between April 1<sup>st</sup> and the onset of breakup, an average of ~6 events per year (Appendix Table B.1). Within the breakout season, between the first breakout event and the onset of breakup, an average of 38 days with no breakout events were recorded each year. In Figure 4.2, a linear trend of the number of breakout events observed each year shows an overall increase between 2000 and 2020 of 0.32 breakout events per year, a total increase of ~6-7 events per year over the 21-year period.

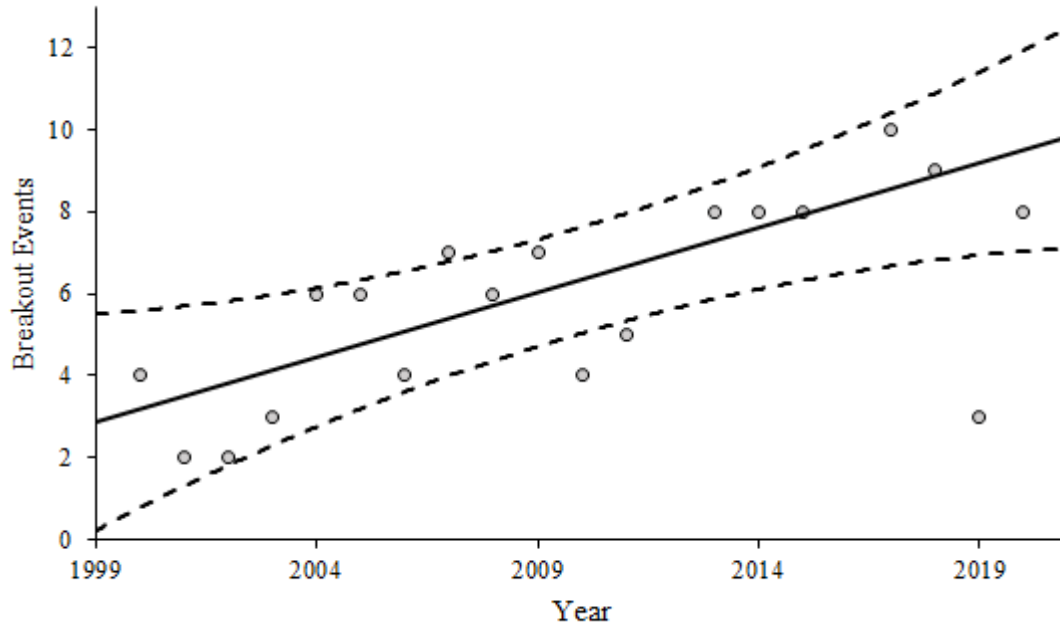


**Figure 4.2** Number of breakout events identified in satellite imagery each year (except 2012). Linear trend of the number of breakout events per year (solid line) and 95% confidence intervals about this line (dashed line) indicate an increase of 0.32 events per year ( $R^2 = 0.37$ ,  $p = 0.004$ ).

The timing of the first breakout occurred, on average, 46 days earlier between 2000 and 2020 (Figure 4.3). The onset of breakup (as defined in Section 3.2.2 and illustrated in Figure 3.4) also occurred earlier over the study period, advancing by ~9 days.

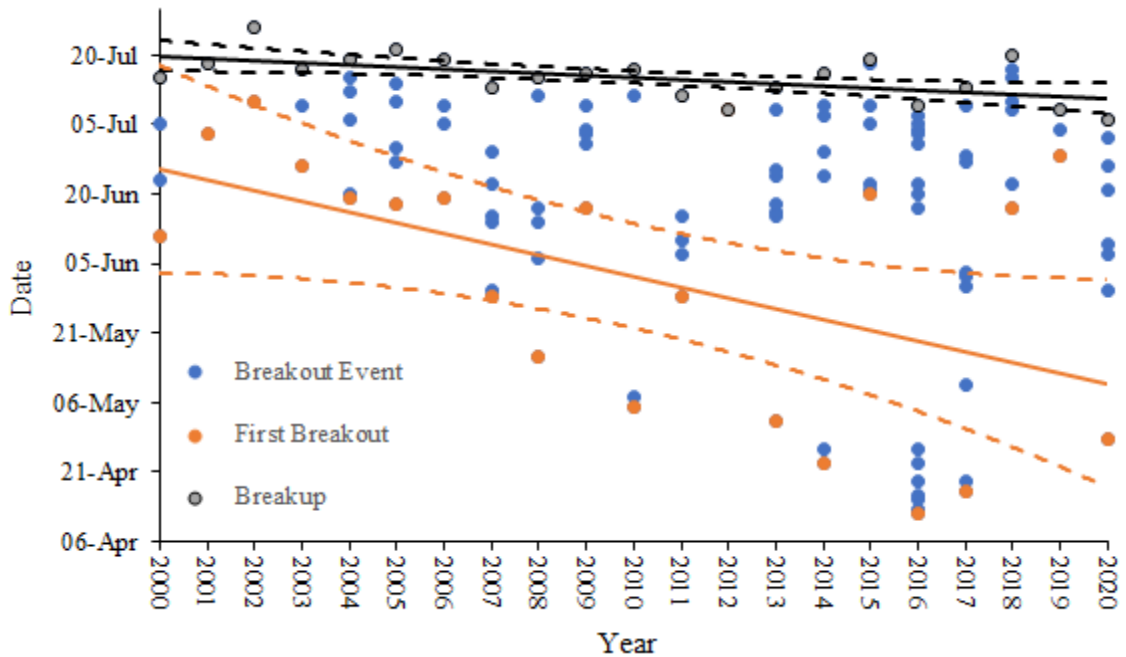


**Figure 4.3** Timing of breakout events identified in satellite imagery. Linear trends of the onset of breakup (black line) and the first breakout event (orange line) are plotted with their respective 95% confidence intervals (dashed lines). The linear trend for the first breakout event indicates an earlier occurrence of ~23 days per decade ( $R^2 = 0.25$ ,  $p = 0.02$ ). The linear trend for the onset of breakup indicates an earlier occurrence of ~4.6 days per decade ( $R^2 = 0.34$ ,  $p = 0.004$ ).

The breakout events are not uniformly distributed between the first breakout event and breakup. Although breakout events occurred as early as mid-April, most events occurred between mid-June and breakup (Figure 4.4). The 7-day moving average generated for the daily frequency distribution of events to create a climatology model to predict the most likely timing of breakout events in the spring season is presented in Figure 4.4. A decision threshold ( $w = 0.11$ ) was identified to convert the relative frequency to a binary prediction, using the same method as the logistic regression output in Section 3.2.4.

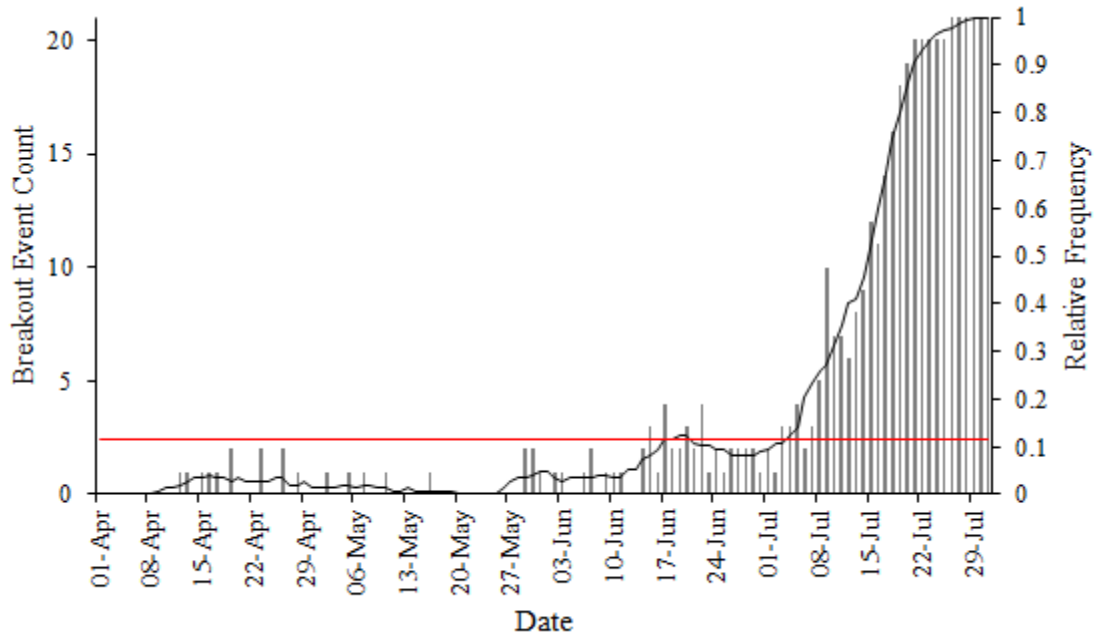


**Figure 4.4 Histogram of breakout events observed on each day of all spring seasons on record. This data series was smoothed with a 7-day moving average (black line). A decision threshold to determine the optimal probability associated with breakout events/no events is indicated by the horizontal red line ( $w=0.11$  relative frequency). Days above this threshold are considered as forecasted breakout events in the climatology model.**

On average, breakout events were  $275 \text{ km}^2$  and ranged from 7 to  $1463 \text{ km}^2$ . The relative size of breakout events in each location category along the northern floe edge in Admiralty Inlet is shown in Figure 4.5. The largest category of breakout events is the 29 plug failures, with a median area of  $\sim 518 \text{ km}^2$ . The difference of means between each category was tested using ANOVA. The mean of the plug events was significantly larger than the centre ( $p = 6.2 \times 10^{-3}$ ), east ( $p = 5.5 \times 10^{-6}$ ) and west ( $p = 4.2 \times 10^{-7}$ )

location categories. The second largest category of breakout events is in the centre of the northern floe edge, with a median size of  $\sim 126 \text{ km}^2$  across 18 events. The size of these events ranged substantially and were not significantly different from the east and west location categories. The third largest category, and the most numerous with 38 recorded events, is the east category, with a median size of  $119 \text{ km}^2$ . The east category is not significantly different from the western category, which is the smallest and least numerous with only 16 observed events, and a median size of  $49 \text{ km}^2$ .

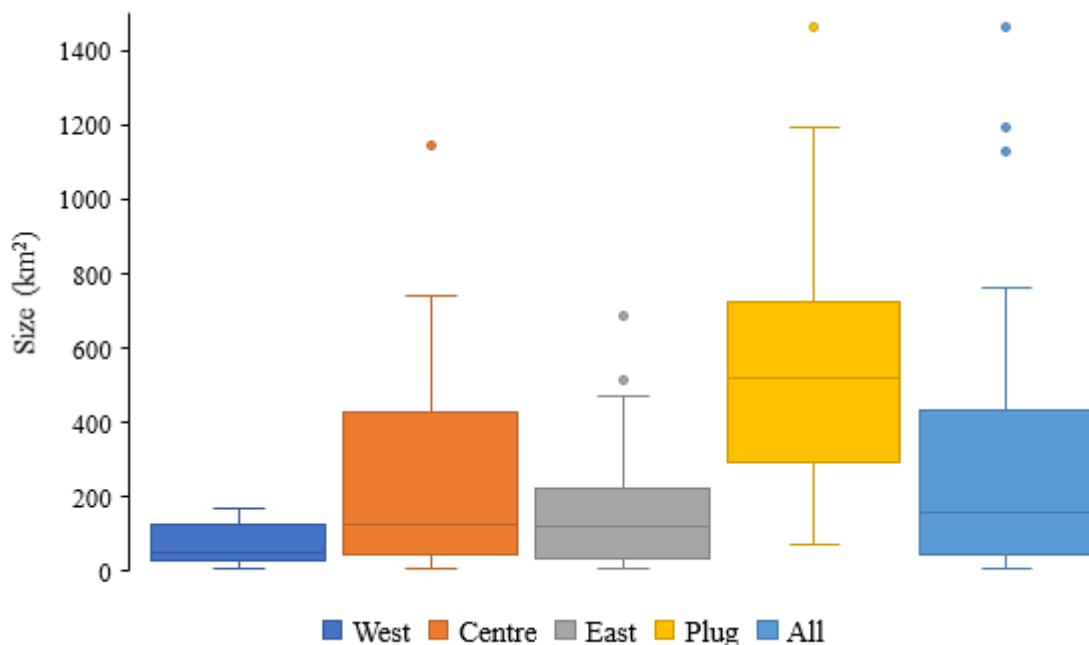


**Figure 4.5** Size of breakout events, categorized by location along the northern floe edge in Admiralty Inlet (West N = 16, Centre N = 18, East N = 38, Plug N = 29, All N = 101).

The relative timing of breakout events by location is illustrated in Figure 4.6. The plug failures consistently occur the latest during the breakout season, typically in late June to

mid-July (Figure 4.6). The median western breakout events also occur slightly later than the other two categories but can occur earlier in the season as well. The other two categories are not very different from one another and may occur at any time during the breakout season. The centre category is skewed towards later dates because most breakout events occur in June, but breakout events can occur as early as April, enough to lower the quartile of the centre category into late April.

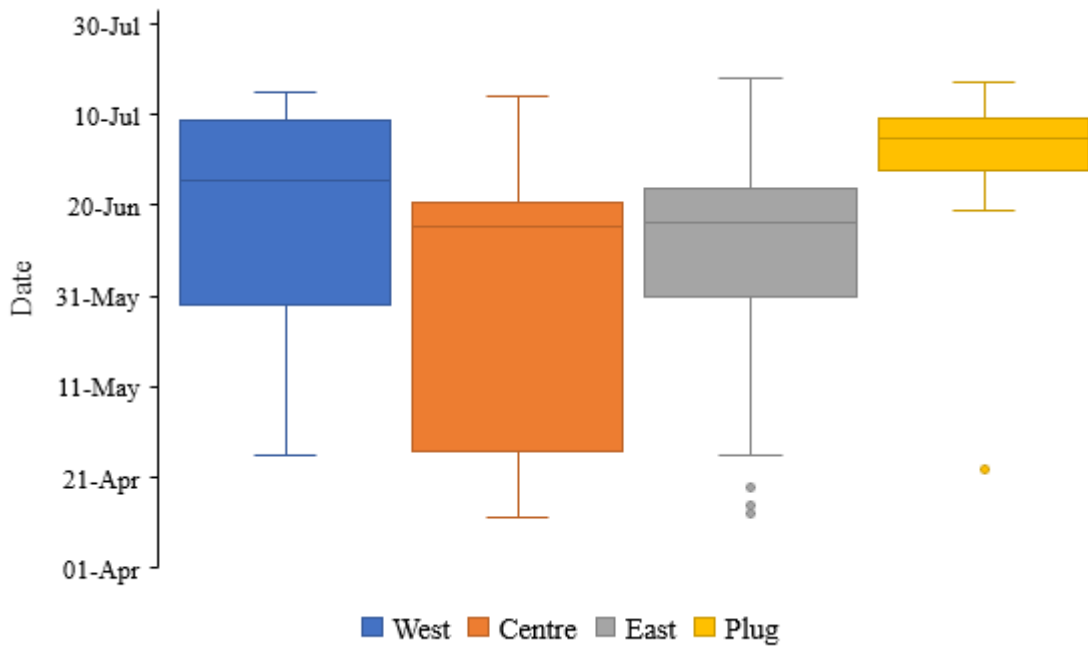


**Figure 4.6 The day-of-the year on which breakout events occurred, grouped by location along the northern floe edge in Admiralty Inlet.**

## 4.2 Significance of environmental variables

A total of 406 environmental variables that had a significant association ( $p < 0.10$ ) with the binary breakout event variables were identified from a pool of 4,515 variables from the ERA5 data set based on the point-biserial correlations (Appendix Table C.1). None of the WebTide variables were significantly correlated with the binary breakout event variable. Among the significant ERA5 environmental variables, there are 57 unique variables. Many of these variables are colinear with other environmental variables, which is obvious when inspecting patterns in the timing of the significant derived leads and averages. For example, *large-scale snowfall* and *large-scale snowfall rate water equivalent* were both positively correlated with the binary breakout event variable at a lag of 20 days ahead of the day of the event. Additionally, many variables that fall within the same categories (i.e., mechanical, non-radiative fluxes, radiation balance, and precipitation) share similar patterns. Precipitation variables related to snowfall all have negative correlations with the binary breakout event variable at leads of 19 to 20 days. Conversely, general precipitation and rainfall variables are positively correlated and are significant at all leads between the day of a breakout event and a lag of 18 days. 37 environmental variables with absolute collinear correlations less than 0.7 with any other remaining predictor were identified with a Pearson collinearity matrix (Table 4.1).

**Table 4.1 Reduced predictor pool of 37 environmental variables with significant point-biserial correlation with the binary breakout event variable after removing multicollinear variables.**

	Variable Name	Derivatives	Point-Biserial Correlation	p-value
Mechanical	Neutral wind at 10 m u-component	5-day lead	0.06	$9 \times 10^{-2}$
	10 metre V wind component	1-day lead	0.06	$9 \times 10^{-2}$
	10 metre U wind component	3-day lead	-0.07	$4 \times 10^{-2}$
		6-day lead	0.06	$9 \times 10^{-2}$
	Mean sea level pressure	3-day lead	-0.08	$3 \times 10^{-2}$
		13-day lead	-0.08	$4 \times 10^{-2}$
	Surface pressure	8-day average	-0.06	$1 \times 10^{-1}$
Precipitation	Convective precipitation	13-day lead	0.10	$3 \times 10^{-3}$
		16-day lead	0.06	$8 \times 10^{-2}$
	Convective rain rate	3-day lead	0.08	$2 \times 10^{-2}$
		14-day lead	0.08	$6 \times 10^{-2}$
		15-day lead	0.07	$1 \times 10^{-2}$
	Convective snowfall rate water equivalent	14-day lead	0.07	$4 \times 10^{-2}$
		16-day lead	0.08	$1 \times 10^{-2}$
	Large scale precipitation	19-day lead	-0.07	$5 \times 10^{-2}$
	Mean convective snowfall rate	13-day lead	0.08	$2 \times 10^{-2}$
		19-day lead	-0.06	$7 \times 10^{-2}$
	Mean large scale precipitation rate	Day-of	0.06	$7 \times 10^{-2}$
	Snowfall	20-day lead	-0.07	$6 \times 10^{-2}$
	Total column rainwater	6-day lead	0.07	$6 \times 10^{-2}$
		7-day lead	0.11	$3 \times 10^{-3}$
		8-day average	0.11	$6 \times 10^{-3}$
Total precipitation	20-day lead	-0.06	$8 \times 10^{-2}$	
	3-day average	0.11	$5 \times 10^{-3}$	
Non-radiative fluxes	Instantaneous surface sensible heat flux	5-day lead	-0.06	$8 \times 10^{-2}$
		17-day lead	-0.06	$9 \times 10^{-2}$
	Potential evaporation	14-day lead	-0.06	$1 \times 10^{-1}$
	Snow evaporation	Day-of	0.07	$6 \times 10^{-2}$
Radiation Balance	Mean surface direct short-wave radiation flux	21-day lead	0.07	$8 \times 10^{-2}$
		3-day average	-0.10	$1 \times 10^{-2}$
	Mean surface net long-wave radiation flux	20-day lead	-0.07	$5 \times 10^{-2}$
	Snow albedo	Day-of	0.06	$1 \times 10^{-1}$
	Surface net thermal radiation	Day-of	0.08	$3 \times 10^{-2}$
		3-day average	0.12	$2 \times 10^{-3}$
	Surface net thermal radiation, clear sky	3-day lead	0.06	$9 \times 10^{-2}$
	Surface thermal radiation downwards	3-day average	0.07	$6 \times 10^{-2}$
Total sky direct solar radiation at surface	20-day lead	0.11	$3 \times 10^{-3}$	

### 4.3 Logistic regression

The 37 significant environmental variables identified using the point-biserial correlation and the Pearson correlation matrix were implemented in a logistic regression model (Table 4.1). Manual backwards regression based on the  $\chi^2$  statistic reduced the number of predictors to 9. The linearity assumption of logistic regression was assessed for all 9 variables together (Figure 4.7). All predictors were confirmed to have linear relationships with the logit of the outcome of the model except for the precipitation predictors, which were log-transformed to produce a linear relationship with the logit of the model's outcome. This reduced variance of the outcomes of the model by increasing the minimum value of the logit from  $\sim -30$  to  $\sim -4$ . After transformation, the *convective rain rate* as a 3-day lead and *total column rainwater* as a 7-day lead were no longer significant in the model (according to the  $\chi^2$  p-values) and were removed (Table 4.2). The resulting 7-predictor model is hereafter referred to as the long-leads benchmark model because it includes all possible derived leads and averages for the environmental predictors implemented in it. A second model that only included leads of 7 days or less, included just 5 predictors. All 5 of the predictors in the short-leads benchmark model were also present in the long-leads benchmark model. After the linearity test, *convective rain rate* as a 3-day lead was no longer significant so it was removed from the model, leaving just 4 predictors (Table 4.3). This model is hereafter referred to as the short leads benchmark model.

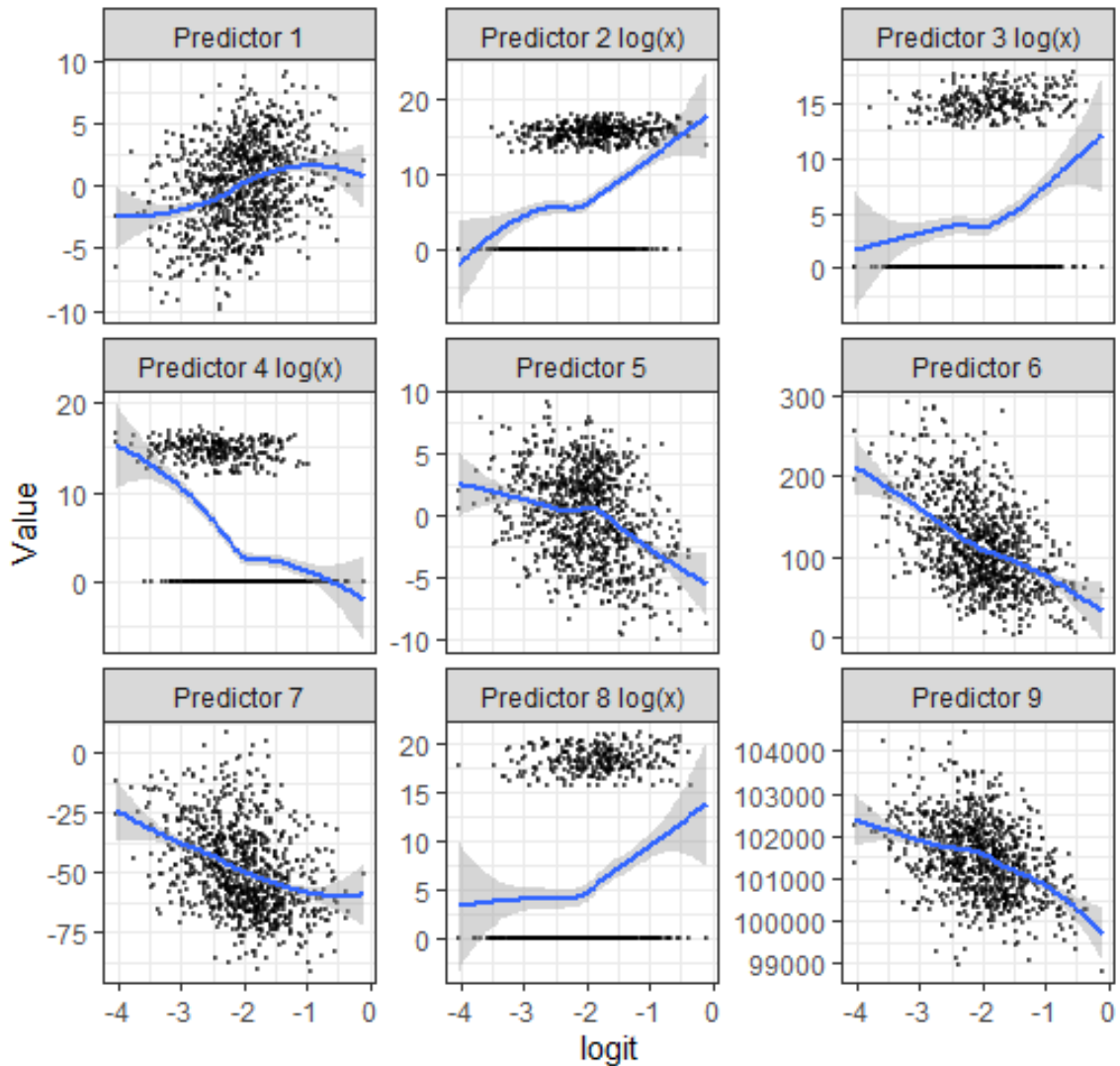


Figure 4.7 Plot of the linear relationships between the value of each predictor and the logit of the model outcome. The blue line is a smoothed loess function, and the grey area indicates the error of the function. Predictors with  $\log(x)$  in the name underwent a logarithmic transformation to create a linear relationship with the logit. Predictor key: Predictor 1 - neutral wind at 10 m u-component (5-day lead); Predictor 2 -  $\log(x)$  convective precipitation (13-day lead); Predictor 3 -  $\log(x)$  convective rain rate (3-day lead); Predictor 4 -  $\log(x)$  mean convective snowfall rate (19-day lead); Predictor 5 - 10 metre U wind component (3-day lead); Predictor 6 - mean surface direct short-wave radiation flux (3-day average); Predictor 7 - mean surface net long-wave radiation flux (20-day lead); Predictor 8 -  $\log(x)$  total column rainwater (7-day lead); Predictor 9 - mean sea level pressure (3-day lead).

**Table 4.2 Logistic regression parameters for the seven predictors in the benchmark long-leads logistic regression model (ROC = 0.67, w = 0.13, McFadden's pseudo R<sup>2</sup> = 0.053). Coeff = regression coefficient ( $\beta$ ), Std. Err. = standard error on the regression coefficient, z = z-value on the regression coefficient, 95% CI = 95% confidence interval, Z Coeff. = regression coefficient of the z-value transformed data set, Z Std. Err. = standard error on the regression coefficient of the z-value transformed data set, p [ $\chi^2$ ] = p-value of the  $\chi^2$  statistic.**

Variable (derivative)	Coeff.	Std. Err.	z	95% CI		Z Coeff.	Z Std. Err.	$\chi^2$	p [ $\chi^2$ ]
Intercept ( $\beta_0$ )	$2.3 \times 10^1$	$1.3 \times 10^1$	1.8	$-1.4 \times 10^0$	$4.8 \times 10^1$	-2.02	0.11	-	-
Neutral wind at 10 m u-component (5-day lead)	$7.0 \times 10^{-2}$	$3.0 \times 10^{-2}$	2.3	$1.1 \times 10^{-2}$	$1.3 \times 10^{-1}$	0.25	0.11	5.4	0.020
log(x) Convective precipitation (13-day lead)	$3.3 \times 10^{-2}$	$1.4 \times 10^{-2}$	2.4	$6.3 \times 10^{-3}$	$5.9 \times 10^{-2}$	0.26	0.11	5.9	0.015
log(x) Mean convective snowfall rate (19-day lead)	$-3.8 \times 10^{-2}$	$1.7 \times 10^{-2}$	-2.2	$-7.1 \times 10^{-2}$	$-4.1 \times 10^{-3}$	-0.25	0.12	4.8	0.028
10 metre U wind component (3-day lead)	$-6.0 \times 10^{-2}$	$2.8 \times 10^{-2}$	-2.2	$-1.1 \times 10^{-1}$	$-5.4 \times 10^{-3}$	-0.22	0.10	4.6	0.031
Mean surface direct short-wave radiation flux (3-day average)	$-4.6 \times 10^{-3}$	$2.1 \times 10^{-3}$	-2.2	$-8.7 \times 10^{-3}$	$-5.4 \times 10^{-4}$	-0.25	0.11	4.9	0.026
Mean surface net long-wave radiation flux (20-day lead)	$-1.2 \times 10^{-2}$	$5.9 \times 10^{-3}$	-2.1	$-1.4 \times 10^{-1}$	$-1.1 \times 10^{-1}$	-0.22	0.10	4.5	0.034
Mean sea level pressure (3-day lead)	$-2.5 \times 10^{-4}$	$1.2 \times 10^{-4}$	-2.0	$-4.9 \times 10^{-4}$	$-6.3 \times 10^{-6}$	-0.22	0.11	4.0	0.044

**Table 4.3 Logistic regression parameters for the four predictors in the benchmark short-leads logistic regression model (ROC = 0.63, w = 0.14, McFadden's pseudo  $R^2 = 0.030$ ). Coeff = regression coefficient ( $\beta$ ), Std. Err. = standard error on the regression coefficient, z = z-value on the regression coefficient, 95% CI = 95% confidence interval, Z Coeff. = regression coefficient of the z-value transformed data set, Z Std. Err. = standard error on the regression coefficient of the z-value transformed data set, p [ $\chi^2$ ] = p-value of the  $\chi^2$  statistic.**

Variable (derivative)	Coeff.	Std. Err.	z	95% CI		Z Coeff.	Z Std. Err.	$\chi^2$	P [ $\chi^2$ ]
Intercept ( $\beta_0$ )	$-1.4 \times 10^0$	$2.4 \times 10^{-1}$	-6.1	$-1.5 \times 10^0$	$-1.4 \times 10^0$	-1.96	0.10	-	-
Neutral wind at 10 m u-component (5-day lead)	$7.1 \times 10^{-2}$	$3.0 \times 10^{-2}$	2.4	$1.2 \times 10^{-2}$	$1.3 \times 10^{-1}$	0.25	0.11	5.5	0.019
10 metre U wind component (3-day lead)	$-6.9 \times 10^{-2}$	$2.8 \times 10^{-2}$	-2.5	$-1.2 \times 10^{-1}$	$-1.4 \times 10^{-2}$	-0.25	0.10	6.0	0.014
Mean surface direct short-wave radiation flux (3-day average)	$-5.7 \times 10^{-3}$	$2.0 \times 10^{-3}$	-2.9	$9.7 \times 10^{-3}$	$-1.8 \times 10^{-3}$	-0.30	0.11	8.2	0.004
log(x) Total column rain water (7-day lead)	$2.1 \times 10^{-2}$	$1.1 \times 10^{-2}$	1.9	$-1.1 \times 10^{-3}$	$4.4 \times 10^{-2}$	0.18	0.10	3.5	0.063

Eight unique predictors were implemented in the final long- and short-lead benchmark models. *Neutral wind at 10 m u-component* ( $\text{m s}^{-1}$ ) and *10 metre U wind component* ( $\text{m s}^{-1}$ ) are the eastward components of wind at a height of 10 m (ECMWF, 2021; Hersbach et al., 2018). These predictors are positive when the surface stress is towards the east and negative when it is towards the west. Neutral wind at 10 m was found to be most significant as a 5-day lead and has positive relationship with the binary breakout event variable. Neutral wind, sometimes called the friction layer, is wind that exchanges momentum with the surface. The direction is the same as surface stress and is proportional to surface stress and the roughness length of the surface. Standard wind at 10 m is most significant as a 3-day lead and has a negative correlation with the binary breakout event variable.

*Convective precipitation* (m) is the daily average of rain and snow that falls to the Earth's surface in one hour (ECMWF, 2021; Hersbach et al., 2018). A logarithmic transformation was applied to this predictor to produce a linear relationship between the variable and the logit of the outcome. This predictor is most significant as a 13-day lead and has a positive relationship with the binary breakout event variable.

*Mean convective snowfall rate* ( $\text{kg m}^{-2} \text{s}^{-1}$ ) is the average intensity of snowfall (ECMWF, 2021; Hersbach et al., 2018). A logarithmic transformation was applied to this predictor to produce a linear relationship between the variable and the logit of the outcome. This predictor is most significant as a 19-day lead and has a negative relationship with the binary breakout event variable.

*Mean surface direct short-wave radiation flux* ( $\text{W m}^{-2}$ ) is the average short-wave radiation flux at the surface. Vertical fluxes are positive downwards (ECMWF, 2021; Hersbach et al., 2018). This predictor is most significant as a 3-day average and has a negative correlation with the binary breakout event variable.

*Mean surface net long-wave radiation flux* ( $\text{W m}^{-2}$ ) is the average long-wave radiation flux at the surface. Vertical fluxes are positive downwards (ECMWF, 2021; Hersbach et al., 2018). This predictor is most significant fourteen days ahead of a breakout event and has a positive correlation with the binary breakout event variable.

*Mean sea level pressure* (Pa) is the pressure of the atmosphere adjusted to the height of mean sea level. Mean sea level pressure is used to identify low- and high-pressure systems (ECMWF, 2021; Hersbach et al., 2018). It is most significant as a twelve-day average ahead of a breakout event and has a negative correlation with the binary breakout event variable.

*Total column rain water* ( $\text{kg m}^{-2} \text{ s}^{-1}$ ) is the amount of water that forms droplets in a column that extends from the surface of the Earth to the top of the atmosphere (ECMWF, 2021; Hersbach et al., 2018). A logarithmic transformation was applied to this predictor to produce a linear relationship between the variable and the logit of the outcome. This predictor is most significant as a 7-day lead and has a positive correlation with the binary breakout event variable.

Assessing model fit for the long-leads benchmark model, McFadden’s pseudo  $R^2$  statistic for the long-leads benchmark model is low at 0.053, but the Hosmer Lemeshow p-value is much greater than 0.05 (Table 4.4), which indicates that there is no evidence of poor fit. The modelled and expected outcomes in each decile are close, which corroborates the interpretation of the Hosmer-Lemeshow statistic. The ROC of this model is 0.67, so despite having a good fit to the data, the skill in distinguishing signal from noise is poor (not much better than a coin flip). An ROC greater than 0.7 would be acceptable, so it is close but is below the accepted performance threshold.

**Table 4.4 Modelled and expected observation frequencies from the long-leads benchmark model within each decile of probability for breakout events, coded as 1, and non-events, coded as 0. The Hosmer-Lemeshow  $\chi^2$  is 3.5, with 8 degrees of freedom and a p-value of 0.89.**

Decile	Probability Cut Point	Events = 1		Non-events = 0	
		Modelled	Expected	Modelled	Expected
1	0.02	3.9	5	89.1	88
2	0.06	6.0	5	86.0	87
3	0.07	7.6	8	84.4	84
4	0.09	8.9	9	83.1	83
5	0.12	10.3	7	81.7	85
6	0.14	11.7	14	80.3	78
7	0.15	13.3	13	78.7	79
8	0.18	15.2	12	76.8	80
9	0.22	18.4	21	73.6	71
10	0.49	26.8	28	65.2	64

Assessing model fit for the short-leads benchmark model, McFadden’s pseudo  $R^2$  statistic for the short-leads benchmark model is even lower than the long-leads benchmark model

at 0.030, which indicates a poorer fit. The Hosmer Lemeshow p-value is less than 0.05 at 0.049 (Table 4.5), indicating a poor fit, which is corroborated by the low pseudo  $R^2$  value. The modelled and expected outcomes in each decile are not close, which corroborates the interpretation of the Hosmer-Lemeshow statistic. The ROC is lower than the long-leads benchmark model at 0.63, so the skill in distinguishing signal from noise is poor and is not as close to the acceptable threshold of 0.7. Despite the poor ROC, both models outperform the climatology model, which had a receiver operating characteristic (ROC) of 0.58, which is not considered to have a greater ability to distinguish signal from noise than a coin flip (Hogan & Mason, 2011; Hosmer et al., 2013).

**Table 4.5 Modelled and expected observation frequencies from the short-leads benchmark model within each decile of probability for breakout events, coded as 1, and non-events, coded as 0. The Hosmer-Lemeshow  $\chi^2$  is 15.6, with 8 degrees of freedom and a p-value of 0.049.**

Decile	Probability Cut Point	Events = 1		Non-events = 0	
		Modelled	Expected	Modelled	Expected
1	0.03	5.4	9	87.6	84
2	0.07	7.3	10	84.7	82
3	0.09	8.8	5	83.2	87
4	0.10	9.9	13	82.1	79
5	0.11	10.9	6	81.1	86
6	0.12	11.9	5	80.1	87
7	0.14	13.3	16	78.7	76
8	0.15	14.9	13	77.1	79
9	0.17	17.2	19	74.8	73
10	0.21	22.4	26	69.6	66

The performance measures of all the models that were developed are summarized in Table 4.6. The symmetric extremal dependence index (SEDI) of the benchmark models is better than the climatology model, at 0.39 and 0.33 for the long-leads and short-leads benchmark models, respectively, in comparison to 0.28 for the climatology model. The shrinkage of the benchmark models, approximated by the 1000 model bootstrap scheme, yielded an average SEDI of 0.27 and 0.24 for the long and short-leads models, respectively; both are lower than the climatology model. In the short-leads model, both the hit rate and false alarm rate are lower than the climatology model. Based on the results of the bootstraps, the expected shrinkage is 27-31%. In the long-leads model, the hit rate is greater than the climatology model, but so is the false alarm rate, reflecting the logistic regression model's poor ability to distinguish signal from noise ( $ROC < 0.7$ ). In subsequent analyses, the short-leads model will no longer be discussed due to its very poor performance in all the measures discussed above.

The SEDI results of the LOYO cross validation scheme for the long-leads model are quite variable. Some extreme results are 2000, 2001 and 2011, which have SEDI values approaching 1 because they correctly forecast all the breakout events in those years. The SEDI in 2003 approaches -1, because there were no hits. The average SEDI of the LOYO models is less than the bootstrap, at 0.23, which is a shrinkage of 41%. Across these models, the number of observations available for validation is lower than in the bootstrap scheme, so they are less representative of the shrinkage of the model. However, they are representative of how a logistic regression model might perform in an individual breakout season.

**Table 4.6 Summary of performance measures for the climatology probability density function and logistic regression results, including the bootstrap and leave-one-year-out (LOYO) cross validation schemes. Abbreviations: symmetric extremal dependence index (SEDI); hit rate (H); false alarm rate (F); hits (a); false alarms (b); misses (c); correct rejections (d). → = approaching.**

Model	SEDI	H	F	a	b	c	d
Climatology	0.28	0.5	0.31	61	244	61	555
Long-leads Benchmark	0.39	0.68	0.40	83	319	39	480
Short-leads Benchmark	0.33	0.57	0.34	70	272	52	527
Bootstrap <sub>Long-leads</sub>	0.27	0.56	0.37	20	89	16	150
Bootstrap <sub>Short-leads</sub>	0.24	0.47	0.30	17	73	19	167
Average <sub>LOYO Long-leads</sub>	0.23	0.56	0.39	64	311	55	488
2000 <sub>LOYO</sub>	→1.00	1.00	0.32	4	10	0	21
2001 <sub>LOYO</sub>	→1.00	1.00	0.50	2	7	0	7
2002 <sub>LOYO</sub>	0.34	0.50	0.27	1	4	1	11
2003 <sub>LOYO</sub>	→-1.00	0.00	0.16	0	3	3	16
2004 <sub>LOYO</sub>	-0.16	0.33	0.44	2	11	4	14
2005 <sub>LOYO</sub>	0.38	0.67	0.39	4	11	2	17
2006 <sub>LOYO</sub>	0.35	0.50	0.26	2	7	2	20
2007 <sub>LOYO</sub>	0.61	0.85	0.41	6	16	1	23
2008 <sub>LOYO</sub>	0.25	0.57	0.39	4	22	3	34
2009 <sub>LOYO</sub>	0.16	0.33	0.23	2	5	4	17
2010 <sub>LOYO</sub>	-0.28	0.25	0.44	1	31	3	39
2011 <sub>LOYO</sub>	→1.00	1.00	0.41	5	16	0	23
2013 <sub>LOYO</sub>	0.39	0.75	0.48	6	31	2	34
2014 <sub>LOYO</sub>	0.02	0.43	0.41	3	31	4	44
2015 <sub>LOYO</sub>	0.04	0.43	0.40	3	10	4	15
2016 <sub>LOYO</sub>	-0.01	0.19	0.19	3	14	13	59
2017 <sub>LOYO</sub>	0.34	0.70	0.46	7	36	3	42
2018 <sub>LOYO</sub>	-0.05	0.50	0.54	3	15	3	13
2019 <sub>LOYO</sub>	0.06	0.67	0.63	2	5	1	3
2020 <sub>LOYO</sub>	0.12	0.50	0.42	4	26	2	36

Testing predictors that were not used in the long-leads benchmark model, six auxiliary models were constructed (Table 4.7). The number of predictors included in each subsequent auxiliary model decreased as predictors were removed from the predictor pool. The probability decision threshold remained relatively constant across all the models at 0.13 to 0.14. With fewer candidate predictors, the SEDI and ROC of each model decreased as well. Summary tables for the auxiliary models that were constructed are in Appendix D .

**Table 4.7 Measures of performance and fit for auxiliary models developed from unused predictors.**

Model	Predictors	Decision threshold ( $w$ )	Hosmer-Lemeshow $\chi^2$ [ $p$ ]	ROC	SEDI
Long-Leads Benchmark	7	0.13	3.5 [0.90]	0.67	0.39
Auxiliary 1	5	0.12	5.0 [0.76]	0.66	0.35
Auxiliary 2	4	0.18	5.7 [0.68]	0.63	0.35
Auxiliary 3	7	0.13	8.0 [0.44]	0.64	0.32
Auxiliary 4	2	0.14	11.0 [0.20]	0.59	0.22
Auxiliary 5	1	0.14	2.5 [0.96]	0.55	0.15
Auxiliary 6	1	0.13	6.9 [0.55]	0.56	0.15

The weighted ensemble model constructed from the long-leads benchmark model and the auxiliary models performs better than the long-leads benchmark model. The false alarm rate of the ensemble model is 0.32, which is better than the long-leads benchmark model's false alarm rate. The hit rate is 0.61, which is worse than the long-leads benchmark model's hit rate. The SEDI is 0.41, which is the best model performance of

any of the constructed models. Assuming the shrinkage of the performance measures is proportional to the shrinkage of the benchmark models (27-31%), a more accurate SEDI is 0.29 to 0.30, which is slightly better than the performance of the climatology model. Since there is no decision threshold for the ensemble model, ROC cannot be calculated for the ensemble model.

**Table 4.8 Yes/No forecast contingency table for the ensemble model (H = 0.61, F = 0.32).**

Event forecast	Event observed	
	Yes	No
Yes	75 (Hits)	254 (False alarms)
No	47 (Misses)	545 (Correct rejections)

## **Chapter 5: Discussion**

### **5.1 Landfast sea ice phenology in Admiralty Inlet**

Prior to this thesis, one of the only detailed studies of the springtime ice phenology in Admiralty Inlet was conducted by Enfotec Technical Services, covering the period between 1999 and 2003. They found that breakout events of the landfast sea ice in the inlet occurred as early as the third week of June, to the second week of July, and breakup (the complete mobilization of sea ice in the inlet) occurred between July 15<sup>th</sup> and 26<sup>th</sup>. In this thesis, the first breakout events of the season were observed between 2000 and 2003 as early as June 11<sup>th</sup>, over a week earlier than Enfotec (2003) reported. Although, throughout the 20 years studied, most breakout events occurred in mid-June or later.

Since the Enfotec (2003) study, the climatology has changed considerably, breakup now occurs an average of approximately 9 days earlier, and more startlingly, first breakout events occur an average of 23 days earlier per decade. This contrasts with the findings of Galley et al. (2012) who did not find any significant trend towards earlier breakup in the inlet between 1983 and 2009. This discrepancy may be due to changes not being statistically significant until after 2009. Breakout events have also become more numerous, increasing by approximately 5 events per year over the 21-year period. This supports the observations of local ice users who have stated that sea ice is becoming more unpredictable and hazardous to travel on during the spring season (Ford et al., 2006).

The Enfotec (2003) project also made observations of the relationship between tides and currents, and breakout events. They observed that eastward currents entering Admiralty

Inlet from Lancaster Sound flow south along the western edge of the inlet. The current then crosses west to east, north of Strathcona Sound, before flowing northeast back into Lancaster Sound. These currents cause floes from fractured landfast ice to drift into eastern Lancaster Sound and carry mobile ice floes into the inlet from western Lancaster Sound. This is corroborated by observations made in this thesis of mobile floes, as well as observations made by local ice users (Bell et al., 2019). Floes are only observed to drift northeast, rotating counterclockwise, north of Strathcona Sound. Additionally, breakout events that cause the southward regression of the northern floe edge do not progress south of Strathcona Sound, south of which the current appears to primarily flow south along the western shore, towards Yeoman Island. Since currents are driving the landfast sea ice southward in the inner inlet, despite being heavily fractured, the sea ice south of Strathcona Sound doesn't break up until the sea ice around Yeoman Island melts out.

The Enfotec report, as well as local ice users (Bell et al., 2019), also observed that high-risk periods coincided with spring tides, which are the highest tides that occur twice in each lunar cycle. The landfast ice foot grounds the floe in shallow waters and high tides can lift the ice foot, unfastening the ice from the shore, and stronger currents can help to shift the ice (Bell et al., 2019; Wadhams, 2000). Based on observations of satellite imagery between 2000 and 2003 (Figure 5.1), as many breakout events were observed around neap tide (low amplitude tide) [6 times] as were observed around the spring tide (high amplitude tide) [6 times]. Tides may have a role in breakout events occurring, however there is no resolvable relationship between spring tides breakout events. Not only do breakout events between 2000 and 2003 not line up with spring tides, but there is

also no significant relationship between maximum daily tide elevation and the binary breakout event variable throughout the entire 21-year data series. While spring tides may contribute to breakout, there is still substantial risk of a breakout event occurring at any point during the lunar cycle.

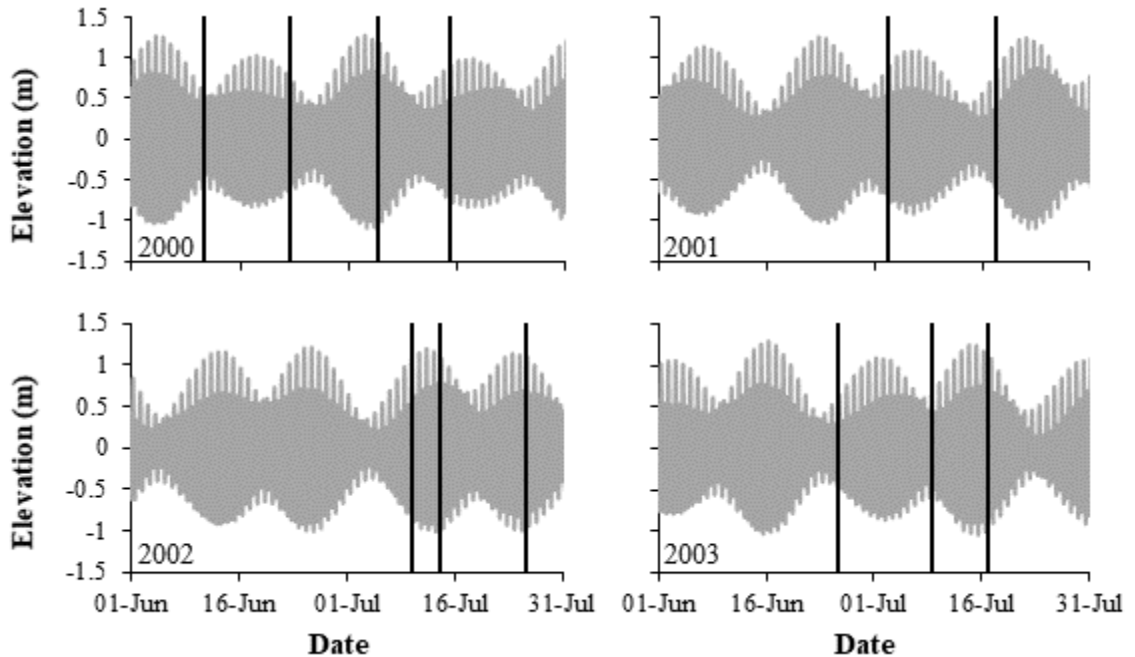


**Figure 5.1** Tide elevation (m) and breakout events (black vertical lines) observed in satellite imagery from June through July for 2000 to 2003.

The point-biserial correlation test did not resolve any significant relationship between tide elevation, tidal currents, and the binary breakout event variable. Since tides reverse twice each day, this precludes the ability to resolve a relationship between these semi-diurnal oscillations and breakout events, which are observed at a daily resolution due to the frequency of available satellite imagery. Since there is no relationship to spring and neap tides, breakout events occur when tidal amplitudes are both low and high, so

relationships to the tidal amplitude during neap tide would be overprinted by relationships to tidal amplitude during spring tides, which are much larger. It is therefore possible that there is a relationship with tide and current oscillations, but it cannot be resolved at the current temporal resolution.

The size and location of the floes that break free from the northern edge of the landfast ice is another important factor to consider, since larger breakout events might be more surprising to ice users (Bell et al., 2019), and certain locations along the floe edge might be considered safer than others. By definition, “plug” failures extend from the eastern to western shore of Admiralty Inlet (Loewen, 2020), so their greater size relative to other breakout events is unsurprising. On average, plug events also occur the later in the breakout season than other breakout events. This observation is consistent with interpretations by Loewen (2020), because plug failures require time for shore leads to form before the large floes can drift into Lancaster Sound. Shore leads form between the landfast ice and the shore, allowing the shore leads to unground from the shallow bed of the inlet near the shore. A large shore lead was observed every year along the western shore that is 1 to 3 km wide. Except for plug failures, breakout events that occur along the centre of the northern floe edge are the largest. In the absence of a shoreline to ground the landfast sea ice in the centre of the floe edge, when a flaw lead forms and conditions favour the floe drifting out into the open ocean, there is no additional resistance from the shore to prevent it from doing so, allowing larger floes to drift into Lancaster Sound. Breakout events occur most frequently on the eastern end of the floe edge. This aligns with Inuit Qaujimagatunangit (Bell et al., 2019) and the Enfotec (2003) reports, which describe northward currents along the eastern shore. This could contribute to smaller

breakout events occurring more frequently along the eastern end of the floe edge. The smallest and least frequent events occur along the western end of the floe edge, where the current flows south, helping to stabilize the floe edge and inhibiting breakout.

## 5.2 Significant environmental variables

Four hundred and six environmental variables were identified by the point-biserial correlation test that have a significant correlation with the binary breakout event variable (Appendix Table C.1). The signs of the correlations vary across the environmental variables as among the derived environmental variables (i.e., different leads and averages). The greatest absolute correlation between any environmental variable and the binary breakout event variable was 0.12, for *surface net thermal radiation* as a three-day average ahead of a breakout event. This is exceptionally low, and most variables have absolute correlations with the binary breakout event variable below 0.10, suggesting they have very little explanatory power. Despite the low correlations, potential cause-effect relationships are easily hypothesized.

At short leads and averages of 6 days or fewer, winds, radiation at the surface, and precipitation are significant. Winds are only significant in this short-lead interval leading up to a breakout event. Northward winds are positively correlated at a 1-day lead. Winds blowing toward the north drive the escaping floes northward into Lancaster Sound, but this only matters leading up to a breakout event, not once the breakout event has already occurred. These may also represent winds at the time of a breakout event due to the uncertainty in the recorded time of the breakout events. Since the timing of observed

breakout events were assigned to the date of the second image (see Section 3.2.1), it is possible that the 1-day lead is capturing the relationship to winds at the true timing of the breakout event (i.e., slightly earlier than the attributed timing). Eastward winds at 5- and 6-day leads were also positively correlated with the binary breakout event variable and would help to dislodge escaping floes from the floe edge if the escaping floe isn't grounded on the eastern shore. The westward winds are positively correlated with the binary breakout event variable at a 3-day lead. This may help to unground floes from the eastern shore, where a large shore lead, like the one in the west, has not been observed to form yet. This agrees with observations made by ice users in the inlet, that wind changes are potentially linked with unexpected deterioration of the floe edge (Bell et al., 2019; Ford et al., 2006). Additionally, the negative correlation of air pressure variables in this lead range indicates a possible association with the passage of synoptic low-pressure systems (i.e., storms), which would produce stronger, more unpredictable winds.

At short leads ahead of a breakout event (less than 7 days), short-wave radiation at the surface is negatively correlated with the binary breakout event variable, and long-wave radiation at the surface is positively correlated with it. It is likely that at these short leads, the significance of radiation at the surface is not their contribution to melting of the ice cover, but as indicators of the presence of storms via cloud cover. The negative correlation with solar radiation is likely due to the presence of cloud cover, which blocks sunlight. Under cloud conditions, long-wave radiation is also increased (Vihma et al., 2009). Clouds may be associated with storm events, which may trigger breakout events as well as contribute to pre-conditioning by producing fractures via wind-generated wave interactions with the landfast ice (Kohout et al., 2014). Similarly, precipitation of all

types is positively correlated with the binary breakout event variable at these short lead times, which may also be associated with stormy weather.

At intermediate lead times ranging from 7 to 18 days, the only significant environmental variables are related to precipitation. Rainfall predictors are positively correlated with the binary breakout event variable, likely because rainfall enhances melt through the addition of latent heat and by decreasing the surface albedo (Bintanja, 2018). Rainfall is often associated with air masses that have migrated north from lower, warmer, latitudes (Bintanja, 2018). The heat held in the rainwater can transfer to the sea ice, enhancing melting even more (Bintanja, 2018). Snowfall at 13-, 14- and 16-day lead times has a positive correlation with the binary breakout event variable, which is counterintuitive because of the inhibitory effect of snowfall on ice cover melt (Bintanja, 2018; Wadhams, 2000). Snowfall with positive correlations with the binary breakout event variable can't be explained physically, and these snowfall variables don't have any colinear environmental variables. For this reason, the correlation is likely spurious, a product of most of the data points in these variables being equal to zero (i.e., no snowfall).

At long leads and averages greater than 18 days, precipitation is significant at 19 to 20-day leads, and radiation at the surface is significant at all leads. Variables relating to snowfall and non-specific precipitation at leads of 19 and 20 days are all negatively correlated with the binary breakout event variable. At these long lead times, precipitation is likely to fall as snow because more than half a month ahead of a breakout event it is likely cold enough for precipitation to fall to the ground as snow and have an insulating effect on the ice cover, inhibiting melt. During the melt season, snow layers can insulate the ice from warm air, inhibiting the exchange of heat (Bintanja, 2018; Wadhams, 2000).

Additionally, fresh snow increases albedo, inhibiting absorption of solar radiation. Reduced exchange of heat and absorption of radiation inhibits thermal decay of landfast ice, making it less likely to breakup (Perovich & Polashenski, 2012; Wadhams, 2000). At these long lead times, downwelling long-wave radiation was negatively correlated with the binary breakout event variable at 19- and 20-day leads, and solar radiation was positively correlated with it at 19 to 21-day leads. This represents a lack of cloud cover, and the absence of cloud cover precludes fresh snowfall, which would insulate the ice cover, as described above (Bintanja, 2018; Wadhams, 2000).

No non-radiative flux variables are mentioned in any of the lead intervals above. This is because many their relationships to the binary breakout event variable are not easy to interpret (*forecast logarithm of surface roughness for heat and mean vertically integrated moisture divergence*) and none follow the same patterns as the other three categories. The evaporation of snow (sublimation) is positively correlated with the binary breakout event variable on the day of a breakout event, which makes sense because sublimation is related to greater surface latent heat flux, and considerably impacts snow depth on sea ice covers (Fichefet & Morales Maqueda, 1999). Inversely, the evaporation potential is negatively correlated with the binary breakout event variable. Low evaporation potential might be associated with an increased dew point temperature, due to the near-surface atmosphere becoming more humid (Burn & Hesch, 2006). The near-surface atmosphere can become more humid because of rainfall, and low clouds or fog.

*Instantaneous surface sensible heat flux* has a negative correlation with the binary breakout event variable (positive fluxes are downward). This means that decreased transfer of heat from the air to the surface correlates with breakout events, which is

counterintuitive. The magnitude of this parameter is related to the temperature gradient between the surface and the near-surface atmosphere (ECMWF, 2021). The negative correlation with sensible heat flux could be the result of relatively warm surface temperatures, which would reduce the temperature gradient with the near-surface atmosphere. This means that the temperature of the ice cover is close to the temperature of the atmosphere, relatively warm.

### 5.3 Logistic regression

At least one of the seven predictors implemented in the long-leads benchmark logistic regression model belong to three of the four environmental variable categories (mechanical, precipitation, radiation balance), excluding non-radiative fluxes. Two of these predictors are related to precipitation, and two are related to radiation balance. The linear relationship between the logit of the model's outcome and the precipitation predictors is interesting because it ranges between two categories, which are no precipitation and precipitation. All the predictors have approximately equal model coefficient z-scores [0.22-0.26] for the parameters in the z-score fitted models, which indicates that they are all contributing roughly equally to producing the model output. In the short-leads benchmark model, there is a greater difference between the predictors' z-score coefficients. The greatest coefficient [-0.30] belongs to *mean surface direct short-wave radiation flux* as a 3-day average, followed by the wind predictors [-0.25]. The lowest coefficient [-0.18] belongs to the *total column rain water* predictor. Petrich et al.

(2012) also identified a strong correlation with downwelling solar radiation for the purpose of predicting thermal breakup.

Another interesting outcome is that none of the predictors are significant on the day of a breakout event, they are all derived from different leads and averages ahead of breakout events, the shortest of which are 3-day leads. This suggests that breakout events are not spontaneous events but require preconditioning in the days leading up to a breakout event. For example, winds may not necessarily contribute to a breakout event occurring on a given day, but rather winds over the days leading up to a breakout event may move the ice into a position that is vulnerable to breakout.

The long-leads benchmark model had the highest symmetric extremal dependence index (SEDI) and receiver operating characteristic (ROC) of all the individual models generated. However, the shrinkage of the benchmark model's SEDI [0.27], based on the average cross-validation schemes suggests that it does not perform better than the climatology model [SEDI = 0.28]. The climatology model was not cross validated, so there is likely shrinkage in the climatology model that has not been accounted for.

Additionally, the climatology model, as constructed, represents only a stationary process, making it inappropriate for use in non-stationary problems like the changes to sea ice phenology observed in this thesis. The ensemble model is the only model that performs marginally better than the climatology model [SEDI = 0.29-0.30]. Although the SEDI is comparable, the hit rate is much higher for the ensemble model [0.61] than the climatology model [0.50]. In the climatology model, the number of hits is equal to the number of misses, which makes it less attractive to implement operationally than the ensemble model. Although the skill is poor, the long-leads model has a greater ability to

distinguish signal from noise [ROC = 0.67] than the climatology model [ROC = 0.58], which is much closer to the signal detection of a coin flip [ROC = 0.5].

None of the models are skillful enough to consider implementing operationally. The SEDI is lower than other predictive models, including a numerical weather prediction (NWP) precipitation model, which had an SEDI = 0.55-0.87 (North et al., 2013).

However, the SEDI score is comparable to predictive models of cloud fraction, which had SEDIs as low as 0.33 (Gregow et al., 2020). Although the SEDI is relatively low, the ROC of the long-leads benchmark logistic regression model [ROC = 0.67] is better than the ROC of 1-month probabilistic forecasts of surface temperature [ROC = ~0.64] and precipitation [ROC = ~0.55] in the Northern Hemisphere from the Japan Meteorological Agency, although it is worse than the forecast for sea surface temperature [ROC = ~0.75] (JMA, 2002).

Better model performance was observed in exploratory models (not shown) that were more permissive with respect to the environmental variable that were included.

Essentially, more saturated models with more environmental variables had improved model skill. However, the precise physical relationship between these environmental variables and the binary breakout event was unclear. Including more information successfully obtained correct predictions, even though these correct predictions may well have been obtained for the wrong reasons. The effect of increasing the number of parameters in the model is also exemplified by the greater skill of the ensemble model, which included three times as many parameters as the long-leads benchmark model albeit across seven component models. The ensemble approach allowed for a greater number of

parameters in the model, while ensuring parsimony within the individual component models.

There are many ways to increase model parameters through ensemble modelling. An alternative ensemble scheme to what was implemented in this thesis is a bagged ensemble. In this scheme, several base models are trained in parallel and then aggregated to construct a randomized generalized linear model (Song et al., 2013). Unlike a conventional bootstrap, which would subsample the complete dataset, this bootstrap would also subsample random combinations of the environmental predictors implemented in the benchmark model (Song et al., 2013). By taking subsets of the environmental predictors used in the benchmark model, the base models are artificially destabilized by increasing the variance across them to increase the range of possible outcomes (Breiman, 1996; Song et al., 2013). Applying this method may enhance model skill by way of increased parameterization.

Another way to introduce alternative model parameters, without affecting model parsimony, would be to add cumulative derived environmental variables to the candidate predictor pool. Petrich et al. (2012) used 2-month cumulative shortwave irradiance as a proxy for ice decay in their ice breakup model. This approach may identify similar relationships between breakout and cumulative derivatives of other environmental variables that are relevant to the Admiralty Inlet case. In general, it is difficult to predict an event that may have several underlying causes. In the case of breakout events this is particularly true since breakout can occur as early as April and as late as July. We can expect the triggers to differ significantly with respect to mechanical and thermal processes between these two timings. Accumulated degree-days of melt (ADDM) was

investigated in both this study and by Petrich et al. (2012), and in neither instance was it found to be significant. Interaction terms should be explored to investigate possible relationships exhaustively. Short-range cumulative variables and changes in the variables might be fruitful, as well as cumulative variables that extend through the winter that account for ice strength and competency during freeze-up. Since an average of 10 breakout events now occur during the spring, a breakout event occurs approximately every 12 days in April through July (122 days). This suggests that another breakout event will likely occur between the long leads and averages (>12 days) of preconditioning environmental variables and the breakout event that they relate to. This shouldn't be an issue, since preconditioning, particularly related to energy balance, can impact the entire ice cover, not just the ice that is on the verge of breakout, and mechanical predictors like winds are only significant at shorter leads of 6 days or less. Alternative, possibly better predictors could also be identified by exploring interaction terms.

#### **5.4 Approaches to ice breakout modelling and future directions**

In this thesis, an empirical modelling approach was implemented with a relaxed threshold ( $p < 0.1$ ) for inclusion of environmental variables, selected from all possible variables available. This inductive approach was favored over a deductive approach, where environmental variables are selected based on their expected, or assumed, relationship to breakout events. Since this is an exploratory investigation of breakout events, and there is little pre-existing literature to guide variable selection, the approach used here allowed all possible candidate predictors to be considered. Interestingly, the environmental variables

selected in the final logistic regression models, using point-biserial correlation and  $\chi^2$  significance, are examples of variables that might have been selected using prior knowledge of the process of ice breakout. For example, wind was reported as being an important variable by community members (Bell et al., 2019; Ford et al., 2006). Additionally, downwelling radiation and precipitation play an important role in enhancing or inhibiting melt (Bintanja, 2018; Petrich et al., 2012; Wadhams, 2000). Despite the different approach, a similar result was achieved while allowing for the exploration of unexpected variables. Additionally, investigation using numerical modelling has already been conducted by Loewen (2020), yielding distinct but significant results for the study of breakout events.

Regardless of the modelling approach used, any model will be limited by the data used to construct it. The greatest challenge in this thesis was the availability of accurate data that is representative of conditions at the northern floe edge in Admiralty Inlet. The available satellite imagery could only resolve the timing of breakout events to the day of the event, which makes it difficult to correlate these events with environmental variables like tides and currents, which have semi-diurnal oscillations. This could be ameliorated in the future by community-led *in situ* observations of breakout events. Community observers living near lakes in Maine, New Brunswick and New Hampshire have recorded the date of ice out on their respective lakes as far back as the early 1800s (Patterson & Swindles, 2014), and in recent years, due to the prevalence of community discussion via social media, ice out is reported down to the hour. If the community of Ikpiarjuk, and other Arctic communities, produced a similar record of observed breakout events, a record far superior to the one produced using satellite imagery in this thesis could be produced over

the next couple decades. Logistically, this is more challenging than collecting ice out data for lakes, where community members can simply look out their window to see if the ice has cleared out of the lake. Deploying a series of onshore time-lapse cameras at strategic locations along Admiralty Inlet could make the collection of this data easier (Loewen, 2019, 2020). Additionally, the launch of the RADARSAT Constellation Mission in 2019 now provides imaging of the Arctic up to four times each day (GC-CSA, 2019). This frequency of images will contribute significantly to improving observations of breakout events in the inlet.

The environmental variables used in this thesis are also not ideal for use in predictive modelling because they are generated by a reanalysis model, rather than from *in situ* observations. A lack of observations in the Arctic limits the accuracy of reanalysis data for modelling local processes (Graham et al., 2019). Additionally, sudden events, like breakout events are triggered by stochastic processes at scale that may not be represented by ERA5 or WebTide very well. There is a weather station located at the Arctic Bay airport, however this is located up to 80 km from the floe edge, where the inlet meets Lancaster Sound, and the local topography would modify environmental conditions. Data from the Arctic Bay airport were compared to data collected at the floe edge in 2019 by Loewen (2020), and there was poor agreement between the observations. Deploying seasonal on-ice weather stations would produce the most accurate data for the floe edge conditions, however a permanent onshore weather station closer to the floe edge would be a significant improvement. Based on the results of this thesis, a weather station should minimally be equipped with anemometers, short- and long-wave radiation sensors, and precipitation sensors, but more variables are better because subsequent analyses might

reveal unexpected relationships between those variables and breakout events. There are also spatial and interannual variability in ice properties to contend with, making predicting an event at a specific moment in time based on short- or long-term changes in energy balance challenging. Data collection regarding the condition of the ice cover itself could be beneficial. Ice variables like thickness, snow depth and ice temperature profiles could help to describe the competence of the ice cover. *In situ* current and tide monitors would also be an improvement over the modelled data available for this work. A data series two decades in length, complemented by an improved resolution of observations of breakout events described above, could be used to produce a much more robust model than what could be generated in this thesis.

In addition to improved data sets, alternative modelling methods should be explored. Empirical modelling techniques are constantly advancing, and there are many alternative modelling methods to the logistic regression method selected for this thesis. To predict river ice jam breakup in the Hay River, NWT, Zhao et al. (2012) developed and assessed a three-layer artificial neural network (ANN). An ANN is a complex, non-linear relationship between input variables that are easily collected or readily available (Zhao et al., 2012). The ANN model was able to effectively generalize complex relationships for river ice breakup forecasting and performed much better than standard multiple linear regression methods models (Zhao et al., 2012). ANN is just one of many alternative modeling techniques currently used across many fields of study. Over the coming years, these techniques will improve significantly and by implementing these techniques, in conjunction with the rigorous data collection campaign suggested above, forecast skill for breakout events will significantly improve. In fact, different modelling algorithms could

also be aggregated in an ensemble, which would increase the number of valid parameters that a model can include.

If improvements are made to the available data and modelling methods, and predictive skill is operationally feasible, the way that these products are delivered to community members is an important factor to consider. The Enfotec (2003) describes differences in the responses of the communities of Ikpiarjuk and Pond Inlet to the warnings of elevated risk of breakout delivered to the communities. Essentially, certain demographics within and between communities are more risk averse than others. Tools provided to the community should help to address these issues by targeting their use towards community members that take greater risks. Risk averse community members will likely not go to the floe edge when there is any risk of breakout. Issues like these need to be addressed through community consultation, but an important question that should be brought to community members is what form warnings should be provided in.

In this thesis, the outcome of the logistic regression models is binary to match the validation dataset, where a breakout event either occurred or did not occur. This binary outcome was converted from a continuous probability, which might be more easily interpreted in an alternative framework to the current binary one. An alternative worth considering is to classify risk categories (i.e., High, Moderate and Low risk). These categories will need to be defined based on the outcomes of the modelling approach. For example, the ratio of the hit rate to the false alarm rate is used in Table 5.1 to discriminate between outcomes of the long-leads benchmark model. Due to the relatively low skill of the model, the results of the classification in this example are not ideal because there are more breakout events classified into the low-risk category than the high-risk category, but

they do illustrate the concept well. Low risk is defined as outcomes with probabilities less than 0.16, below this decision threshold the ratio of the hit rate to the false alarm is 1.5 or lower. Moderate risk includes outcomes with probabilities between 0.12 and 0.21, in which the ratio of the hit rate to the false alarm rate is between 1.5 and 2.5. Outcomes with probabilities greater than or equal to 0.21 are classified as high risk.

**Table 5.1 Probability partition scheme for the benchmark logistic regression model.**

Risk Category	Probability Decision threshold	Breakout Events	H/F
High	$\geq 0.21$	31	$>2.5$
Moderate	$0.12 - <0.21$	55	$1.5 - 2.5$
Low	$<0.12$	36	$<1.5$

While this makes the results of a modelling technique more realistic representations of the outcome, it does have one significant shortcoming, which is that this classification cannot be validated. Ordinal classifications for other predictive models, like precipitation, can be validated because the distinction between the classes is based on physical properties. For example, an ordinal classification of precipitation might include classes like no rain, light rain, and heavy rain (Haiden et al., 2012), which are based on the amount of precipitation that falls. Predictions for these categories can be validated by comparing to real measures of precipitation. Since risk categories are not physical properties of breakout events, the ordinal classification cannot be validated.

## Chapter 6: Conclusion

Landfast sea ice in the Arctic is an important winter highway for people living in the north (Cooley et al., 2020; Ford et al., 2006; Nickels et al., 2005). Due to widespread observations of declining sea ice extent, thickness, and duration, it is uncertain how travel on landfast sea ice will be affected in the future (Comiso et al., 2017; Galley et al., 2012; Howell et al., 2016; Perovich et al., 2020). Communities have noticed worsening stability and predictability of the floe edge (Cooley et al., 2020; Ford et al., 2006; Nickels et al., 2005), which is not parameterized in sea ice models and has not been investigated in sea ice datasets (Lemieux et al., 2016). The goal of this thesis is to add to the existing Inuit Qaujimagatuqangit surrounding breakout events and to explore whether a predictive model might be skillful enough for operational use.

This is the first work that has investigated the climatology of floe edge deterioration over two decades, and significant changes were observed over the 21-year study period. First breakout events occurred an average of 46 days earlier per decade, and complete breakup of the landfast sea ice cover in the inlet occurs an average of approximately 9 days earlier over the 21-year period. Additionally, the average number of breakout events occurring each year has increased by five per year over the same period. This is supported by reports from the community of Ikpiarjuk that the landfast ice is becoming more hazardous for travel and cultural practices during the spring season (Bell et al., 2019; Ford et al., 2006). The same approach used in this work could be applied to other communities such as Pond Inlet to understand if the changes observed in Admiralty Inlet

are occurring in other places, and if the changes to the stability of landfast sea ice are Arctic-wide.

Our understanding of the timing and mechanisms of landfast sea ice breakout events at the northern floe edge in Admiralty Inlet was improved by analysis of relational statistics between past breakout events and readily available reanalysis data. These new insights complement existing Inuit Qaujimajatuqangit and add additional important considerations for ice users in Admiralty Inlet. For example, both community members and previous researchers in the inlet reported that spring tides coincide with higher risk of breakout events (Bell et al., 2019; Enfotec Technical Services, 2003). However, based on the absence of correlation between maximum daily tide elevation and breakout events between 2000 and 2020, the risk of breakout events is not significantly different during neap tides, so ice users should still be cautious when travelling to the northern floe edge, regardless of the time in the lunar cycle. It is worth pointing out that Inuit Qaujimajatuqangit draws on observations extending back much further than this study.

Community members also reported that strong winds and changes in wind direction contribute to breakout events (Bell et al., 2019; Ford et al., 2006), which was also found in this thesis. Northward winds are correlated with breakout events, understandably because they might push ice floes into Lancaster Sound to the north. Eastward and westward winds are also correlated with breakout events, which may contribute to shifting ice floes to either unground them from the shore or to position them more favorably for breakout. Some new relationships that were identified are the positive correlations with rainfall and the negative correlations with snowfall. Rainfall might contribute to increased risk of breakout through the addition of latent heat, enhancing

melt (Bintanja, 2018), while snowfall could inhibit melt by insulating the ice cover (Bintanja, 2018; Wadhams, 2000), reducing the risk of breakout events.

Although promising relationships were identified, the logistic regression models had relatively low skill [ $SEDI_{best} = 0.29-0.30$ ;  $ROC_{best} = 0.67$ ] in predicting sea ice breakout events at the northern floe edge of Admiralty Inlet. The low skill could be attributed in part to the poor representativeness of the data implemented in the model, and it is surprising that the skill of the model is as high as it is despite this major limitation.

Despite the poor data, increasing the number of parameters included in a model through ensemble modelling helped to increase predictive skill. In this work, the method for increasing parameters was a custom weighted summation in an ensemble of models, but future exploration of logistic regression for this application should explore the randomized generalized linear model approach of Song et al. (2013), and other potential approaches. There should also be an exploration of other modelling approaches beyond logistic regression, possibly artificial neural networks, which were used effectively by Zhao et al. (2012) to predict river ice jam breakup in the Hay River, Northwest Territories. Additionally, Petrich et al. (2012) investigated cumulative radiance as measures of the state of ice decay and were able to predict thermal decay as a two-week forecast to within two days. In addition to the derived leads and averages, cumulative derivatives should be investigated.

The skill of any future model can only marginally improve with modifications to the modelling approach, but improvements to the data sets implemented in the model might help to increase predictive skill even more. To this end, a long term, comprehensive, data-collection campaign at the northern floe edge of Admiralty inlet could significantly

improve the quality of available data. The lack of *in situ* data in the Arctic is already a large weakness in the accuracy and representativeness of reanalysis data (Graham et al., 2019). Implementation of *in situ* data would preclude the need for reanalysis data and would be the most representative information of the meteorological and oceanographic conditions near the floe edge. Improved data collection should include monitoring of the spring floe-edge to improve the resolution of observed breakout events to one to six hours. Improved resolution of observations could be achieved through the deployment of on-shore time-lapse cameras (Loewen, 2019, 2020) or by analyzing images from the recently launched RADARSAT Constellation Mission, which provides images of the Arctic up to four times per day (GC-CSA, 2019). It should also include collection of *in situ* meteorological conditions, including radiation balance, precipitation, and wind, as well as ice conditions like thickness, temperature and depth of snow cover, and oceanographic conditions like water temperature and current and tide parameters.

Ideally, this data collection should be community-based to ensure that the campaign can be maintained long-term by increasing community-members' engagement with the project and so that in the future community members can implement hazard-related operations independently from researchers. Additionally, there should be more consultation with the community to understand the form in which predictive products should be provided to maximize uptake of these products, particularly for the less risk-averse members of the community. There were originally plans for more consultation with the community as part of this thesis, however this was hampered by the outbreak of the COVID-19 virus.

## References

- Afyouni, S., Smith, S. M., & Nichols, T. E. (2019). Effective degrees of freedom of the Pearson's correlation coefficient under autocorrelation. *NeuroImage*, *199*, 609–625. <https://doi.org/10.1016/j.neuroimage.2019.05.011>
- Barry, R. G., Moritz, R. E., & Rogers, J. C. (1979). The fast ice regimes of the Beaufort and Chukchi sea coasts, Alaska. *Cold Regions Science and Technology*, *1*, 129–152.
- Bell, T., Arreak, A., & Mosesie, J. (2019). Inuit Qaujimaqatuqangit of landfast ice breakup in Admiralty Inlet. *SmartICE*.
- Bintanja, R. (2018). The impact of Arctic warming on increased rainfall. *Scientific Reports*, *8*(1). <https://doi.org/10.1038/s41598-018-34450-3>
- Breiman, L. (1996). Heuristics of instability and stabilization in model selection. *The Annals of Statistics*, *24*(6), 2350–2383.
- Burn, D. H., & Hesch, N. M. (2006). A Comparison of trends in potential and pan evaporation for the Canadian prairies. *Canadian Water Resources Journal*, *31*(3), 173–184. <https://doi.org/10.4296/cwrj3103173>
- CIS-ECCC. (2006). Canadian Ice Service Digital Archive - Regional Charts: History, Accuracy and Caveats. *Environment and Climate Change Canada*.
- Collins, A. K., Hannah, C. G., & Greenberg, D. (2011). Validation of a high resolution modelling system for tides in the Canadian Arctic Archipelago. *Ocean Sciences Division, Maritimes Region, Fisheries and Oceans Canada*.
- Comiso, J. C., Meier, W. N., & Gersten, R. (2017). Variability and trends in the Arctic Sea ice cover: Results from different techniques. *Journal of Geophysical Research: Oceans*, *122*(8), 6883–6900. <https://doi.org/10.1002/2017JC012768>

- Cooley, S. W., Ryan, J. C., Smith, L. C., Horvat, C., Pearson, B., Dale, B., & Lynch, A. H. (2020). Coldest Canadian Arctic communities face greatest reductions in shorefast sea ice. *Nature Climate Change*, *10*(6), 533–538.  
<https://doi.org/10.1038/s41558-020-0757-5>
- Crocker, G. B., & Wadhams, P. (1989). Breakup of Antarctic fast ice. *Cold Regions Science and Technology*, *17*, 61–76.
- Dai, A., Luo, D., Song, M., & Liu, J. (2019). Arctic amplification is caused by sea-ice loss under increasing CO<sub>2</sub>. *Nature Communications*, *10*(1).  
<https://doi.org/10.1038/s41467-018-07954-9>
- DelSole, T., Trenary, L., & Tippett, M. K. (2017). The weighted-average lagged ensemble. *Journal of Advances in Modeling Earth Systems*, *9*(7), 2739–2752.  
<https://doi.org/10.1002/2017MS001128>
- ECMWF. (2021). Part IV: Physical processes. In *IFS Documentation CY47R3*. Shinfield Park, Reading, England: European Centre for Medium-Range Weather Forecasts.
- Else, B. G. T., Papakyriakou, T. N., Raddatz, R., Galley, R. J., Mundy, C. J., Barber, D. G., Swystun, K., & Rysgaard, S. (2014). Surface energy budget of landfast sea ice during the transitions from winter to snowmelt and melt pond onset: The importance of net longwave radiation and cyclone forcings. *Journal of Geophysical Research: Oceans*, *119*(6), 3679–3693. <https://doi.org/10.1002/2013JC009672>
- Enfotec Technical Services. (2003). *Consultations and Product Evaluations - Final Report*. Montreal, QC, Canada: Enfotec Technical Services Inc.

- Fichefet, T., & Morales Maqueda, M. A. (1999). Modelling the influence of snow accumulation and snow-ice formation on the seasonal cycle of the Antarctic sea-ice cover. *Climate Dynamics*, *15*, 251–268.
- Ford, J. D., Clark, D., Pearce, T., Berrang-Ford, L., Copland, L., Dawson, J., New, M., & Harper, S. L. (2019). Changing access to ice, land and water in Arctic communities. *Nature Climate Change*, *9*(4), 335–339. <https://doi.org/10.1038/s41558-019-0435-7>
- Ford, J. D., Smit, B., & Wandel, J. (2006). Vulnerability to climate change in the Arctic: A case study from Arctic Bay, Canada. *Global Environmental Change*, *16*(2), 145–160. <https://doi.org/10.1016/j.gloenvcha.2005.11.007>
- Fox, J. (2020). *Car package*. RDocumentation. <https://rdocumentation.org/packages/car/versions/3.0-10>
- Galley, R. J., Else, B. G. T., Howell, S. E. L., Lukovich, J. v, & Barber, D. G. (2012). Landfast sea ice conditions in the Canadian Arctic: 1983-2009. *Source: Arctic*, *65*(2), 133–144.
- GC-BIO. (2015). *WebTide Arctic Data (v0.7)*. Bedford Institute of Oceanography. <https://www.bio.gc.ca/science/research-recherche/ocean/webtide/arctic-arctique-en.php>
- GC-CSA. (2019). *What is RCM?* Government of Canada - Canadian Space Agency. <https://www.asc-csa.gc.ca/eng/satellites/radarsat/what-is-rcm.asp>
- GC-CSA. (2021). *RADARSAT: Technical features*. Government of Canada - Canadian Space Agency. <https://www.asc-csa.gc.ca/eng/satellites/radarsat/technical-features/radarsat-comparison.asp>

- Graham, R. M., Cohen, L., Ritzhaupt, N., Segger, B., Graversen, R. G., Rinke, A., Walden, V. P., Granskog, M. A., & Hudson, S. R. (2019). Evaluation of six atmospheric reanalyses over Arctic sea ice from winter to early summer. *Journal of Climate*, 32(14), 4121–4143. <https://doi.org/10.1175/JCLI-D-18-0643.1>
- Gregow, E., Lindfors, A. v., van der Veen, S. H., Schoenach, D., de Haan, S., & Lindsog, M. (2020). The use of satellite and surface observations for initializing clouds in the HARMONIE NWP model. *Meteorological Applications*, 27(6). <https://doi.org/10.1002/met.1965>
- Haiden, T., Rodwell, M. J., Richardson, D. S., Okagaki, A., Robinson, T., & Hewson, T. (2012). Intercomparison of global model precipitation forecast skill in 2010/11 using the SEEPS score. *Monthly Weather Review; Washington*, 140(8), 2720–2733.
- Hall, D. K., Riggs, G. A., & Salomonson, V. v. (2001). *Algorithm theoretical basis document (ATBD): for the MODIS snow and sea ice-mapping algorithms*. MODIS and VIIRS Snow and Ice Global Mapping Project. <https://modis-snow-ice.gsfc.nasa.gov/?c=atbd>
- Hersbach, H., Bell, B., Berrisford, P., Biavati, G., Horányi, A., Muñoz Sabater, J., Nicolas, J., Peubey, C., Radu, R., Rozum, I., Schepers, D., Simmons, A., Soci, C., Dee, D., & Thépaut, J.-N. (2018). ERA5 hourly data on single levels from 1979 to present. *Copernicus Climate Change Service (C3S) Climate Data Store (CDS)*.
- Hogan, R. J., & Mason, I. B. (2011). Deterministic forecasts of binary events. In I. T. Jolliffe & D. B. Stephenson (Eds.), *Forecast verification: A practitioner's guide in atmospheric science* (2nd ed.). John Wiley & Sons, Inc.

- Hosmer, D. W., Lemeshow, Stanley., & Sturdivant, R. X. (2013). *Applied Logistic Regression* (D. J. Balding, N. A. C. Cressie, G. M. Fitzmaurice, H. Goldstein, I. M. Johnstone, G. Molenberghs, D. W. Scott, A. F. M. Smith, R. S. Tsay, & S. Weisberg, Eds.; 3rd ed.). John Wiley & Sons.
- Howell, S. E. L., Laliberté, F., Kwok, R., Derksen, C., & King, J. (2016). Landfast ice thickness in the Canadian Arctic Archipelago from observations and models. *The Cryosphere*, *10*(4), 1463–1475. <https://doi.org/10.5194/tc-10-1463-2016>
- Iba, K., Shinozaki, T., Maruo, K., & Noma, H. (2021). Re-evaluation of the comparative effectiveness of bootstrap-based optimism correction methods in the development of multivariable clinical prediction models. *BMC Medical Research Methodology*, *21*(1). <https://doi.org/10.1186/s12874-020-01201-w>
- IPCC. (2019). *The Ocean and Cryosphere in a Changing Climate - A Special Report of the Intergovernmental Panel on Climate Change* (H.-O. Pörtner, D. C. Roberts, V. Masson-Delmotte, P. Zhai, M. Tignor, E. Poloczanska, K. Mintenbeck, A. Alegria, M. Nicolai, A. Okem, J. Petzold, B. Rama, & N. M. Weyer, Eds.). Intergovernmental Panel on Climate Change.
- Itkin, P., Spreen, G., Cheng, B., Doble, M., Girard-Ardhuin, F., Haapala, J., Hughes, N., Kaleschke, L., Nicolaus, M., & Wilkinson, J. (2017). Thin ice and storms: Sea ice deformation from buoy arrays deployed during N-ICE2015. *Journal of Geophysical Research: Oceans*, *122*(6), 4661–4674. <https://doi.org/10.1002/2016JC012403>
- Jakobsson, M., Mayer, L., Coakley, B., Dowdeswell, J. A., Forbes, S., Fridman, B., Hodnesdal, H., Noormets, R., Pedersen, R., Rebesco, M., Schenke, H. W., Zarayskaya, Y., Accettella, D., Armstrong, A., Anderson, R. M., Bienhoff, P.,

- Camerlenghi, A., Church, I., Edwards, M., ... Weatherall, P. (2012). The International Bathymetric Chart of the Arctic Ocean (IBCAO) Version 3.0. *Geophysical Research Letters*, 39(12). <https://doi.org/10.1029/2012GL052219>
- JMA. (2002). *Verification of probabilistic forecast (leadtime 1-month)*. Japan Meteorological Agency. [https://ds.data.jma.go.jp/tcc/tcc/products/model/probfcst/3-mon/hind/html/skill\\_reg\\_3-mon.html](https://ds.data.jma.go.jp/tcc/tcc/products/model/probfcst/3-mon/hind/html/skill_reg_3-mon.html)
- Jones, J., Eicken, H., Mahoney, A., MV, R., Kambhamettu, C., Fukamachi, Y., Ohshima, K. I., & George, J. C. (2016). Landfast sea ice breakouts: Stabilizing ice features, oceanic and atmospheric forcing at Barrow, Alaska. *Continental Shelf Research*, 126, 50–63. <https://doi.org/10.1016/j.csr.2016.07.015>
- Kabacoff, R. (2011). *R in action: data analysis and graphics with R*. Shelter Island, NY: Manning Publications Co.
- Koen, H. (2020). *ecmwfr*. RDocumentation. <https://rdocumentation.org/packages/ecmwfr/versions/1.3.0>
- Kohout, A. L., Williams, M. J. M., Dean, S. M., & Meylan, M. H. (2014). Storm-induced sea-ice breakup and the implications for ice extent. *Nature*, 509, 604–607. <https://doi.org/10.1038/nature13262>
- Learns, J. R. (2016, September 19). Arctic search-and-rescue missions double as climate warms. *National Geographic*.
- Lemieux, J. F., Dupont, F., Blain, P., Roy, F., Smith, G. C., & Flato, G. M. (2016). Improving the simulation of landfast ice by combining tensile strength and a parameterization for grounded ridges. *Journal of Geophysical Research: Oceans*, 121(10), 7354–7368. <https://doi.org/10.1002/2016JC012006>

- Loewen, A. (2019). *Admiralty Inlet sea ice break-up timelapse 1*. YouTube.  
<https://www.youtube.com/watch?v=YcWtCmWllg>
- Loewen, A. (2020). *Landfast Sea Ice Break-up Processes in Admiralty Inlet, NU*.
- Mahoney, A. R., Eicken, H., Gaylord, A. G., & Gens, R. (2014). Landfast sea ice extent in the Chukchi and Beaufort seas: The annual cycle and decadal variability. *Cold Regions Science and Technology*, *103*, 41–56.  
<https://doi.org/10.1016/j.coldregions.2014.03.003>
- Mahoney, A. R., Eicken, H., & Shapiro, L. (2007). How fast is landfast sea ice? A study of the attachment and detachment of nearshore ice at Barrow, Alaska. *Cold Regions Science and Technology*, *47*(3), 233–255.  
<https://doi.org/10.1016/j.coldregions.2006.09.005>
- Murphy, A. H. (1996). The Finley affair: A signal event in the history of forecast verification. *Weather and Forecasting*, *11*(1), 3–20.
- NASA. (n.d.). *Moderate resolution imaging spectroradiometer*. MODIS. Retrieved November 19, 2021, from <https://modis.gsfc.nasa.gov/>
- Nickels, S., Furgal, C., Buell, M., & Moquin, H. (2005). *Unikkaaqatigiit - Putting the Human Face on Climate Change: Perspectives from Inuit in Canada*. Ottawa: Inuit Tapiriit Kanatami, Nasivvik Centre for Inuit Health and Changing Environments at Université Laval and the Ajunnginiq Centre at the National Aboriginal Health Organization.
- North, R., Trueman, M., Mittermaier, M., & Rodwell, M. J. (2013). An assessment of the SEEPS and SEDI metrics for the verification of 6h forecast precipitation

- accumulations. *Meteorological Applications*, 20(2), 164–175.  
<https://doi.org/10.1002/met.1405>
- NSIDC. (2020). *Remote sensing: Passive microwave*. National Snow & Ice Data Centre.  
[https://nsidc.org/cryosphere/seaice/study/passive\\_remote\\_sensing.html](https://nsidc.org/cryosphere/seaice/study/passive_remote_sensing.html)
- NSIDC. (2021a). *MODIS data: Moderate resolution imaging spectroradiometer*.  
National Snow & Ice Data Center. <https://nsidc.org/data/modis/index.html>
- NSIDC. (2021b). *Polar stereographic data: NSIDC polar stereographic grid information*. National Snow & Ice Data Center. [https://nsidc.org/data/polar-stereo/ps\\_grids.html](https://nsidc.org/data/polar-stereo/ps_grids.html)
- Onstott, R. G., & Shuchman, R. A. (2004). SAR measurements of sea ice. In C. R. Jackson & J. R. Apel (Eds.), *SAR marine user's manual* (pp. 81–115). National Oceanic and Atmospheric Administration.
- Osborne, J. W. (2017). A practical guide to testing assumptions and cleaning data for logistic regression. In *Best Practices in Logistic Regression*. SAGE Publications, Ltd. <https://doi.org/10.4135/9781483399041>
- Ottenbacher, K. J., Ottenbacher, H. R., Tooth, L., & Ostir, G. v. (2004). A review of two journals found that articles using multivariable logistic regression frequently did not report commonly recommended assumptions. *Journal of Clinical Epidemiology*, 57(11), 1147–1152. <https://doi.org/10.1016/j.jclinepi.2003.05.003>
- Patterson, R. T., & Swindles, G. T. (2014). Influence of ocean–atmospheric oscillations on lake ice phenology in eastern North America. *Climate Dynamics*, 45(9–10), 2293–2308. <https://doi.org/10.1007/s00382-014-2415-y>

- Pedersen, L. T., Tonboe, R., Kern, S., Lavergne, T., Ivanova, N., & Heygster, G. (2017). Sea ice observations. In T. Carrieres, M. Buehner, J.-F. Lemieux, & L. T. Pedersen (Eds.), *Sea ice analysis and forecasting: Towards and increased reliance on automated prediction systems*. Cambridge University Press.
- Perovich, D., Meier, W., Tschudi, M., Farrell, S., Hendricks, S., Gerland, S., Haas, C., Krumpen, T., Polashenski, C., Ricker, R., & Webster, M. (2018). Sea Ice. In *NOAA Arctic Report Card 2018* (pp. 25–32). National Oceanic and Atmospheric Administration. <https://www.arctic.noaa.gov/Report-Card>
- Perovich, D., Meier, W., Tschudi, M., Hendricks, S., Petty, A. A., Divine, D., Farrell, S., Gerland, S., Haas, C., Kaleschke, L., Pavlova, O., Ricker, R., Tian-Kunze, X., Webster, M., & Wood, K. (2020). Sea ice. In R. L. Thoman, J. Richter-Menge, & M. L. Druckenmiller (Eds.), *NOAA Arctic Report Card 2020* (pp. 44–53). <https://doi.org/10.25923/n170-9h57>
- Perovich, D., & Polashenski, C. (2012). Albedo evolution of seasonal Arctic sea ice. *Geophysical Research Letters*, 39(8). <https://doi.org/10.1029/2012GL051432>
- Petrich, C., Eicken, H., Zhang, J., Krieger, J., Fukamachi, Y., & Ohshima, K. I. (2012). Coastal landfast sea ice decay and breakup in northern Alaska: Key processes and seasonal prediction. *Journal of Geophysical Research: Oceans*, 117(2). <https://doi.org/10.1029/2011JC007339>
- R-core. (1969). *stats*. RDocumentation. <https://rdocumentation.org/packages/stats/versions/3.6.2>
- Rizopoulos, D. (2018). *ltm*. RDocumentation. <https://rdocumentation.org/packages/ltm/versions/1.1-1>

- Selyuzhenok, V., Krumpen, T., Mahoney, A., Janout, M., & Gerdes, R. (2015). Seasonal and interannual variability of fast ice extent in the southeastern Laptev Sea between 1999 and 2013. *Journal of Geophysical Research: Oceans*, *120*(12), 7791–7806. <https://doi.org/10.1002/2015JC011135>
- Serreze, M. C., & Barry, R. G. (2011). Processes and impacts of Arctic amplification: A research synthesis. *Global and Planetary Change*, *77*(1–2), 85–96. <https://doi.org/10.1016/j.gloplacha.2011.03.004>
- Sheskin, D. J. (2011). *Handbook of parametric and nonparametric statistical procedures* (5th ed.). Chapman & Hall / CRC.
- Shokr, M., & Sinha, N. (2015). Remote sensing principles relevant to sea ice. In *Sea ice: Physics and remote sensing* (pp. 271–336).
- Song, L., Langfelder, P., & Horvath, S. (2013). Random generalized linear model: a highly accurate and interpretable ensemble predictor. *BMC Bioinformatics*, *14*, 5. <http://www.biomedcentral.com/1471-2105/14/5>
- Stoltzfus, J. C. (2011). Logistic regression: A brief primer. *Academic Emergency Medicine*, *18*(10), 1099–1104. <https://doi.org/10.1111/j.1553-2712.2011.01185.x>
- Untersteiner, N. (1986). *The Geophysics of sea ice*.
- Vihma, T., Johansson, M. M., & Launiainen, J. (2009). Radiative and turbulent surface heat fluxes over sea ice in the western Weddell Sea in early summer. *Journal of Geophysical Research: Oceans*, *114*(4). <https://doi.org/10.1029/2008JC004995>
- Wadhams, P. (2000). *Ice in the ocean*. Overseas Publishers Association.
- Wilson, K. J., Arreak, A., Itulu, J., Community, S., Committee, M., Ljubicic, G. J., Bell, T., & Ca, K. W. (2021). “When we’re on the ice, all we have is our Inuit

Qaujimajatuqangit”: Mobilizing Inuit knowledge as a sea ice safety adaptation strategy in Mittimatalik, Nunavut. *Arctic*, 74(4), 525–549.

<https://doi.org/10.14430/arctic74212>

Ye, K., & Messori, G. (2021). Inter-model spread in the wintertime Arctic amplification in the CMIP6 models and the important role of internal climate variability. *Global and Planetary Change*, 204. <https://doi.org/10.1016/j.gloplacha.2021.103543>

Yu, K. xia, Zhang, X., Li, P., Li, Z., Qin, Y., & Sun, Q. (2019). Probability prediction of peak break-up water level through vine copulas. *Hydrological Processes*, 33(6), 962–977. <https://doi.org/10.1002/hyp.13377>

Zhao, L., Hicks, F. E., & Fayek, A. R. (2012). Applicability of multilayer feed-forward neural networks to model the onset of river breakup. *Cold Regions Science and Technology*, 70, 32–42. <https://doi.org/10.1016/j.coldregions.2011.08.011>

## Appendices

### Appendix A - ERA5 reanalysis variables

Appendix Table A.1 105 Single level ERA5 reanalysis variables with 0.25-degree spatial resolutions and continuous coverage over Admiralty Inlet, acquired from the Copernicus Climate Data Store (CDS).

Name	Units
<i>100 metre U wind component</i>	$\text{m s}^{-1}$
<i>100 metre V wind component</i>	$\text{m s}^{-1}$
<i>Neutral wind at 10 m u-component</i>	$\text{m s}^{-1}$
<i>10 metre U wind component</i>	$\text{m s}^{-1}$
<i>Neutral wind at 10 m v-component</i>	$\text{m s}^{-1}$
<i>10 metre V wind component</i>	$\text{m s}^{-1}$
<i>10 metre wind gust since previous post-processing</i>	$\text{m s}^{-1}$
<i>2 metre dewpoint temperature</i>	K
<i>2 metre temperature</i>	K
<i>Clear-sky direct solar radiation at surface</i>	$\text{J m}^{-2}$
<i>Convective precipitation</i>	m
<i>Convective rain rate</i>	$\text{kg m}^{-2} \text{s}^{-1}$
<i>Convective snowfall</i>	m of water equivalent
<i>Convective snowfall rate water equivalent</i>	$\text{kg m}^{-2} \text{s}^{-1}$
<i>Downward UV radiation at the surface</i>	$\text{J m}^{-2}$
<i>Evaporation</i>	m of water equivalent
<i>Forecast logarithm of surface roughness for heat</i>	-
<i>Ice temperature layer 1</i>	K
<i>Ice temperature layer 2</i>	K
<i>Ice temperature layer 3</i>	K
<i>Ice temperature layer 4</i>	K
<i>Instantaneous 10 metre wind gust</i>	$\text{m s}^{-1}$
<i>Instantaneous large-scale surface precipitation fraction</i>	-
<i>Instantaneous surface sensible heat flux</i>	$\text{W m}^{-2}$
<i>Large-scale precipitation</i>	m
<i>Large-scale precipitation fraction</i>	s
<i>Large scale rain rate</i>	$\text{kg m}^{-2} \text{s}^{-1}$
<i>Large-scale snowfall</i>	m of water equivalent

Name	Units
<i>Large scale snowfall rate water equivalent</i>	$\text{kg m}^{-2} \text{ s}^{-1}$
<i>Maximum temperature at 2 metres since previous post-processing</i>	K
<i>Maximum total precipitation rate since previous post-processing</i>	$\text{kg m}^{-2} \text{ s}^{-1}$
<i>Mean boundary layer dissipation</i>	$\text{W m}^{-2}$
<i>Mean convective precipitation rate</i>	$\text{kg m}^{-2} \text{ s}^{-1}$
<i>Mean convective snowfall rate</i>	$\text{kg m}^{-2} \text{ s}^{-1}$
<i>Mean eastward gravity wave surface stress</i>	$\text{N m}^{-2}$
<i>Mean eastward turbulent surface stress</i>	$\text{N m}^{-2}$
<i>Mean evaporation rate</i>	$\text{kg m}^{-2} \text{ s}^{-1}$
<i>Mean large-scale precipitation fraction</i>	-
<i>Mean large-scale precipitation rate</i>	$\text{kg m}^{-2} \text{ s}^{-1}$
<i>Mean large-scale snowfall rate</i>	$\text{kg m}^{-2} \text{ s}^{-1}$
<i>Mean northward turbulent surface stress</i>	$\text{N m}^{-2}$
<i>Mean potential evaporation rate</i>	$\text{kg m}^{-2} \text{ s}^{-1}$
<i>Mean sea level pressure</i>	Pa
<i>Mean snow evaporation rate</i>	$\text{kg m}^{-2} \text{ s}^{-1}$
<i>Mean snowfall rate</i>	$\text{kg m}^{-2} \text{ s}^{-1}$
<i>Mean surface direct short-wave radiation flux</i>	$\text{W m}^{-2}$
<i>Mean surface direct short-wave radiation flux, clear sky</i>	$\text{W m}^{-2}$
<i>Mean surface downward long-wave radiation flux</i>	$\text{W m}^{-2}$
<i>Mean surface downward long-wave radiation flux, clear sky</i>	$\text{W m}^{-2}$
<i>Mean surface downward short-wave radiation flux</i>	$\text{W m}^{-2}$
<i>Mean surface downward short-wave radiation flux, clear sky</i>	$\text{W m}^{-2}$
<i>Mean surface downward UV radiation flux</i>	$\text{W m}^{-2}$
<i>Mean surface latent heat flux</i>	$\text{W m}^{-2}$
<i>Mean surface net long-wave radiation flux</i>	$\text{W m}^{-2}$
<i>Mean surface net long-wave radiation, clear sky</i>	$\text{W m}^{-2}$
<i>Mean surface net short-wave radiation flux</i>	$\text{W m}^{-2}$
<i>Mean surface net short-wave radiation flux, clear sky</i>	$\text{W m}^{-2}$
<i>Mean surface sensible heat flux</i>	$\text{W m}^{-2}$
<i>Mean top downward short-wave radiation flux</i>	$\text{W m}^{-2}$
<i>Mean top net long-wave radiation flux</i>	$\text{W m}^{-2}$
<i>Mean top net long-wave radiation flux, clear sky</i>	$\text{W m}^{-2}$
<i>Mean top net short-wave radiation flux</i>	$\text{W m}^{-2}$
<i>Mean top net short-wave radiation flux, clear sky</i>	$\text{W m}^{-2}$

Name	Units
<i>Mean total precipitation rate</i>	$\text{kg m}^{-2} \text{s}^{-1}$
<i>Mean vertically integrated moisture divergence</i>	$\text{kg m}^{-2} \text{s}^{-1}$
<i>Minimum temperature at 2 metres since previous post-processing</i>	K
<i>Minimum total precipitation rate since previous post-processing</i>	$\text{kg m}^{-2} \text{s}^{-1}$
<i>Near IR albedo for direct radiation</i>	-
<i>Near IR albedo for diffuse radiation</i>	-
<i>Potential evaporation</i>	M
<i>Skin temperature</i>	K
<i>Snow albedo</i>	-
<i>Snow evaporation</i>	m of water equivalent
<i>Snowfall</i>	m of water equivalent
<i>Surface latent heat flux</i>	$\text{J m}^{-2}$
<i>Surface net solar radiation</i>	$\text{J m}^{-2}$
<i>Surface net solar radiation, clear sky</i>	$\text{J m}^{-2}$
<i>Surface net thermal radiation</i>	$\text{J m}^{-2}$
<i>Surface net thermal radiation, clear sky</i>	$\text{J m}^{-2}$
<i>Surface pressure</i>	Pa
<i>Surface sensible heat flux</i>	$\text{J m}^{-2}$
<i>Surface solar radiation downward clear-sky</i>	$\text{J m}^{-2}$
<i>Surface solar radiation downwards</i>	$\text{J m}^{-2}$
<i>Surface thermal radiation downward clear-sky</i>	$\text{J m}^{-2}$
<i>Surface thermal radiation downwards</i>	$\text{J m}^{-2}$
<i>Temperature of snow layer</i>	K
<i>TOA incident solar radiation</i>	$\text{J m}^{-2}$
<i>Top net solar radiation</i>	$\text{J m}^{-2}$
<i>Top net solar radiation, clear sky</i>	$\text{J m}^{-2}$
<i>Top net thermal radiation</i>	$\text{J m}^{-2}$
<i>Top net thermal radiation, clear sky</i>	$\text{J m}^{-2}$
<i>Total column rainwater</i>	$\text{kg m}^{-2} \text{s}^{-1}$
<i>Total column snow water</i>	$\text{kg m}^{-2} \text{s}^{-1}$
<i>Total precipitation</i>	M
<i>Total sky direct solar radiation at surface</i>	$\text{J m}^{-2}$
<i>UV visible albedo for diffuse radiation</i>	-
<i>UV visible albedo for direct radiation</i>	-

## Appendix B - Breakout events

**Appendix Table B.1. Observed breakout events included in the binary breakout event variable and ancillary observations of the event size and location along the northern floe edge.**

Date	Location	Long Axis (km)	Short Axis (km)	Elliptical Area (km <sup>2</sup> )
2000-06-11	East	28.5	12.6	282.0
2000-06-23	East	23	4.1	74.1
2000-07-05	Plug	32	22.6	568.0
2000-07-15	Breakup			
2001-07-03	Centre	57.5	25.41	1147.5
2001-07-18	Breakup			
2002-07-10	Plug	38	25.5	761.1
2002-07-26	Breakup			
2003-06-26	East	20.1	3.9	61.6
2003-07-09	Plug	34.3	19.5	525.3
2003-07-17	Breakup			
2004-06-19	East	18.7	12.2	179.2
2004-06-20	East	18.1	11	156.4
2004-07-06	Plug	31.3	27.9	685.9
2004-07-12	Plug	25.8	3.6	72.9
2004-07-15	Plug	23.6	19	352.2
2004-07-19	Breakup			
2005-06-18	East	51.6	12.7	514.7
2005-06-27	West	19.7	8.1	125.3
2005-06-30	East	24.3	14.8	282.5
2005-07-10	Plug	38.8	25	761.8
2005-07-14	Centre	29.1	12.5	285.7
2005-07-21	Breakup			
2006-06-19	Plug	61.3	23.4	1126.6
2006-07-05	Plug	27.8	27.4	598.3
2006-07-09	West	10.5	1.6	13.2
2006-07-19	Breakup			
2007-05-29	West	5.9	1.5	7.0
2007-05-30	West	11	4.5	38.9
2007-06-14	East	46.3	13	472.7
2007-06-15	Centre	14.4	5.5	62.2
2007-06-22	Centre	10.7	4.5	37.8
2007-06-29	West	7.9	4.7	29.2
2007-07-13	Breakup			
2008-05-16	East	27.7	8.7	189.3
2008-06-06	East	5.3	2.1	8.7
2008-06-14	East	8.8	6.1	42.2
2008-06-17	East	7.1	6.1	34.0
2008-07-11	Centre	7	4.5	24.7

Date	Location	Long Axis (km)	Short Axis (km)	Elliptical Area (km <sup>2</sup> )
2008-07-15	Breakup			
2009-06-17	East	33.8	15.7	416.8
2009-07-01	Plug	41.5	15.9	518.2
2009-07-03	East	8.2	4.7	30.3
2009-07-04	Plug	38.4	24.1	726.8
2009-07-05				
2009-07-09	Plug	28.8	25.5	576.8
2009-07-16	Breakup			
2010-05-05	East	9.3	6.1	44.6
2010-05-07	East	17.8	8.7	121.6
2010-07-11	West	9	5.6	39.6
2010-07-17	Breakup			
2011-05-29	West	18.5	11.7	170.0
2011-06-07	Centre	5.6	1.8	7.9
2011-06-10	East	42.4	10	333.0
2011-06-15	East	39.7	6.8	212.0
2011-07-11	Breakup			
2012-07-08	Breakup			
2013-05-02	Centre	66.3	6.7	348.9
2013-06-15	East	37.9	5.3	157.8
2013-06-16	Centre	14.4	2.2	24.9
2013-06-18	East	30	6.8	160.2
2013-06-24	Plug	40.3	23.3	737.5
2013-06-25	Plug	29.1	7.8	178.3
2013-07-08	West	13.5	13.5	143.1
2013-07-13	Breakup			
2014-04-23	Centre	29.8	7.7	180.2
2014-04-26	East	36.1	4	113.4
2014-06-24	West	17.7	2.2	30.6
2014-06-29	Plug	31	18.1	440.7
2014-07-07	East	6.2	3.9	19.0
2014-07-09	Plug	24.9	24	469.4
2014-07-16	Breakup			
2015-06-20	Centre	14.6	5.8	66.5
2015-06-21	East	53.5	16.3	684.9
2015-06-22	East	30.2	4.1	97.2
2015-07-05	East	11.2	26	228.7
2015-07-09	East	7.9	2.9	18.0
2015-07-18	East	8.2	5	32.2
2015-07-19	Breakup			
2016-04-12	Centre	39.1	14.7	451.4
2016-04-13	East	26.8	10.7	225.2
2016-04-15	East	19.9	7.5	117.2
2016-04-16	East	16.1	7.5	94.8

Date	Location	Long Axis (km)	Short Axis (km)	Elliptical Area (km <sup>2</sup> )
2016-04-19	Centre	38.6	15.2	460.8
2016-04-23	Plug	54.9	16.7	720.1
2016-04-26	West	10.8	2.6	22.1
2016-06-17	Centre	10.7	2.9	24.4
2016-06-20	Centre	34.9	2.3	63.0
2016-06-22	East	11.4	4.7	42.1
2016-07-01	Plug	30.1	16.6	392.4
2016-07-03	East	13.2	2.5	25.9
2016-07-04	West	21.9	7.1	122.1
2016-07-05	Plug	23.6	11.8	218.7
2016-07-07	Plug	25	5.6	110.0
2016-07-09	Breakup			
2017-04-17	Centre	50.6	18.7	743.2
2017-04-19	East	6.7	2.9	15.3
2017-05-10	West	37.2	5.8	169.5
2017-05-31	East	25.6	9.4	189.0
2017-06-02	East	12.9	2.8	28.4
2017-06-03	Centre	10.8	8.5	72.1
2017-06-27	Plug	30.6	26.5	636.9
2017-06-28	Plug	25.2	7.1	140.5
2017-07-09	West	10.7	7	58.8
2017-07-13	Breakup			
2018-06-17	Centre	31.7	13.7	341.1
2018-06-22	West	18.2	4.2	60.0
2018-07-08	Plug	60.8	25	1193.8
2018-07-10	Plug	32.1	11.9	300.0
2018-07-15	West	15.4	3	36.3
2018-07-17	Plug	27.9	18.4	403.2
2018-07-20	Breakup			
2019-06-28	Plug	60.9	30.6	1463.6
2019-07-04	East	6.3	3.6	17.8
2019-07-08	Breakup			
2020-04-28	Centre	51.1	15.9	638.1
2020-05-30	East	29.4	6	138.5
2020-06-07	East	23.3	13.6	248.9
2020-06-09	West	22.2	5.2	90.7
2020-06-21	Plug	29.9	18.2	427.4
2020-06-26	Plug	24.9	4.4	86.0
2020-07-02	Plug	25.4	14.6	291.3
2020-07-06	Breakup			

## Appendix C - Significant environmental variables

Appendix Table C.1 Environmental variables and corresponding derivatives with significant point-biserial correlations at an  $\alpha = 0.10$ . Positive correlations are black and negative correlations are red. 0 is the variable on the day-of the event and leads (L) and averages (A) are 1 through 21.

Environmental Variables		L																								
		0	A	1	2	3	4	5	6	7	8	9	0	1	1	1	1	1	1	1	1	1	1	2	2	
Mechanical	100 metre V wind component	L	█																							
	A																									
	100 metre U wind component	L			█				█																	
	A																									
	Neutral wind at 10 m V-component	L	█																							
	A																									
	Neutral wind at 10 m U-component	L			█				█																	
	A																									
	10 metre V wind component	L	█																							
	A																									
	10 metre U wind component	L			█				█																	
	A																									
	Mean eastward gravity wave surface stress	L			█				█																	
	A																									
Mean eastward turbulent surface stress	L			█				█																		
A																										
Mean sea level pressure	L			█	█							█	█	█	█	█	█	█	█	█	█	█	█	█	█	
A				█	█	█					█	█	█	█	█	█	█	█	█	█	█	█	█	█	█	
Surface pressure	L			█	█							█	█	█	█	█	█	█	█	█	█	█	█	█	█	
A				█	█	█					█	█	█	█	█	█	█	█	█	█	█	█	█	█	█	
Non-radiative fluxes	Forecast logarithm of surface roughness for heat	L	█	█	█	█	█	█																		
	A		█	█	█	█	█	█	█																	
	Instantaneous surface sensible heat flux	L						█															█			
	A																									
	Mean potential evaporation rate	L																					█	█	█	█
	A																						█	█	█	█

Environmental Variables		L / A																					
		0	1	2	3	4	5	6	7	8	9	0	1	1	1	1	1	1	1	1	2	2	
Radiation Balance	Mean snow evaporation rate	█																					
	A																						
	Mean vertically integrated moisture divergence				█										█								
	A				█	█	█	█	█	█	█	█	█	█	█	█	█	█	█	█	█	█	█
	Potential evaporation																						
	A																						
	Snow evaporation	█																					
	A																						
	Mean surface direct short-wave radiation flux				█	█	█																█
	A				█	█	█	█															█
	Mean surface downward long-wave radiation flux				█	█	█																
	A				█	█	█																
	Mean surface downward short-wave radiation flux				█	█	█																█
	A				█	█	█																█
	Mean surface net long-wave radiation flux	█			█	█	█	█	█														█
	A				█	█	█	█	█														█
	Mean surface net long-wave radiation flux, clear sky				█																		
	A				█																		
	Mean surface net short-wave radiation flux																						█
	A																						█
Mean top net long-wave radiation flux																						█	
A																						█	
Mean top net short-wave radiation flux																						█	
A																						█	
Snow Albedo	█																						
A																							
Surface net solar radiation																						█	
A																						█	
Surface net thermal radiation	█			█	█	█																█	
A				█	█	█																█	
Surface net thermal radiation, clear sky				█																			
A				█																			



Environmental Variables			L																				
	0	A	1	2	3	4	5	6	7	8	9	0	1	1	1	1	1	1	1	1	2	2	
Mean convective precipitation rate	L																						
	A																						
Mean convective snowfall rate	L																						
	A																						
Mean large-scale precipitation fraction	L																						
	A																						
Mean large-scale precipitation rate	L																						
	A																						
Mean large scale snowfall rate	L																						
	A																						
Mean snowfall rate	L																						
	A																						
Mean total precipitation rate	L																						
	A																						
Minimum total precipitation rate since previous post-processing	L																						
	A																						
Snowfall	L																						
	A																						
Total column rainwater	L																						
	A																						
Total column snow water	L																						
	A																						
Total precipitation	L																						
	A																						

## Appendix D - Auxiliary logistic regression models

**Appendix Table D.1** Logistic regression parameters for the five predictors in the first auxiliary model. Coeff = regression coefficient ( $\beta$ ), Std. Err. = standard error on the regression coefficient,  $z$  =  $z$ -value on the regression coefficient, 95% CI = 95% confidence interval, Z Coeff. = regression coefficient of the  $z$ -value transformed data set, Z Std. Err. = standard error on the regression coefficient of the  $z$ -value transformed data set,  $p[\chi^2]$  =  $p$ -value of the  $\chi^2$  statistic.

Variable	Coeff.	Std. Err.	$z$	95% CI		Z Coeff.	Z Std. Err.	$\chi^2$	P [ $\chi^2$ ]
Intercept ( $\beta_0$ )	$-3.5 \times 10^1$	$1.5 \times 10^1$	-2.3	$-1.3 \times 10^1$	$-2.9 \times 10^0$	-2.04	0.11	-	-
Instantaneous surface sensible heat flux (5-day lead)	$-3.1 \times 10^{-2}$	$1.5 \times 10^{-2}$	-2.0	$1.8 \times 10^{-1}$	$7.7 \times 10^{-1}$	-0.22	0.11	4.1	0.043
Total precipitation (3-day average)	$4.9 \times 10^{-1}$	$1.5 \times 10^{-1}$	3.3	$8.1 \times 10^{-3}$	$1.2 \times 10^{-1}$	0.44	0.13	11.0	0.001
10 metre U wind component (6-day lead)	$6.0 \times 10^{-2}$	$2.9 \times 10^{-2}$	2.1	$-1.9 \times 10^4$	$2.9 \times 10^5$	0.22	0.10	4.4	0.035
Snow evaporation (day-of)	$1.7 \times 10^0$	$9.5 \times 10^{-1}$	1.8	$-1.9 \times 10^4$	$2.9 \times 10^5$	0.91	0.51	3.3	0.071
Total precipitation (20-day lead)	$-1.3 \times 10^{-1}$	$3.2 \times 10^{-2}$	-3.9	$-1.8 \times 10^{-1}$	$-5.8 \times 10^{-2}$	-0.28	0.07	15.4	<0.001

**Appendix Table D.2 Logistic regression parameters for the four predictors in the second auxiliary model. Coeff = regression coefficient ( $\beta$ ), Std. Err. = standard error on the regression coefficient, z = z-value on the regression coefficient, 95% CI = 95% confidence interval, Z Coeff. = regression coefficient of the z-value transformed data set, Z Std. Err. = standard error on the regression coefficient of the z-value transformed data set, p [ $\chi^2$ ] = p-value of the  $\chi^2$  statistic.**

Variable	Coeff.	Std. Err.	z	95% CI		Z Coeff.	Z Std. Err.	$\chi^2$	P [ $\chi^2$ ]
Intercept ( $\beta_0$ )	$1.5 \times 10^0$	$1.3 \times 10^0$	1.1	$-1.7 \times 10^0$	$3.24 \times 10^0$	-1.97	0.10	-	-
Surface thermal radiation downwards (3-day average)	$-2.8 \times 10^{-6}$	$1.2 \times 10^{-6}$	-2.3	$-4.4 \times 10^{-6}$	$7.8 \times 10^{-8}$	-0.42	0.18	5.4	0.020
Instantaneous surface sensible heat flux (17-day lead)	$-3.3 \times 10^{-2}$	$1.6 \times 10^{-2}$	-2.1	$3.2 \times 10^{-6}$	$1.3 \times 10^{-5}$	-0.23	0.11	4.2	0.040
Surface net thermal radiation (3-day average)	$9.2 \times 10^{-6}$	$2.6 \times 10^{-6}$	3.5	$3.2 \times 10^{-6}$	$1.3 \times 10^{-5}$	0.52	0.15	12.4	0.001
Total sky direct solar radiation at surface (20-day lead)	$1.6 \times 10^{-6}$	$5.0 \times 10^{-7}$	3.2	$5.6 \times 10^{-7}$	$2.5 \times 10^{-6}$	0.37	0.12	9.9	0.002

**Appendix Table D.3 Logistic regression parameters for the seven predictors in the third auxiliary model. Coeff = regression coefficient ( $\beta$ ), Std. Err. = standard error on the regression coefficient,  $z$  = z-value on the regression coefficient, 95% CI = 95% confidence interval, Z Coeff. = regression coefficient of the z-value transformed data set, Z Std. Err. = standard error on the regression coefficient of the z-value transformed data set,  $p$  [ $\chi^2$ ] = p-value of the  $\chi^2$  statistic.**

Variable	Coeff.	Std. Err.	$z$	95% CI		Z Coeff.	Z Std. Err.	$\chi^2$	P [ $\chi^2$ ]
Intercept ( $\beta_0$ )	$3.2 \times 10^1$	$1.8 \times 10^1$	1.8	$-1.7 \times 10^0$	$-6.2 \times 10^{-1}$	-1.95	0.10	-	-
10 metre V wind component (1-day average)	$7.2 \times 10^{-2}$	$4.1 \times 10^{-2}$	1.7	$-1.6 \times 10^{-3}$	$1.6 \times 10^{-1}$	0.17	0.10	3.7	0.082
Convective rain rate (15-day lead)	$-3.4 \times 10^{-2}$	$1.9 \times 10^{-2}$	-1.8	$-1.6 \times 10^{-3}$	$1.6 \times 10^{-1}$	-0.20	0.11	3.7	0.070
Convective snowfall rate water equivalent (14-day lead)	$3.4 \times 10^{-2}$	$1.7 \times 10^{-2}$	2.0	$-1.6 \times 10^{-3}$	$1.6 \times 10^{-1}$	0.20	0.10	3.7	0.043
Large scale precipitation (19-day lead)	$-5.7 \times 10^{-2}$	$3.5 \times 10^{-2}$	-1.7	$-1.6 \times 10^{-3}$	$1.6 \times 10^{-1}$	-0.13	0.08	3.7	0.099
Snowfall (20-day lead)	$-4.3 \times 10^{-2}$	$2.1 \times 10^{-2}$	-2.0	$-1.6 \times 10^{-3}$	$1.6 \times 10^{-1}$	-0.19	0.09	3.7	0.041
Surface net thermal radiation, clear sky (3-day lead)	$6.0 \times 10^{-6}$	$3.4 \times 10^{-6}$	1.8	$-1.6 \times 10^{-3}$	$1.6 \times 10^{-1}$	0.18	0.10	3.7	0.076
Surface pressure (8-day average)	$-3.0 \times 10^{-4}$	$1.8 \times 10^{-2}$	-1.7	$-8.0 \times 10^{-2}$	$-1.3 \times 10^{-2}$	-0.19	0.11	7.4	0.086

**Appendix Table D.4 Logistic regression parameters for the two predictors in the fourth auxiliary model. Coeff = regression coefficient ( $\beta$ ), Std. Err. = standard error on the regression coefficient,  $z$  = z-value on the regression coefficient, 95% CI = 95% confidence interval, Z Coeff. = regression coefficient of the z-value transformed data set, Z Std. Err. = standard error on the regression coefficient of the z-value transformed data set,  $p[\chi^2]$  = p-value of the  $\chi^2$  statistic.**

Variable	Coeff.	Std. Err.	$z$	95% CI		Z Coeff.	Z Std. Err.	$\chi^2$	P [ $\chi^2$ ]
Intercept ( $\beta_0$ )	$2.0 \times 10^1$	$1.1 \times 10^1$	1.8	$2.5 \times 10^0$	$4.7 \times 10^1$	-1.91	0.10	-	-
Mean sea level pressure (13-day lead)	$-2.2 \times 10^{-4}$	$1.1 \times 10^{-4}$	-1.9	$-1.2 \times 10^{-1}$	$4.3 \times 10^{-3}$	-0.19	0.10	3.6	0.058
Surface net thermal radiation (day-of)	$2.5 \times 10^{-6}$	$1.4 \times 10^{-6}$	-1.9	$-4.7 \times 10^{-4}$	$-3.3 \times 10^{-5}$	0.18	0.10	3.4	0.064

**Appendix Table D.5 Logistic regression parameters for the one predictor in the fifth auxiliary model. Coeff = regression coefficient ( $\beta$ ), Std. Err. = standard error on the regression coefficient,  $z$  = z-value on the regression coefficient, 95% CI = 95% confidence interval, Z Coeff. = regression coefficient of the z-value transformed data set, Z Std. Err. = standard error on the regression coefficient of the z-value transformed data set,  $p[\chi^2]$  = p-value of the  $\chi^2$  statistic.**

Variable	Coeff.	Std. Err.	$z$	95% CI		Z Coeff.	Z Std. Err.	$\chi^2$	P [ $\chi^2$ ]
Intercept ( $\beta_0$ )	$-2.2 \times 10^0$	$1.8 \times 10^{-1}$	-11.8	$2.5 \times 10^0$	$4.7 \times 10^1$	-1.89	0.10	-	-
Mean surface direct short-wave radiation flux (21-day lead)	$2.8 \times 10^{-3}$	$1.4 \times 10^{-3}$	2.0	$-4.7 \times 10^{-4}$	$-3.3 \times 10^{-5}$	-0.19	0.10	3.9	0.047

**Appendix Table D.6 Logistic regression parameters for the one predictor in the sixth auxiliary model. Coeff = regression coefficient ( $\beta$ ), Std. Err. = standard error on the regression coefficient, z = z-value on the regression coefficient, 95% CI = 95% confidence interval, Z Coeff. = regression coefficient of the z-value transformed data set, Z Std. Err. = standard error on the regression coefficient of the z-value transformed data set, p [ $\chi^2$ ] = p-value of the  $\chi^2$  statistic.**

Variable	Coeff.	Std. Err.	z	95% CI		Z Coeff.	Z Std. Err.	$\chi^2$	P [ $\chi^2$ ]
Intercept ( $\beta_0$ )	$-1.1 \times 10^1$	$4.6 \times 10^0$	-2.3	$2.5 \times 10^0$	$4.7 \times 10^1$	-1.89	0.10	-	-
Snow albedo (day-of)	$1.1 \times 10^1$	$5.5 \times 10^0$	1.9	$-4.7 \times 10^{-4}$	$-3.3 \times 10^{-5}$	0.19	0.10	3.8	0.052